Spring 2015

Assessment of high-fidelity collision models in the direct simulation Monte Carlo method

Andrew Brian Weaver
Purdue University

Graduate School Form 30
Updated 1/15/2015

PURDUE UNIVERSITY
GRADUATE SCHOOL
Thesis/Dissertation Acceptance

This is to certify that the thesis/dissertation prepared

By Andrew B. Weaver

Entitled
Assessment of High-Fidelity Collision Models in the Direct Simulation Monte Carlo Method

For the degree of Doctor of Philosophy

Is approved by the final examining committee:

Alina Alexeenko
Chair

Gregory A. Blaisdell

Jong Hyun Choi

Robert P. Lucht

To the best of my knowledge and as understood by the student in the Thesis/Dissertation Agreement, Publication Delay, and Certification Disclaimer (Graduate School Form 32), this thesis/dissertation adheres to the provisions of Purdue University's "Policy of Integrity in Research" and the use of copyright material.

Approved by Major Professor(s): Alina Alexeenko

Approved by: Weinong Chen 3/3/2015
Head of the Departmental Graduate Program Date

ASSESSMENT OF HIGH-FIDELITY COLLISION MODELS IN THE DIRECT SIMULATION MONTE CARLO METHOD

A Dissertation

Submitted to the Faculty

of

Purdue University

by

Andrew B. Weaver

In Partial Fulfillment of the

Requirements for the Degree

of

Doctor of Philosophy

May 2015

Purdue University

West Lafayette, Indiana

I dedicate this to my wife, Debbie, for her patience with me through the years.

ACKNOWLEDGMENTS

There are many people whom I would like to thank for their support during the course of my graduate academic career. First and foremost, I sincerely thank my advisor Professor Alina Alexeenko for all the support and for the many skills obtained through her guidance. The useful advice and recommendations from Professors Gregory Blaisdell, Jong Hyun Choi, and Robert Lucht have also helped guide my research; for which I am very thankful. I am truly grateful for the insight and discussions with Dr. Michael Gallis and Dr. John Torczynski in support of the research performed at Sandia National Laboratories.

My research group colleagues and friends deserve acknowledgments for their moral support and advice: Arnab, Bill, Cem, Devon, Gayathri, Israel, Marat, Nikhil, Siva, and Venkattraman. The support and encouragement of my family over the years is greatly appreciated. A special thanks goes to all the faculty and staff at Purdue University for creating this engaging educational environment, and especially Ms. Linda Flack.

TABLE OF CONTENTS

LIST OF TABLES

LIST OF FIGURES

Figure Page

Figure Page

Figure Page

SYMBOLS

c_r	relative collisional velocity
h	Planck's constant ($6.62606957 \times 10^{-34}\, J \cdot s$)
k	Boltzmann constant ($1.380648 \times 10^{-23}\, J/K$)
m	mass
m_r	collision-reduced mass
n	number density
T_t	translational temperature
T_r	rotational temperature
T_v	vibrational temperature
T^*	non-dimensional temperature (kT/ϵ)
v	velocity
χ	scattering angle
ϵ	potential well depth
$\Omega^{*(l,s)}$	reduced collision integral
ϕ	intermolecular potential energy

ABBREVIATIONS

CFD	Computational Fluid Dynamics
DSMC	Direct Simulation Monte Carlo
FHO	Forced Harmonic Oscillator
L-B	Larsen-Borgnakke
L-J	Lennard-Jones
PIC	Particle-in-Cell
QCT	Quasi-Classical Trajectory
VHS	Variable Hard Sphere
VSS	Variable Soft Sphere

ABSTRACT

Weaver, Andrew B. PhD, Purdue University, May 2015. Assessment of High-Fidelity Collision Models in the Direct Simulation Monte Carlo Method . Major Professor: Alina Alexeenko.

Advances in computer technology over the decades has allowed for more complex physics to be modeled in the DSMC method. Beginning with the first paper on DSMC in 1963, 30,000 collision events per hour were simulated using a simple hard sphere model. Today, more than 10 billion collision events can be simulated per hour for the same problem. Many new and more physically realistic collision models such as the Lennard-Jones potential and the forced harmonic oscillator model have been introduced into DSMC. However, the fact that computer resources are more readily available and higher-fidelity models have been developed does not necessitate their usage. It is important to understand how such high-fidelity models affect the output quantities of interest in engineering applications. The effect of elastic and inelastic collision models on compressible Couette flow, ground-state atomic oxygen transport properties, and normal shock waves have therefore been investigated. Recommendations for variable soft sphere and Lennard-Jones model parameters are made based on a critical review of recent *ab-initio* calculations and experimental measurements of transport properties.

1. INTRODUCTION

The Direct Simulation Monte Carlo (DSMC) method [1] for rarefied gas flows is based on kinetic theory formulated centuries earlier. Gassendi has been claimed to be the father of kinetic theory [2] with his explanation of the three states of matter and the motion of gas particles. It was nearly 200 years after Gassendi that kinetic theory had gained substantial attention from such mathematicians and physicists as R. Clausius, J.C. Maxwell and L. Boltzmann [3], to name a few. The key idea from kinetic theory is the existence of microscopic particles known as atoms; which, by their chaotic motion through space, accounts for the macroscopic fluid properties such as density, pressure, and temperature.

As with the Navier-Stokes equations, very few analytic solutions exist for the governing equation of rarefied gas flows known as the Boltzmann equation. Solutions only exist for simple flows such as those in the free molecular regime where the mean molecular spacing between molecules is so great that they never collide with each other. Thus, Couette flow, thermophoresis, and transpiration phenomena are prime examples of the types of problems which may be studied analytically.

Direct solution of the Boltzmann equation is a valid approach to extend the application beyond free molecular flows, but is still limited to relatively simple problems. The number of grid points when considering the three-dimensions in physical space as well as an additional three in velocity space makes this approach computationally unfeasible. On the other hand, much like molecular dynamics (MD) is a solution method for dense gases, the DSMC method is a particle simulation approach which may be utilized to obtain a solution for dilute gases.

Many of the models most widely used in DSMC are phenomenological in nature and are justified in that the DSMC method itself is a probabilistic approach. These phenomenological models are calibrated to match experimental values, usu-

ally to equilibrium conditions as it applies to reaction rates and relaxation times. The Larsen-Borgnakke (L-B) model [4] is an example of a popular, inelastic collision model for which translational and internal energies are redistributed between colliding molecules. While the dissociation rates may compare well with experiments, the relaxation process may differ significantly from more physically derived models [5] such as the forced harmonic oscillator (FHO) model. [6,7] For elastic collisions in which there is no change in kinetic energy, the variable hard sphere (VHS) proposed by Bird [1,8] and the variable soft sphere (VSS) proposed by Koura and Matsumoto [9,10] are commonly found in DSMC literature. Like the L-B model, the VHS and VSS models are largely phenomenological, and a more physically realistic model would contain both short-range repulsive as well as long-range attractive contributions. One such model is the Lennard-Jones (L-J) model [11], and although its conception dates back to the mid 1920s, it has seen limited use in DSMC codes due to its relative complexity.

This work focuses on the aforementioned elastic and inelastic collision models and their effects on DSMC simulations of gas flows. In this chapter, motivations and applications for the study of high-fidelity collision models in DSMC will be discussed as well as the goals and objectives. The theory for binary collision dynamics, including details for computing transport properties from scattering angles, and and introduction to the DSMC method is presented in Chapter 2. DSMC simulations of Couette flows using VHS/VSS and L-J models are presented in Chapter 4 along with VSS and L-J model parameter recommendations for 8 common gases. Binary scattering angle and collision cross-section calculations for the ground state of atomic oxygen collisions are also presented in Chapter 4. Inelastic collision modeling is described in detail in Chapter 5, and a consistent Born-Mayer-FHO model is compared to both VSS-FHO and VSS-LB models for energy relaxation in a 0-D heat bath and 1-D normal shock wave. Concluding remarks and summaries are made in Chapter 6.

1.1 Motivation and Background Information

Thanks to the shrinking physical size of the transistors, more may be manufactured on a single CPU in an effort to improve clock speed. Recently, however, it has been easier to simply increase the number of processors rather than improve the performance of a single CPU core due to power and heat constraints as well as physical limit of transistor size. [12] Since 2005, multicore CPU's have become mainstream for scientific computing. The development has thus largely followed Moore's law of doubling the number of transistors every two years, as depicted in figure 1.1(a). Today, GPU's are being used to further accelerate the solution algorithm for computationally intensive problems, including computational fluid dynamics (CFD). [13, 14]

As computational power grows an increasing number of physics may be feasibly modeled. Dating back to 1963, the first paper on DSMC [15] as it is known today, pertained to the simulation of a 0-D relaxation problem. The simplest known interaction model, hard-sphere (HS), was used and 30,000 collision events were recorded per hour. In 1970 two million collision events per hour (nearly 66 times more than in 1963) were recorded on an IBM 360-75 computer at the California Institute of Technology [16]. The variable hard sphere (VHS) intermolecular model, L-B inelastic collision model, and the total collision energy (TCE) model for reactions are substantial achievements to the DSMC method, as they are still commonplace today. Since then, a myriad of intermolecular models and collision schemes have been implemented including the majorant frequency [17] (MFS) and no-time counter [18] (NTC) schemes. During the 1990's there was a large push for accurate vibrational transition modeling, and one such model is the FHO model implemented into DSMC by Koura and Matsumoto [19] in 1994. Figure 1.1(b) shows that along with the drastic increase in the number of simulated collisions per hour, the number of papers per year related to DSMC has also been on the rise.

The technological advancement has also pushed the physical chemistry community to explore *ab-initio* potentials via the solution of the Schrödinger wave equation. [20–

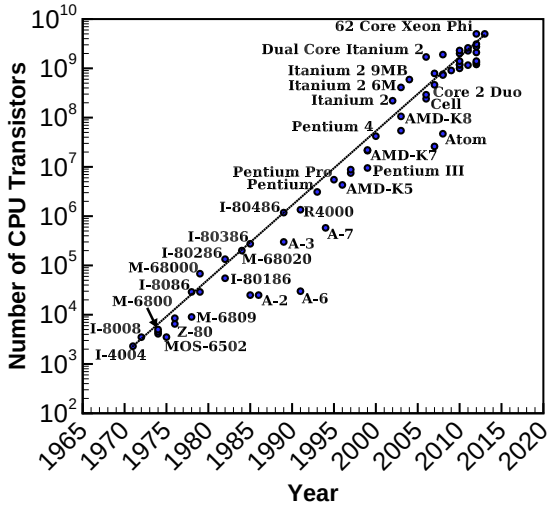

(a) Moore's Law for CPU's. Notation as follows: A=Acorn, I=Intel, M=Motorola, Z=Zilog, (┈)=Moore's Law

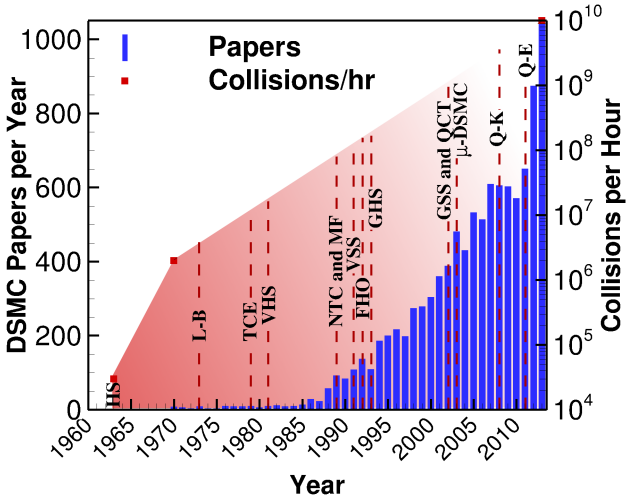

(b) Growth of DSMC users and capabilities

Figure 1.1.. Moore's Law and the development of DSMC

26] These intermolecular interactions are fundamental to the DSMC method and are therefore worthwhile to study within the DSMC framework itself. Under which conditions and for which applications do the more complex potentials differ from the

simpler, phenomenological models? What is the computational cost of utilizing more complex potentials in DSMC? These are the sort of questions driving the research presented in this dissertation.

1.2 Applications for High-Fidelity Collision Modeling in DSMC

There are a wide variety of applications which may benefit from high-fidelity collision modeling. Ranging from low-temperature gas flows such as supersonic expansion experiments [27] or sputter deposition to high-temperature gas flows encountered in hypersonic cruise and reentry, the use of more physically accurate collision models helps us to better understand and predict the observed phenomena.

First, consider the impact of the background gas collision model on sputter deposition. This is one method used in material processing to deposit a thin film on a substrate, and the development of the M1 elastic collision model was motivated by the need for an improved representation of the sputtering deposition rates. [28] In such conditions the attractive term in the intermolecular potential becomes significant, and its inclusion in the M1 model predicted a lower peak concentration of target atoms (Ti) than the standard VHS model.

Another example is the rate of NO formation due to hypersonic flight through air. At such high temperatures, the attractive part of the potential is insignificant, and a softer, exponential repulsive potential is a more accurate representation of the collision cross-section than the VHS and even L-J models [28]. The formation of NO typically occurs through the $N_2 + O \rightarrow NO + N$ exchange reaction and the rate is therefore strongly dependent on the number densities of molecular nitrogen and atomic oxygen. Since this reaction, as well as the formation of atomic oxygen through dissociation, is more probable at higher ro-vibrational levels, it is important to use a higher-fidelity model which can more accurately represent this excitation process.

1.3 Goals and Objectives of the Dissertation

The advancement in computer technology has allowed for more accurate modeling of pertinent physics, and it is useful at this point to ascertain the benefits and costs of such implementations. The major goal of this dissertation is to explore and assess the performances of select higher-fidelity collision models in DSMC relative to those commonly used today. These collision models may be categorized into two groups: elastic and inelastic. The objectives for elastic collision models are as follows:

Objective 1 Study the effects of intermolecular potentials on shear stress and viscosity in the transitional regime.

Objective 2 Compare VSS and L-J models for viscosity to experiments through DSMC simulations of Couette flow.

Objective 3 Compute scattering angles, total collision cross-sections, and transport collision integrals for ground state atomic oxygen using a variety of empirical and *ab-initio* potentials.

Likewise for inelastic collision models, the objectives are as follows:

Objective 1 Investigate optimal implementation of FHO model into DSMC.

Objective 2 Formulate a consistent elastic collision model to be used with the FHO model.

Objective 3 Compare L-B and FHO models for relaxation times and temperature evolutions in a 0-D heat bath simulation.

Objective 4 Compare density and temperature profiles across a normal shock wave using the newly formulated, consistent elastic collision model.

2. KINETIC THEORY FOR THE CALCULATION OF TRANSPORT PROPERTIES

The theory for binary collision dynamics is based on classical mechanics. Two particles with velocities c_1 and c_2 and separated by a distance, r, approach each other. As a result of the collision, the two particles are scattered by an angle, χ, with post-collision velocities c_1^* and c_2^*. It is typical to work in a fixed scattering center frame of reference as illustrated in figure 2.1. In this frame of reference, the magnitude of relative collision velocity defined as the velocity of particle 1 with respect to particle 2, $c_r = c_1 - c_2$, is unchanged as a result of the collision. Thus, $c_r^* = c_r$. An impact parameter, b, dictates the separation distance measured perpendicular to the relative collision velocity. There is a head-on collision when the impact parameter is zero, and no collision as the impact parameter approaches infinity. The angle at which the colliding particles scatter is dependent on the intermolecular potential in addition to the relative collision velocity and impact parameter.

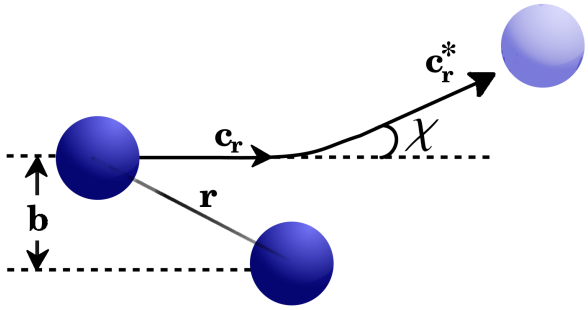

Figure 2.1.. Binary scattering diagram in the fixed scattering center frame of reference

The intermolecular potential specifies the forces attracting and repelling the colliding particles, and are typically categorized as either long-range or short-range forces, respectively. When particles are close enough such that their electron clouds are interacting, a strong repulsive force is exerted. Long-range forces, on the other hand, are a result of electrostatic, induction, and dispersion forces. Figure 2 illustrates the differences in the long-range forces.

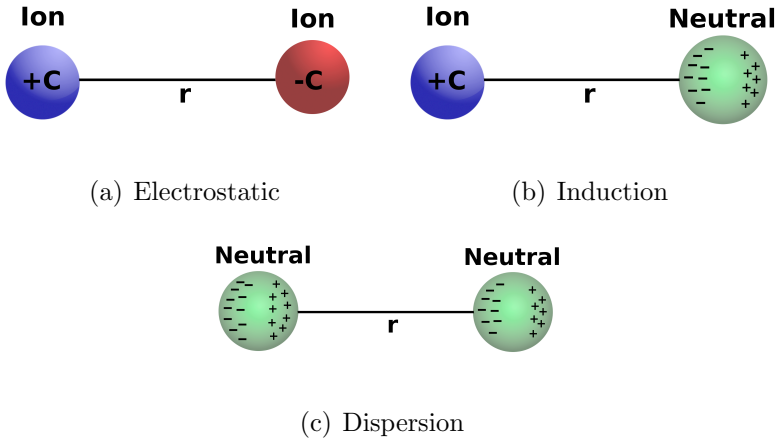

(a) Electrostatic (b) Induction

(c) Dispersion

Figure 2.2.. Schematics of long-range intermolecular forces

Electrostatic forces are caused by charged-particle charged-particle interactions. Thus, the interactions of ions and electrons are subject to this type of force. The most common model is the Coulomb potential,

$$\phi(r) = k_e \frac{(+C)(-C)}{r}\,, \tag{2.1}$$

which has a long-range force due to the two charges, $+C$ and $-C$. Coulomb's constant, k_e, is inversely proportional to the permittivity denoted by ϵ_0. The form of the Coulomb potential in Eq. (2.1) implies that like charges will repel while opposite charges will attract. Molecules with permanent dipole moments or quadrupole moments also experience electrostatic forces, but have a smaller range of influence. For a dipole-dipole interaction, the potential scales as r^{-3} and for quadrupole-quadrupole interactions the potential scales as r^{-5}.

Induction forces occur when a charged particle interacts with a neutral particle. The charge induces a polarity in the neutral particle; thereby creating an attractive force. The potential energy depends on the polarizability of the neutral particle, α, the charge of the charged particle, C, and the intermolecular separation distance, r, as

$$\phi(r) = -\frac{C^2\alpha}{2r^4}\,. \tag{2.2}$$

A molecule with a permanent dipole moment may also induce a polarity in the neutral particle; thereby causing an induction potential energy which scales as r^{-6}.

The last type of long-range force is the dispersion force (also called induced-dipole induced-dipole force) acting between two neutral particles. The latter term, induced-dipole induced-dipole force, is perhaps more descriptive of the nature of this force in that two non-polar molecules may instantaneously align opposite charges causing instantaneous dipole moments. Thus, even non-polar molecules may exert attractive forces at long-range distances depending on the characteristic energies and polarizabilities. The potential for dispersion has the form,

$$\phi(r) = -\frac{3}{2}\left(\frac{h\nu_1 h\nu_2}{h\nu_1 + h\nu_2}\right)\frac{\alpha_1\alpha_2}{r^6}\,. \tag{2.3}$$

Induced-dipole induced-quadrupole and induced-quadrupole induced-quadrupole interactions result in dispersion potential energies which scale as r^{-8} and r^{-10}, respectively.

Binary collisions may be adequately described using classical mechanics and assuming point centers of mass when two conditions are met. First, quantum effects become important when the molecular dimensions are on the order of the de Broglie wavelength [29],

$$L \sim \frac{h}{p}\,. \tag{2.4}$$

In Eq. (2.4) L is the molecular dimension (usually specified as the square root of momentum-transfer cross-section) and the ratio of Planck's constant to momentum is known as the de Broglie wavelength. If a hard sphere of diameter, d, is assumed

for the intermolecular potential and the most probable thermal speed at equilibrium is assumed for the momentum, p, then

$$L \sim \frac{h}{p} \quad \Rightarrow \quad \sqrt{\pi d^2} \sim \frac{h}{\sqrt{2kTm}}. \tag{2.5}$$

This condition will therefore be satisfied for most neutral gases as long as the mass and temperatures are large enough. Light gases such as hydrogen and helium are most likely to break this condition at low temperatures. The second condition is that the intermolecular potential is spherically symmetric. When the intermolecular potential is spherically symmetric, the orientation of the colliding particles is inconsequential and point centers of mass is a valid assumption.

Transport properties including self-diffusion coefficient, viscosity, and thermal conductivity may be computed from scattering angles assuming spherically symmetric potentials and only elastic collisions. Often times, non-spherical potentials such as the Stockmayer potential are averaged over all orientations such that they become spherically symmetric. For the formulations which follow, this assumption is necessary. As binary scattering angles are fundamental to all other properties discussed in this section, we will begin with the scattering angles.

The scattering angles may be computed for any spherically symmetric potential assuming negligible diffraction from quantum effects as

$$\chi\left(\epsilon, b\right) = \pi - 2b \int_{r_{min}}^{\infty} \frac{dr/r^2}{\sqrt{1 - \frac{b^2}{r^{*2}} - \frac{\phi(r)}{\epsilon}}}. \tag{2.6}$$

The lower limit of integration, r_{min}, is the distance of closest-approach depending on the impact parameter, b, relative collision energy, ϵ, and the intermolecular potential, $\phi(r)$. The distance of closest-approach may be determined from the root,

$$r_{min} = \text{root}\left[1 - \frac{\phi(r)}{\frac{1}{2}m_r c_r^2} - \frac{b^2}{r^2}\right], \tag{2.7}$$

where m_r is the collision-reduced mass, $m_r = m_1 m_2/(m_1 + m_2)$ and c_r is the relative collision velocity.

Transport cross-sections are integrals over the impact parameter as defined as [30]

$$S^{(l)}(\epsilon) = 2\pi \int_0^\infty \left(1 - \cos^l \chi\right)\, b\, \mathrm{d}b, \tag{2.8}$$

or

$$S^{*(l)}(\epsilon^*) = \frac{2}{\left(1 - \frac{1+(-1)^l}{2(1+l)}\right)} \int_0^\infty \left(1 - \cos^l \chi\right)\, b^*\, \mathrm{d}b^* \tag{2.9}$$

in non-dimensional terms; where the reduced collision energy is nondimensionalized by the potential well depth, $\epsilon^* = \frac{1}{2} m_r c_r^2/\epsilon$, and the reduced impact parameter is nondimensionalized by the intermolecular separation distance of zero potential energy, $b^* = b/\sigma$.

Collision integrals involve integration over collision energies and are defined as [30]

$$\Omega^{(l,s)}(T) = \sqrt{\frac{kT}{8\pi m_r}} \int_0^\infty \epsilon^{*s+1} S^{(l)}(\epsilon)\, \mathrm{e}^{-\epsilon^*}\, \mathrm{d}\epsilon^*, \tag{2.10}$$

or

$$\Omega^{*(l,s)}(T^*) = \frac{1}{(s+1)! T^{*s+2}} \int_0^\infty \epsilon^{*s+1} S^{*(l)}(\epsilon^*)\, \mathrm{e}^{-\epsilon^*/T^*}\, \mathrm{d}\epsilon^*, \tag{2.11}$$

in non-dimensional terms. In the previous non-dimensional equation, the non-dimensional temperature is expressed as $T^* = kT/\epsilon$. Both nondimensional transport cross-sections, $S^{*(l)}$, and collision integrals, $\Omega^{*(l,s)}$, are nondimensionalized by the corresponding values for a hard sphere (HS),

$$S_{HS}^{(l)} = \left(1 - \frac{1 + (-1)^l}{2\,(1+l)}\right) \pi\sigma^2, \quad \Omega_{HS}^{(l,s)} = \sqrt{\frac{kT}{2\pi m_r}} \frac{(s+1)!}{2} S_{HS}^{(l)}\,. \tag{2.12}$$

Finally, the transport properties may be written directly as a function of the collision integrals. Chapman-Enskog theory [3] may be applied near equilibrium to determine a first-order approximation to self-diffusion coefficient in a monatomic gas as

$$D_{11}^{(1)} = \frac{3}{8} \left(\frac{\sqrt{\pi m kT}}{\rho \pi \sigma^2 \Omega^{*(1,1)}}\right). \tag{2.13}$$

In the previous expression for self-diffusion coefficient, m is the mass of a single molecule, T is the temperature, and ρ is the density of the gas. For a pure gas, Kihara [30] obtained the higher-order approximation to self-diffusion coefficient,

$$D_{11}^{(Kihara)} = D_{11}^{(1)} \left[1 + \frac{\left(6C^* - 5\right)^2}{16A^* + 40}\right], \tag{2.14}$$

where

$$A^* = \frac{\Omega^{*(2,2)}}{\Omega^{*(1,1)}}$$
$$B^* = \frac{5\Omega^{*(1,2)} - 4\Omega^{*(1,3)}}{\Omega^{*(1,1)}}$$
$$C^* = \frac{\Omega^{*(1,2)}}{\Omega^{*(1,1)}} \tag{2.15}$$

Similarly, the viscosity may be computed using Chapman-Enskog theory [3] to a first-order approximation in a pure gas as

$$\mu^{(1)} = \frac{5}{16}\left(\frac{\sqrt{\pi mkT}}{\pi\sigma^2\Omega^{*(2,2)}}\right). \tag{2.16}$$

Kihara's higher-order approximation for viscosity [30] is a function of one diagonal and one off-diagonal collision integral, $\Omega^{*(2,2)}$ and $\Omega^{*(2,3)}$.

$$\mu^{(Kihara)} = \mu^{(1)}\left[1 + \frac{3}{49}\left(\frac{4\Omega^{*(2,3)}}{\Omega^{*(2,2)}} - \frac{7}{2}\right)^2\right] \tag{2.17}$$

A more rigorous formulation is provided in Chapman and Cowling [3] which results in nearly the same higher-order correction as Kihara [30]. Figure 2.3 shows the difference in the higher-order correction for viscosity between Chapman and Cowling's and Kihara's formulation assuming a L-J potential. The maximum difference in this range is 0.035% near a reduced temperature of 40. For reference, this would correspond to a temperature of nearly 5,000 K for argon gas.

Lastly, the thermal conductivity of a pure gas may be computed to a first-order approximation as

$$k^{(1)} = \frac{25}{32}\left(\frac{\sqrt{\pi mkT}}{\pi\sigma^2\Omega^{*(2,2)}}\right)\left(\frac{C_v}{m}\right) = \frac{15}{4}\frac{k}{m}\mu^{(1)}. \tag{2.18}$$

Notice both viscosity and thermal conductivity are linearly related and depend only on the viscosity-type collision integral, $\Omega^{*(2,2)}$, to a first-order approximation. A higher-order approximation to the thermal conductivity may also be computed as obtained by Kihara,

$$k^{(Kihara)} = k^{(1)}\left[1 + \frac{2}{21}\left(\frac{4\Omega^{*(2,3)}}{\Omega^{*(2,2)}} - \frac{7}{2}\right)^2\right]. \tag{2.19}$$

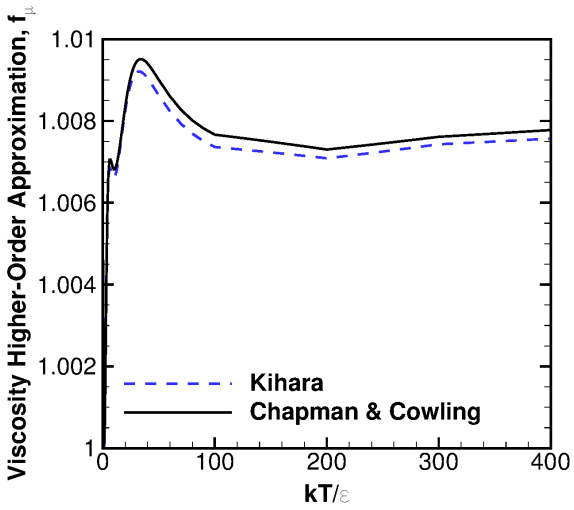

Figure 2.3.. Higher-order approximations to viscosity of a pure gas

For diatomic and polyatomic gases, internal energy modes contribute to the thermal conductivity and Eucken's formula [31] should be used instead. Eucken's formula,

$$k^{(1)}_{Eucken} = \frac{1}{4}\left(9\gamma - 5\right)\left(\frac{C_v}{M}\right)\mu^{(1)}\,, \tag{2.20}$$

accounts for the energy transfer from the translational to internal energy modes through the specific heat at constant volume, C_v. The definition of specific heat is the change in energy per change in temperature,

$$\frac{C_{v,tot}}{R} = \frac{\partial}{\partial T}\left(e_{tot}\right)\,, \tag{2.21}$$

where the total energy, $e_{tot} = e_t + e_r + e_v$, is the sum of the energies in each mode. Thus, we may write the total specific heat, $C_{v,tot}/R$, as a sum of the individual specific heats, $C_{v,t}, C_{v,r}$, and $C_{v,v}$.

Beginning with the translational mode, the average translational energy is $E_t = \frac{3}{2}kT$. Therefore, the specific heat per unit mass is $C_{v,t} = \frac{3}{2}R$. Substitution of this value into Eucken's formula in Eq. (2.20) would provide the monatomic gas result shown in Eq. (2.18).

The energy of the rotational modes may be expressed in terms of the partition function, [31]

$$E_r = kT^2 \frac{\partial}{\partial T} \left(\ln \left[Z_r \right] \right) . \tag{2.22}$$

The rotational partition function, Z_r, is the same for both diatomic and linear polyatomic molecules, and is expressed as

$$Z_r = \frac{1}{\sigma} \frac{T}{\theta_r} , \tag{2.23}$$

where σ is the symmetry factor (2 for symmetric molecule and 1 otherwise) and θ_r is the characteristic rotational temperature. The specific heat is then equal to R for both diatomic and linear polyatomic molecules.

The rotational partition function for non-linear polyatomic molecules is more complicated - involving the three principal axes of rotation about the center of mass, I_{aa}, I_{bb}, and I_{cc}. The partition function for non-linear polyatomic molecules may be expressed as

$$Z_r = \frac{1}{\sigma} \sqrt{\frac{\pi T^3}{\theta_A \theta_B \theta_C}} , \tag{2.24}$$

where the symmetry factor, σ, accounts for the number of ways the molecule can be rotated to result in the same orientation, and θ_A, θ_B, and θ_C are defined as follows.

$$\theta_A = \frac{h^2}{8\pi^2 k I_{aa}}, \quad \theta_B = \frac{h^2}{8\pi^2 k I_{bb}}, \quad \theta_C = \frac{h^2}{8\pi^2 k I_{cc}} . \tag{2.25}$$

Thus, as it turns out, the rotational specific heat is simply equal to $\frac{3}{2}R$ for non-linear polyatomic molecules.

Contributions from the vibrational mode may be expressed as a sum over all the vibrational modes,

$$C_{v,v} = R \sum_{i=1}^{m} \frac{\exp\left(\frac{\theta_{v,i}}{T}\right) \left(\theta_{v,i}/T\right)^2}{\left[\exp\left(\frac{\theta_{v,i}}{T}\right)\right]^2} , \tag{2.26}$$

where m is equal to 3N-5 for linear molecules and 3N-6 for non-linear molecules and $\theta_{v,i}$ is the characteristic vibrational temperature of the $i-th$ vibrational mode. More accurate formulations to correct for anharmonicity are detailed in the JANAF tables

by Chase *et al.* [32] The C_v data used in this work for diatomic and polyatomic species comes from the fit of C_p by Chase [33]; where $C_v/M = C_p/M - R$. More information on internal energy contributions to specific heat may also be found in Ref. [31]

In the sections that follow, a few of the common intermolecular potentials will be introduced. Depending on the potential used, simpler forms of the scattering angle and transport collision integral may be obtained. Any such simplification will be provided in the corresponding section for that particular potential. The forms of the potentials may be observed from figures 2.4(a) through 2.4(f). Note that the inverse power model illustrated in figure 2.4(c) may be either purely repulsive or purely attractive; hence the two curves.

2.1 Hard Sphere (HS) Model

By far the simplest model for an intermolecular interaction is the hard sphere (HS) model. This potential is shown in figure 2.4(a) where the potential energy is zero everywhere except when the separation distance is less than or equal to the collision diameter, d.

$$\phi(r) = \begin{cases} \infty & \text{for } r \leq d \\ 0 & \text{for } r > d \end{cases} \tag{2.27}$$

Thus, the HS model is analogous to billiard balls colliding. With the transport properties expressed in terms of the transport collision integrals nondimensionalized by the HS values, the transport properties for the HS model are as follows.

$$D_{11}^{(1)} = \frac{3}{8}\left(\frac{\sqrt{\pi mkT}}{\rho\pi d^2}\right) \tag{2.28}$$

$$\mu^{(1)} = \frac{5}{16}\left(\frac{\sqrt{\pi mkT}}{\pi d^2}\right) \tag{2.29}$$

$$k^{(1)} = \frac{25}{32}\left(\frac{\sqrt{\pi mkT}}{\pi d^2}\right)\left(\frac{C_v}{m}\right) = \frac{15}{4}\frac{k}{m}\mu^{(1)} \tag{2.30}$$

Scattering angles are independent of the relative collision energy and depend only on the impact parameter.

$$\chi(b) = 2\,\cos^{-1}\left(\frac{b}{d}\right) \tag{2.31}$$

2.2 Variable Hard/Soft Sphere (VHS)/(VSS) Models

In the study of gas flows, accurate predictions of the macroscopic properties are important, rather than microscopic properties such as accurate intermolecular forces. Thus, phenomenological models such as the variable hard sphere [1] (VHS) and variable soft sphere [9, 10] (VSS) have a strong basis for use in the computation of gas flows.

Both the VHS and VSS models have the same infinite repulsion as the HS model but the collision diameter is varied with collision energy in order to better match viscosity measurements. With the reference diameter, d_{ref}, specified at a reference temperature, T_{ref}, the diameter varies with relative collision velocity as [1]

$$d_{VSS} = d_{ref}\sqrt{\frac{(2kT_{ref}/m_r c_r^2)^{\omega-1/2}}{\Gamma(5/2-\omega)}}\,. \tag{2.32}$$

The viscosity index, ω, may vary between 0.5 and 1 depending on the interaction pair. A value of 0.5 for the viscosity index corresponds to the HS model, while a value of 1 corresponds to the Maxwell molecule. In the expression for VSS collision diameter, Γ denotes the Gamma function and m_r is the collision-reduced mass, $m_r = m_1 m_2/(m_1 + m_2)$.

$$\phi(r) = \begin{cases} \infty & \text{for } r \le d_{VSS} \\ 0 & \text{for } r > d_{VSS} \end{cases} \tag{2.33}$$

With the total collision cross-section being inversely proportional to $c_r^{2\omega-1}$, the viscosity for both the VHS and VSS models is proportional to a power of temperature,

$$\mu = \mu_{ref}\left(\frac{T}{T_{ref}}\right)^{\omega}\,. \tag{2.34}$$

The reference viscosity is may be used to define the reference diameter [1],

$$d_{\text{ref}} = \left[\frac{5(\alpha+1)(\alpha+2)(mkT_{\text{ref}}/\pi)^{1/2}}{4\alpha(5-2\omega)(7-2\omega)\mu_{\text{ref}}}\right]^{1/2} . \tag{2.35}$$

The scattering for the VHS model results in diffusion coefficients which are in poor agreement with measurements. [1, 9, 10] This lead to the development of the VSS model, which includes an additional model parameter, α, governing the scattering. When α is unity, the scattering,

$$\chi\left(b,\epsilon\right) = 2\cos^{-1}\left(\left[\frac{b}{d_{VSS}}\right]^{1/\alpha}\right) \tag{2.36}$$

becomes that of the VHS model.

The self-diffusion coefficient for the VSS model may be determined analytically, based on Chapman-Enskog theory, [1] and is provided in Eq. 2.37.

$$D_{11} = \frac{3\left(\alpha+1\right)\sqrt{\pi}\left(2kT/m_r\right)^{\omega}}{16\Gamma\left(7/2-\omega\right)n\sigma_{T,\text{ref}}\, c_{r,\text{ref}}^{2(\omega-1/2)}} \tag{2.37}$$

The Schmidt number is a ratio of momentum to mass diffusivity,

$$Sc = \frac{\mu_{\text{ref}}}{\rho\left(D_{11,\text{ref}}\right)} , \tag{2.38}$$

and is useful for relating viscosity and mass diffusion coefficient measurements to the VSS model parameters, ω and α. For the VSS model, Eq. (2.38) simplifies to [1]

$$Sc = \frac{2+\alpha}{(3/5)\left(7-2\omega\right)\alpha} . \tag{2.39}$$

2.3 Inverse Power Model

The inverse power model is either purely repulsive or purely attractive, with the potential energy scaling with a power of the separation distance, $\sim r^{-n}$. This potential is most appropriate to describe the interaction of unbound molecules. Following the work of Hirschfelder, Curtiss, and Bird [30], the potential may be written as

$$\phi(r) = \frac{d}{r^{\delta}} . \tag{2.40}$$

The scattering angle in Eq. (2.6) may be rewritten in terms of the quantities,

$$y = \frac{b}{r}, \quad y_{min} = \frac{b}{r_{min}}, \quad y_0 = b\left(\frac{\frac{1}{2}mc_r^2}{\delta d}\right)^{1/\delta} \tag{2.41}$$

where b is the impact parameter and y_{min} is the distance of closest approach for the given impact parameter and collision energy. This distance of closest approach must be determined numerically from Eq. (2.7) with the inverse power model of Eq. (2.40). The scattering angle then has the form

$$\chi(y_0) = \pi - 2\int_0^{y_{min}(y_0)} \left[1 - y^2 - \frac{1}{\delta}\left(\frac{y}{y_0}\right)^{\delta}\right]^{-1/2} \mathrm{d}y\,. \tag{2.42}$$

A tabulation of $y_{min}(y_0)$ and $\chi(y_0)$ is given in Table III of Hirschfelder, Curtiss, and Bird [30].

The transport cross-sections and collision integrals may be written in terms of the quantities in Eq. (2.41) and $A^{(l)}(\delta)$ defined as the integral,

$$A^{(l)}(\delta) = \int_0^{\infty} \left(1 - \cos^l \chi\right)\, y_0\, \mathrm{d}y_0\,. \tag{2.43}$$

The transport cross-sections and collision integrals are then given by Eqs. (2.44) and (2.45), respectively.

$$Q^{(l)} = \left(\frac{\delta d}{\frac{1}{2}m_r c_r^2}\right)^{2/\delta} A^{(l)}(\delta) \tag{2.44}$$

$$\Omega^{(l,s)} = \frac{1}{2}\sqrt{\frac{2\pi kT}{m_r}}\left(\frac{\delta d}{\frac{1}{2}m_r c_r^2}\right)^{2/\delta} A^{(l)}(\delta)\,\Gamma\left(s + 2 - \frac{2}{\delta}\right) \tag{2.45}$$

Numerical values of $A^{(l)}(\delta)$ are also tabulated in in table 8.3-3 of Hirschfelder, Curtiss, and Bird. [30]

2.4 Generalized Hard Sphere (GHS) Model

The GHS model also uses a scattering law similar to the VHS, but the total cross-section is instead varied with relative collision energy through the sum of two terms each depending on relative collision energy. The GHS total cross-section, [34]

$$(\sigma_T)_{GHS} = \pi d_{GHS}^2 = \sigma_{LJ}^2\left[\alpha_1\left(\frac{\epsilon}{\epsilon_{LJ}}\right)^{-\omega_1} + \alpha_2\left(\frac{\epsilon}{\epsilon_{LJ}}\right)^{-\omega_2}\right], \tag{2.46}$$

has a set of four constants: α_1, α_2, ω_1, and ω_2 which are determined by fitting to experimental or theoretical viscosity and diffusion coefficients. Apart from the four fitting parameters, the two parameters from the Lennard-Jones (LJ) intermolecular potential (σ_{LJ} and ϵ_{LJ} described later in Section 2.6) are also used; making it a total of six molecular model parameters.

2.5 Born-Mayer Exponential Repulsive Model

The Born-Mayer exponential repulsive model [35] utilizes an exponential function to represent the repulsion resulting from the interaction of electron clouds. Thus, the potential may be expressed as

$$\phi(r) = A\mathrm{e}^{-\alpha r}\,, \tag{2.47}$$

where A is a scaling parameter and α is the interaction range parameter. These parameters are set depending on the interaction pair. Inverse power models are known not to be "soft" enough at higher collision energies, and therefore the exponential function is preferred under these circumstances. [28]

Scattering angles, transport cross-sections, collision integrals, and properties must all be evaluated numerically from Eqs. (2.6)– (2.19). Details of computing the microscopic and macroscopic properties from an arbitrary potential are provided in Section 2.8.

2.6 Lennard-Jones (L-J) Model

The Lennard-Jones (L-J) model [11] is a combination of two inverse power models: repulsive and attractive. Thus, the L-J model represents a more physically realistic intermolecular potential and may be written in general terms as

$$\phi(r) = 4\epsilon\left[\left(\frac{\sigma}{r}\right)^q - \left(\frac{\sigma}{r}\right)^n\right]\,. \tag{2.48}$$

The sign of the terms dictates whether it is repulsive or attractive, and therefore the first term which depends on r^{-q} is repulsive while the second term depending on r^{-n}

is attractive. Since repulsive forces dominate at short distances and the dispersion forces for neutral atoms are on the order of r^{-6}, the most common values of q and n are 12 and 6. These are the values used throughout the remainder of the dissertation and reference to L-J potential will imply the (12-6) L-J potential.

Although an analytic expression for the scattering angle may not be obtained, a simpler form has been obtained by Matsumoto and Koura [36]. The scattering angles may thus be evaluated from the integral,

$$\chi = \pi - 2\sqrt{1+cz-(1+c)z^2}\int_0^1 \{1-[1+cz-(1+c)z^2]u^2+czu^6-(1+c)z^2u^{12}\}^{-1/2}du, \tag{2.49}$$

where $c = (2/\epsilon^*)[1+\sqrt{1+\epsilon^*}]$, $z = (4/c\epsilon^*)(\sigma_{LJ}/r_{min})^6$, and $u = r_{min}/r$. The distance of closest approach between the two molecules is denoted by r_{min}; while the reduced relative collision energy is a ratio of the relative collision energy to the L-J potential well depth, $\epsilon^* = \epsilon/\epsilon_{\mathrm{LJ}}$. A reduced form of the impact parameter is also used, where the impact parameter is non-dimensionalized by the intermolecular separation distance of zero energy, $b^* = b/\sigma_{\mathrm{LJ}}$. Varying u from 0 to 1 varies r from ∞ to r_{min}. z in the above integral depends on b^* and ϵ^* and is obtained by solving the implicit equation,

$$b^* = \left(\frac{4}{c\epsilon^*}\right)^{1/6}\sqrt{1+cz-(1+c)z^2}z^{-1/6}. \tag{2.50}$$

For practical use in the direct simulation Monte Carlo (DSMC) method [1] the L-J polynomial approximation (LJPA) model was developed by Venkattraman and Alexeenko [37] which replaces the complicated scattering angle calculation in Eq.(2.49) with a simpler, two-dimensional, seventh-order polynomial of the form,

$$\chi(\epsilon, b) = \sum_{i=0}^{7}\sum_{j=0}^{7-i}\hat{\chi}_{ij}\hat{b}^{*i}\hat{\epsilon}^{*j}. \tag{2.51}$$

The two variables, $\hat{b}^*$ and $\hat{\epsilon}^*$, are non-dimensional numbers related to the impact parameter and relative translational collision energy, respectively; while $\hat{\chi}_{ij}$ are the polynomial coefficients. Refer to Ref [37] for more details. Collision integral tables similar to those found in table 1-M of Ref [30] may be computed using the LJPA

scattering as a function of non-dimensional temperature, $T^* = kT/\epsilon$. These reduced collision integral tables using the LJPA scattering have been included in Appendix A

2.7 Morse Model

The Morse potential uses an exponential function, like the Born-Mayer model, to model the repulsive as well as the attractive forces. The Morse potential,

$$\phi(r) = \epsilon \left[e^{-2(c/\sigma)(r-r_e)} - 2e^{-(c/\sigma)(r-r_e)} \right], \tag{2.52}$$

where ϵ is the potential well depth, r_e is the equilibrium separation distance, σ is the location of zero potential energy, and c is a shaping factor. The Morse potential has one more model parameter than the L-J potential, and the model parameters may be set to an L-J -like potential through the following relations:

$$r_e = r_m = 2^{1/6}\,\sigma, \quad c = \left(\frac{\sigma}{r_e - \sigma} \right) \ln(2)\,. \tag{2.53}$$

2.8 Numerical Procedure for Arbitrary Potentials

The methodology used for computing scattering angles from arbitrary intermolecular potentials follows similarly to that described by Colonna and Laricchiuta [38]. First, the distance of closest approach, r_{min}, in Eq. (2.7) must be obtained numerically for all but the simplest of potentials. Multiple roots are possible, but it is the maximum root which is needed. Therefore, several initial guesses for the secant method are used to converge to a root and are compared for the maximum. Adaptive quadrature is employed to efficiently evaluate the scattering integral of Eq. (2.6) for arbitrary potentials. The trapezoidal rule is used in each interval $[a, b]$,

$$I_{1,ab} = \frac{1}{2}\left(f(a) + f(b)\right) \tag{2.54}$$

$$I_{2,ab} = I_{1,ac} + I_{1,cb}, \quad c = \frac{a+b}{2} \tag{2.55}$$

and the number of intervals is increased until the difference in the integrals $I_{1,ab}$ and $I_{2,ab}$ is less than a specified tolerance. A large value on the order of 10^{10} is used as an approximation to the upper limit of integration, ∞.

A maximum reduced impact parameter, $b^*_{max} = b/\sigma$, must be determined as a function of relative collision energy. In theory, this value extends to infinity for the L-J and Morse potentials, but this is computationally impractical. Following the work of Koura and Matsumoto [9], a minimum cut-off angle is instead introduced such that impact parameters which result in less scattering are neglected. Thus, the impact parameter which results in scattering equal to the minimum cut-off scattering angle is defined as b^*_{max}. The minimum cut-off scattering angle used for comparisons in this work is 0.001 radians unless otherwise stated. The collision diameter is then $d = b_{max}$, and the total collision-cross section is computed for the circular area as $\sigma_T = \pi d^2$.

Scattering angles are anyways required in particle based methods such as the direct simulation Monte Carlo method [1], and therefore scattering angles are pre-computed for a large number of relative collision energies and impact parameters. On the order of one million scattering angles are computed; with reduced collision energies ranging from 10^{-5} to 10^3 and reduced impact parameters incremented by 0.005 until the maximum impact parameter specified by b^*_{max} is reached. The range of the reduced collision energy is increased and the increment of the reduced impact parameter is decreased until convergence and agreement with literature is sufficient (less than 1%). Cubic splines are fit for scattering angles as a function of impact parameter for each relative collision energy. Using these splines, the same adaptive quadrature method is employed to evaluate the integral for the transport cross-sections, Eq. (2.9). Cubic splines are then fit for transport cross-sections as a function of relative collision energy in order to evaluate the transport collision integrals, Eq. (2.11).

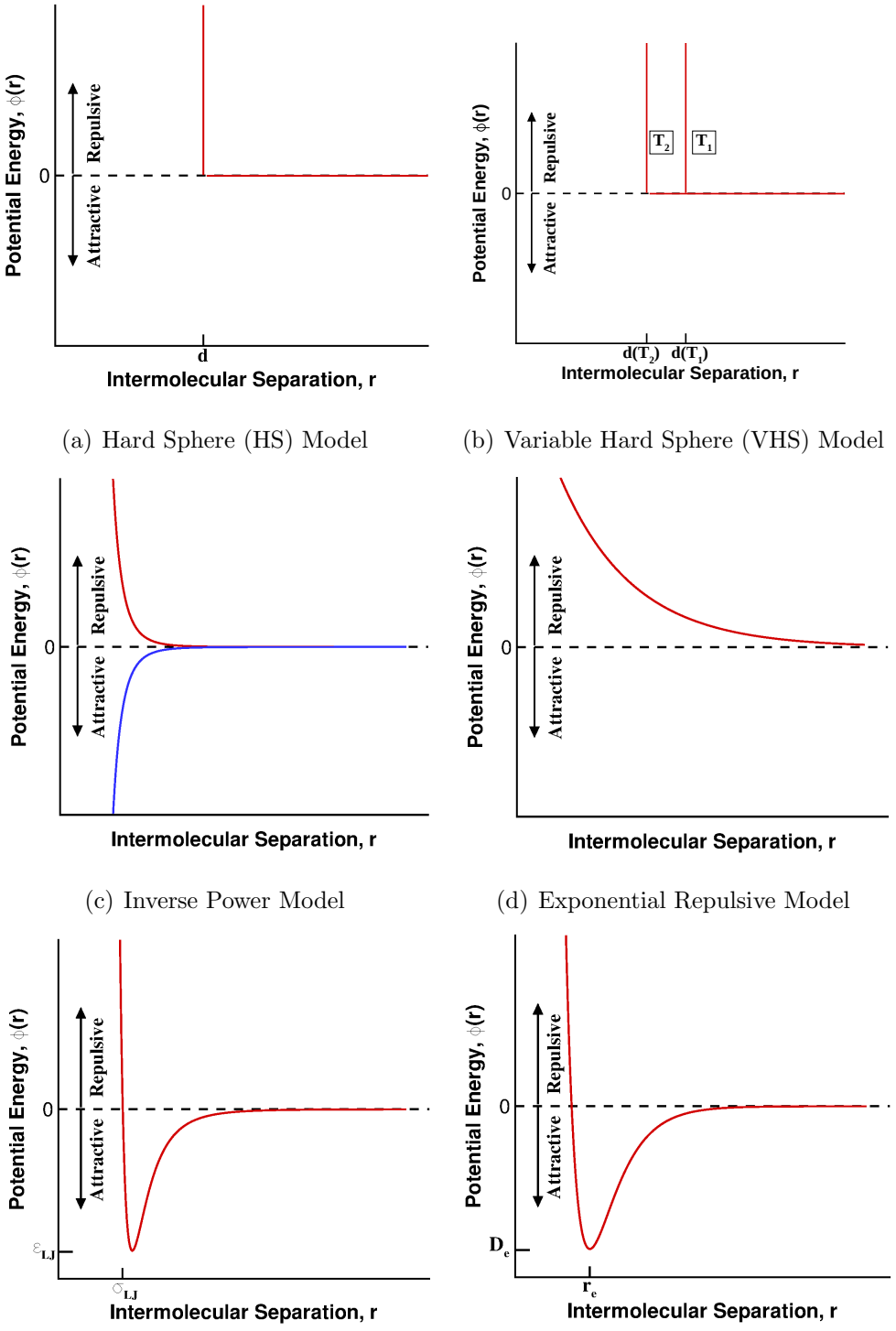

(a) Hard Sphere (HS) Model

(b) Variable Hard Sphere (VHS) Model

(c) Inverse Power Model

(d) Exponential Repulsive Model

(e) Lennard-Jones (L-J) Model

(f) Morse Model

Figure 2.4.. Schematics of common intermolecular potentials

3. INTRODUCTION TO THE DSMC METHOD

The study of gas flows at the microscopic level is required when the continuum hypothesis fails. This may occur in low-density environments such as in high-altitude flight or in vacuum manufacturing processes or at small length scales such as in micro/nano-electrical-mechanical systems (MEMS)/(NEMS) devices. In such instances, the Navier-Stokes equations in continuum fluid dynamics do not apply and instead the Boltzmann equation shown in Eq. (3.1) is used.

$$\frac{\partial}{\partial t}(nf) + \vec{c}\cdot\frac{\partial}{\partial \vec{x}}(nf) + \vec{F}\cdot\frac{\partial}{\partial \vec{c}}(nf) = \int_{-\infty}^{\infty}\int_{0}^{4\pi} n^2\left(f^* f_1^* - f f_1\right) c_r \sigma \, \mathrm{d}\Omega \, \mathrm{d}\vec{c}_1 \qquad (3.1)$$

The physics that the Boltzmann equation represents is the intermolecular interaction in a dilute gas. The number of molecules crossing a surface may be affected by transient processes, convection, external forces, or collisions with other molecules. These contributors to the change in number flux across a surface are expressed in the four terms in Eq. (3.1), respectively, where n is the number density, f and f^* are the pre- and post-collision velocity distribution functions, $\vec{c}$ is the macroscopic velocity, $\vec{F}$ is the external force, σ is the collision cross-section, and $\mathrm{d}\Omega$ is the unit solid angle.

At the microscopic level there exists intermolecular forces acting between particles governing the dynamics of particle collisions. The air we breathe consists of molecules which are colliding with each other on the order of 10 billion times every second. The outcome of each collision - in what directions do the molecules move and with what velocity - is determined from the intermolecular potential energies of the colliding molecules along with the initial conditions. Particle motion may be described knowing the current positions as well as velocities. Thus, after collisions new particle positions may be determined. Macroscopic fluid properties are simply averages of microscopic properties sampled from all particles in a region. This leads to one of the most

common approaches to computing flow fields for rarefied gas flows, the DSMC method. [1]

The DSMC method does not directly solve the Boltzmann equation of Eq. (3.1), but rather simulates the real physics the Boltzmann equation represents. DSMC proceeds through four main processes: (1) indexing, (2) moving, (3) collisions, and (4) sampling. This flowchart is illustrated in Figure 3.1; where the processes are repeated until the specified number of samples are taken. The procedure begins with indexing the molecules.

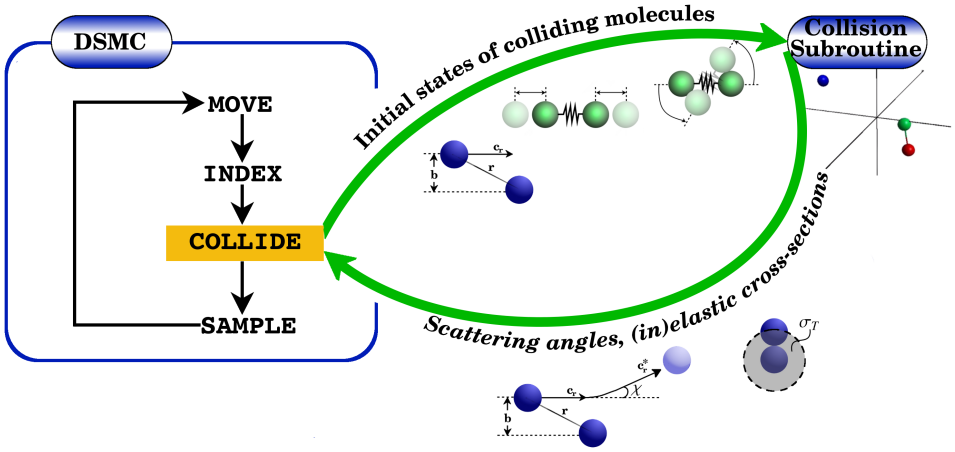

Figure 3.1.. Flowchart of the DSMC process

DSMC uses a spatial grid to contain the simulated molecules and perform sampling. Often times, separate grids are used for performing collisions and sampling, [1] as depicted in Figure 3.2. Individual simulated molecules must be tracked, and therefore the *index* subroutine is used to track which molecules are in which collision and sampling cells. Repeated calling of the *index* subroutine is necessitated by molecular movement.

The *move* subroutine moves each molecule according to their velocity a distance appropriate for the specified time step. This velocity is assumed constant over each time step. The velocity of a molecule is changed either by external forces, such as

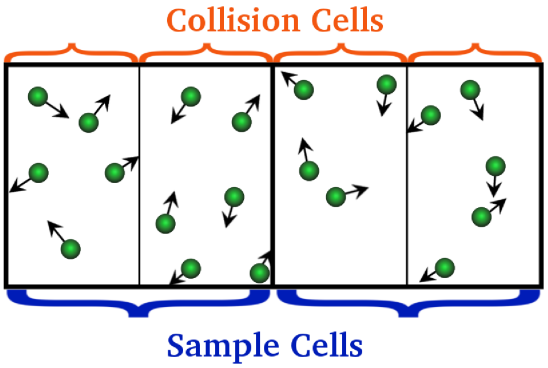

Figure 3.2.. Schematic of a DSMC sub-layered grid

electrostatic forces, or by the scattering resulting from a collision. In the absence of external forces, the velocity will only change as a result of a collision.

A collision may be classified as either elastic or inelastic. Elastic collisions refer to collisions in which the total kinetic energy is unchanged. This means no energy is transferred between the various energy modes. Atoms have two energy modes, translational and electronic; while molecules possess two additional energy modes, vibrational and rotational. Characteristic temperatures of the electronic modes of air species are more than 10,000 K and may therefore be neglected for hypersonic flows with moderate Mach numbers ($M < 10$). At higher Mach numbers more typical of reentry, however, sufficient energy is available to not only excite the electronic modes, but also ionize the gas species. The interaction of charged particles creates an electric field and is outside the scope of the DSMC method. It is often times modeled with another particle-based method known as particle-in-cell Monte Carlo [39] (PIC-MCC).

The *collide* subroutine includes both elastic and inelastic collisions, and being a statistical method randomly selects a pair of molecules to collide using the acceptance-rejection method. [1] The collision is accepted with a probability,

$$P = \frac{\sigma c_r}{(\sigma c_r)_{max}}, \tag{3.2}$$

where $(\sigma c_r)_{max}$ is the maximum, effective volume swept out by a molecule. This maximum value is recorded in each sampling cell such that each cell may have a separate collision frequency. With this in mind, the goal of the *collide* subroutine is not only to determine scattering angles and post-collision energies, but also to obtain correct collision frequencies and macroscopic properties.

There are several methods to perform collision sampling, with the most prevalent being Bird's time-counter [40] (TC) and no-time-counter [1] (NTC) methods, Koura's null-collision method [41], and Ivanov's majorant frequency scheme [42] (MFS). The differences lie in how the collision times are accounted for in the collision probabilities. The collision sampling method employed in this work is the NTC method, where the number of collisions is computed outside of the *collide* subroutine. Thus, no separate time counter is required to reach flow time as the other methods do.

This leads to the last subroutine, *sample*, which is performed over all sampling cells to determine macroscopic properties. The microscopic properties from each simulated molecule (molecular velocities and translational, rotational, and vibrational energies) are averaged in each cell to compute the macroscopic properties such as density, bulk velocity, pressure, and translational, rotational, and vibrational temperatures. For example, the density in a cell is the sum of the mass from each of the N particles, $m_{i,cell}$, divided by the cell volume,

$$\rho_{cell} = \frac{1}{V_{cell}} \sum_{i=1}^{N} m_{i,cell} \, . \tag{3.3}$$

A mass-weighted average may be used as the bulk velocity in a cell when gas mixtures are present, [1]

$$\vec{v}_{cell} = \sum_{i=1}^{N} \frac{m_{i,cell} \vec{c}_{i,cell}}{m_{i,cell}} \, , \tag{3.4}$$

where $\vec{c}_{i,cell}$ is the molecular velocity vector of the $i-th$ particle in the cell.

The translational temperature is the average kinetic energy, and is therefore [1]

$$T_{t,cell} = \frac{1}{3kN} \sum_{i=1}^{N} \left(m_{i,cell} \left| \vec{c}_{i,cell} \right|^2 - m_{i,cell} \left| \vec{v}_{cell} \right|^2 \right) \, . \tag{3.5}$$

Through equipartition of energy, the average temperature for any energy mode may be related to its number of degrees of freedom by

$$\bar{E}_{mode} = \frac{\bar{\eta}}{2} k T_{mode} \,. \tag{3.6}$$

Thus, Eq. (3.6) may be rearranged to solve for T_{mode} where now we are interested in the rotational energy mode.

Again, temperature is an averaged quantity so summations over all simulated molecules in the cell are used to compute the rotational temperature,

$$T_{r,cell} = \frac{2}{k} \frac{\sum_{i=1}^{N} q_{i,cell} \Theta_{r,i}}{\sum_{i=1}^{N} \eta_{i,cell}} \,. \tag{3.7}$$

The rotational energies are quantized, and therefore the rotational levels, $q_{i,cell}$, are integers beginning with zero. Note that each molecular species may have different characteristic rotational temperatures, Θ_r, and even different characteristic temperatures within the same molecule if several rotational modes are present.

The vibrational temperature of species p may be determined from the Boltzmann distribution. Taking the ratio of the number of molecules in level 1 to level 0 in the cell results in the following for the Boltzmann distribution.

$$\frac{N_0}{N_1} = \mathrm{e}^{(E_{v,1} - E_{v,0})/k T_{v,p}} \tag{3.8}$$

This expression may be rearranged to determine the vibrational temperature, $T_{v,p}$, as

$$T_{v,p} = \frac{E_{v,1} - E_{v,0}}{k \, \ln\left(N_0/N_1\right)} \,. \tag{3.9}$$

Since the characteristic vibrational temperature energy spacing between vibrational levels zero and one is nearly the same for harmonic and anharmonic oscillators, the characteristic vibrational temperature, Θ_v, may be substituted into Eq. (3.9).

$$T_{v,p} = \frac{\Theta_{v,p}}{\ln\left(N_0/N_1\right)} \tag{3.10}$$

Again, each species may have different characteristic vibrational temperatures and even a single species may have several characteristic vibrational temperatures corresponding to each vibrational mode. Also note that it is possible to use a ratio of any

vibrational levels, or an average of multiple, sequential ratios. However, it is preferable to use the lowest vibrational levels since these levels will almost always be more populated than upper levels. Remember that although the Boltzmann distribution has some non-zero population values for each vibrational level, only a finite number of molecules may be simulated in DSMC. Therefore, if the theoretical population values are too small, then there will likely be an insufficient number of simulated molecules to populate such vibrational levels.

Now that the vibrational temperature for each species has been defined, the average vibrational temperature for the entire cell may be determined. This is again relating back to the equipartition of energy in Eq. (3.6). Thus, the vibrational temperature in the cell is

$$T_{v,cell} = \frac{2}{k} \frac{\sum_{i=1}^{N} \eta_{v,i,cell} T_{v,i,cell}}{\sum_{i=1}^{N} \eta_{v,i,cell}} \,. \tag{3.11}$$

Finally, the overall temperature in the cell is the summation over all the energy modes, [1]

$$T_{cell} = \frac{3T_{t,cell} + T_{r,i,cell} \sum_{i=1}^{N} \eta_{r,cell}/N + T_{v,cell} \sum_{i=1}^{N} \eta_{v,i,cell}/N}{3 + \sum_{i=1}^{N} \eta_{r,i,cell}/N + \sum_{i=1}^{N} \eta_{v,i,cell}/N} \,, \tag{3.12}$$

where the factor, 3, for the translational mode comes from the three degrees of freedom.

4. ELASTIC COLLISION MODELING

4.1 Effect of Intermolecular Potential on Transport Property Calculations

Several variations were proposed to the VHS model including the variable soft sphere (VSS) [9], generalized hard sphere (GHS) [34] and generalized soft sphere (GSS) [43] which all belong to a class of purely repulsive interactions. The VSS model modifies the scattering law of the VHS model by using a parameter that allows reproduction of measured diffusion coefficients in addition to viscosity coefficient. The GHS model uses the same scattering law as the VHS model but applies a modified collision cross-section with parameters chosen to reproduce both viscosity and diffusion coefficients. The GSS model has a cross-section similar to GHS model but with a scattering law similar to the VSS model and has fewer parameters than the GHS model. Dimpfl et al. [44] used the Born-Mayer potential with a hard sphere scattering kernel to develop what is referred to as the Extended-VHS (EVHS) model to deal with hyperthermal gas flows. Other collision models such as the μ-DSMC method [45] can reproduce arbitrary viscosity variation with temperature by adjusting parameters of the hard sphere model in each cell based on the local time-averaged temperature. In summary, the parameters of all these models are determined in such a way that they match observed or theoretical bulk transport properties such as viscosity and diffusion coefficients.

Each of these models have limited validity due to the fact that they do not account for the attractive force between molecules at large distances. With the exception of the GSS model, most of these models are limited to a relatively narrow temperature range in which the viscosity variation is accurately reproduced. For problems involving a wide range of temperatures, this would be insufficient. Examples include flows

with large temperature variations such as supersonic plume expansions in vacuum as encountered in space propulsion and in low-pressure deposition of thin film materials where the vapor temperature varies from the melting point of the material to very low temperatures due to rapid expansion into vacuum. In other applications the detailed collision dynamics that includes the contribution of the attractive interactions between molecules becomes important. For example, this is the case when the orientation of a molecule incident on a solid surface should be accurately predicted along with the incident energy of the molecule for thin film growth modeling.

Implementation of realistic repulsive-attractive interaction potentials in DSMC simulations have been reported in the past [36, 46] but has never been used widely. One of the popular attractive-repulsive interaction potential is the Lennard-Jones (LJ) potential which is known to accurately represent the interaction of molecules and was used by Koura and Matsumoto [36] in DSMC simulations to investigate the velocity distribution functions within an argon shock wave at free-stream temperatures much lower than the potential well depth of argon. Their implementation used numerical integration to obtain the elastic scattering angle for every collision. More recently, Valentini and Schwartzentruber [47] performed large scale molecular dynamics simulations to revisit the computation of velocity distribution functions within an argon shock wave. They reported significant differences between the DSMC computations with the VHS model and the molecular dynamics simulations with the LJ potential. Sharipov and Strapasson [48] demonstrated a data look-up table implementation in DSMC, applicable for arbitrary intermolecular potentials, and applied it to Couette and Fourier flows using the LJ potential. An approach presented recently [37] reduces the computational cost relative to direct implementation by representing the scattering angle as a polynomial expansion in non-dimensional collision parameters and is referred to as the LJ polynomial approximation (LJPA) model. In the aforementioned studies [36, 37, 46–48], the focus has been either on demonstrating new numerical schemes for implementing the LJ potential in DSMC, or evaluating the accuracy of the VHS model in normal shock waves near continuum. The aim here is

to quantify the differences in transport properties between the widely used, repulsive VHS model and the attractive-repulsive LJ model for a variety of flow regimes. [49]

4.1.1 Comparison of VHS and LJ Potential Elastic Scattering

Since there is no general relation between the parameters of the LJ potential and the VHS model, comparisons of the scattering angle for the two cases can be made only for a given gas. Figure 4.1 shows contours of the scattering angle obtained using the VHS model and the LJ potential computed using parameters for Argon. The relevant parameters were: $\sigma_{LJ} = 3.405\times10^{-10}\ m$, $\epsilon_{LJ} = 0.0103\ eV$, $d_{\text{ref}} = 4.17\times10^{-10}\ m$ at 273 K, and $\omega = 0.81$. As can be observed, there are significant differences for a range of b^* and ϵ^* values. The differences are pronounced for low energy collisions, as can be observed from the contour lines close to the x-axis, and also for long-range collisions corresponding to values of $b > d_{VHS}$. Figure 4.2 shows the variation of χ as a function of b^* for four different values of ϵ^* in order to compare the LJ potential, VHS model and GSS model scattering angles more rigorously. Since the VHS and GSS models are purely repulsive models, negative values of scattering angle are not obtained while the LJ potential has a shallow well for χ even at relative energies of ϵ^* = 5.0. For the lowest value of ϵ^* shown, the GSS model leads to a very large collision cross section as mentioned earlier. The mean translation energy of collisions in the center of mass frame for VHS model is given by Bird [1] as

$$\bar{E}_t = (2.50 - \omega)kT. \tag{4.1}$$

For a temperature of 273 K, the mean translation energy of collisions is 0.0397 eV and corresponds to $\epsilon^* = 3.86$ for argon. On the other hand, for a temperature of 40 K, the mean translation energy of collisions is 0.0058 eV corresponding to $\epsilon^* = 0.57$. The effect of negative scattering angles due to the attractive component of the force between molecules is more important at 40 K than at 273 K.

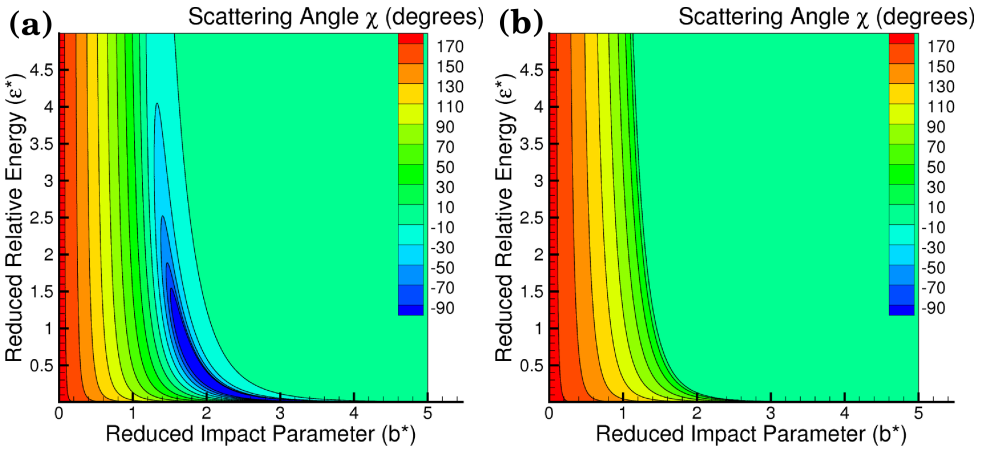

Figure 4.1.. Comparison of scattering angle contours for the (a) LJ potential and (b) VHS model.

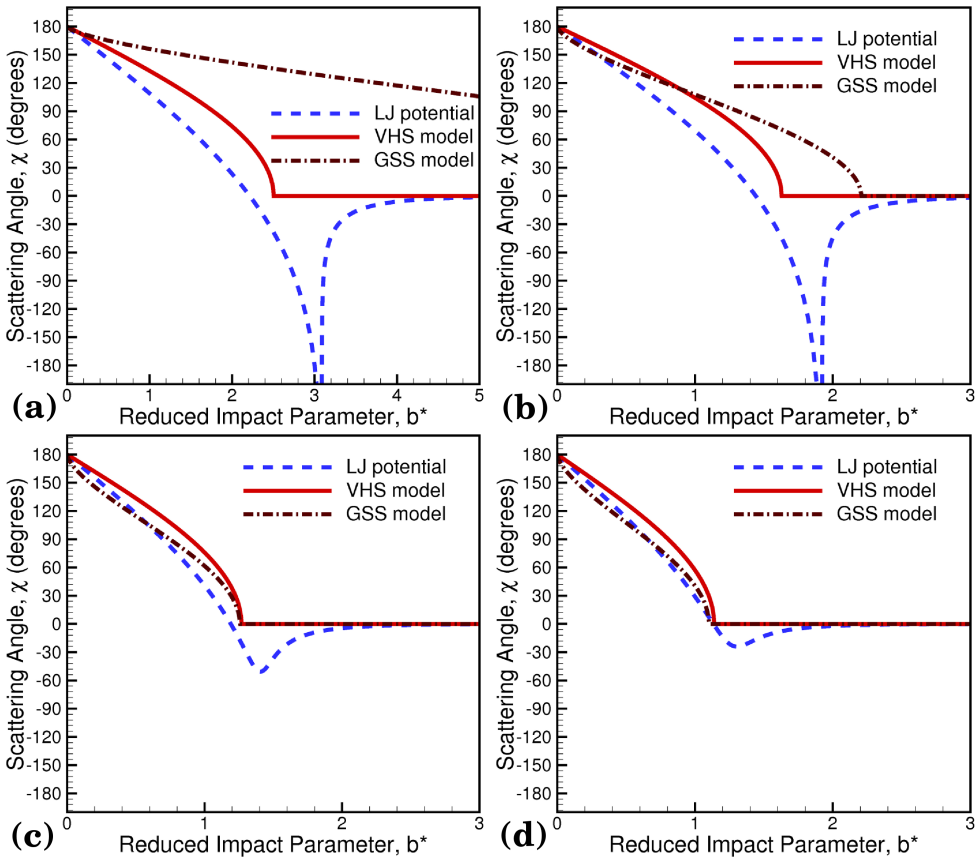

Figure 4.2.. Variation of χ as a function of b^* for (a) $\epsilon^* = 0.031$, (b) $\epsilon^* = 0.5$, (c) $\epsilon^* = 2.5$, and (d) $\epsilon^* = 5.0$

4.1.2 Verification of LJPA Model

The LJPA model is verified through comparison of equilibrium collision frequencies computed at several temperatures to theory. Equilibrium collision frequency is computed as a product of number density and the mean of the product of total cross-section and relative velocity. The mean of the product, $\overline{\sigma_T c_r}$, is averaged over

the relative velocity distribution function, f_{c_r}, such that the equilibrium collision frequency has the form [1],

$$\nu_0 = n\overline{\sigma_T c_r} \tag{4.2}$$

$$= n\int_0^\infty \sigma_T c_r f_{c_r}\,\mathrm{d}c_r \tag{4.3}$$

$$= 4n\frac{m_r^{3/2}}{\sqrt{\pi}\,(2kT)^{3/2}}\int_0^\infty \left(\pi b_{max}^2\right) c_r^3\,\exp\left[-\frac{m_r c_r^2}{2kT}\right]\,\mathrm{d}c_r\,. \tag{4.4}$$

The total cross-section for the LJ potential would theoretically extend to infinity, and therefore a maximum impact parameter [9, 37],

$$b_{max} = \sigma_{LJ}\max\left[\left(\frac{4\pi}{\epsilon^*\chi_{min}}\right)^{\frac{1}{6}}, \left(\frac{6\pi}{\epsilon^*\chi_{min}}\right)^{\frac{1}{12}}\right], \tag{4.5}$$

is set to a value beyond which scattering angles less than χ_{min} are neglected. This variation of total cross-section with relative velocity also necessitates the use of numerical integration techniques, such at those described in Section 2.6. In this section, as well as in the remainder of the paper, a minimum scattering angle of 0.1 radians is used.

The DSMC implementation of the LJ potential itself follows the work of Koura and Matsumoto [36] very closely with the principal difference being the use of the polynomial expansion for the scattering angle instead of a concurrent numerical integration. To reiterate, the reduced impact parameter, b^*, is uniformly distributed between 0 and b_{max} once a collision pair is chosen, and then the elastic scattering angle for the chosen collision pair is obtained using the LJPA model described in detail in Ref [37]. The DSMC simulations were performed using the one-dimensional code of Bird [1], DSMC1.FOR, after implementation of the LJPA model.

Collision frequencies are computed from DSMC using both the LJPA model and the direct LJ scattering from the integral,

$$\int_0^1 I(u)du = \sum_{k=0}^{M-1}\frac{1}{2}w_k I\left(\frac{y_k+1}{2}\right)\sqrt{1-y_k^2}, \tag{4.6}$$

where w_k are the weights for Gauss-Chebyshev quadrature, y_k are the zeros of the M^{th} degree Chebyshev polynomial denoted by ϕ_M, and I is the integrand of Eq.(2.49) given by

$$I(u) = \{1 - [1 + cz - (1 + c)z^2]u^2 + czu^6 - (1 + c)z^2u^{12}\}^{-1/2}. \tag{4.7}$$

The zeros, y_k, of ϕ_M are given by

$$y_k = \cos\left(\frac{(2k + 1)\pi}{2M}\right), \tag{4.8}$$

and the weights are all equal to

$$w_k = \frac{\pi}{M}. \tag{4.9}$$

A single cell of length, 1 mm, with 40,000 molecules and a number density corresponding to $Kn = 10$ is used. A time-step of $\tau_0/10$ is used, where τ_0 is the mean collision time as computed from theory ($1/\nu_0$). DSMC sampling speeds of each LJ scattering angle implementation are recorded using a single processor on the Hansen compute cluster. The Hansen compute cluster has four 2.3 GHz 12-Core AMD Opteron 6176 processors per node, 10GB Ethernet interconnections, and 48.8 TeraFLOPS performance. Sampling speeds for the LJPA model ranged from 33.0 samples/s to 39.9 samples/s; while the direct LJ scattering implementation resulted in approximately half the sampling speed of 14.9-15.1 samples/s. Collision frequencies computed from DSMC and theory are reported in table 4.1 along with their corresponding errors relative to theory.

The statistical errors reported as a two-sided 95% confidence interval are much smaller than the errors in collision frequency relative to theory; thus providing confidence in the results. Both DSMC implementations of the LJ scattering angle have comparable collision frequencies at each of the simulated temperatures, and are in error by less than 0.02%. The good agreement verifies the implementation of the LJPA model in DSMC, and the errors are consistent with both those reported for the VHS model at 300 K [50] and for the VSS model in table 4.2.

Table 4.1.. LJ Collision Frequencies Computed from DSMC and Theory

$T(K)$	$\nu_{LJPA}(Hz)$	$\nu_{Direct}(Hz)$	$\nu_{Theory}(Hz)$	ν_{LJPA} Error (%)	ν_{Direct} Error (%)
40	$25,813.2 \pm 0.1$	$25,812.5 \pm 0.1$	25,808.4	0.019	0.016
273.15	$66,130.7 \pm 0.5$	$66,128.4 \pm 0.3$	66,117.8	0.020	0.016
1,000	$129,090.9 \pm 1.$	$129,085.8 \pm 0.6$	129,084.5	0.005	0.001
1,500	$154,932.6 \pm 0.4$	$154,926.5 \pm 1.$	154,936.4	-0.002	-0.006

Table 4.2.. VSS Collision Frequencies Computed from DSMC and Theory

$T(K)$	$\nu_{VSS}(Hz)$	$\nu_{Theory}(Hz)$	ν_{VSS} Error (%)
40	$14,566.1 \pm 0.1$	14,563.5	0.018
273.15	$37,053.3 \pm 0.3$	37,044.3	0.024
1,000	$72,855.0 \pm 0.3$	72,837.5	0.024
1,500	$86,838.5 \pm 0.7$	86,817.8	0.024

4.1.3 Couette Flow Simulations in the Slip Regime

The LJPA model is evaluated by initially using it in DSMC simulations of compressible subsonic and supersonic Couette flow problems similar to those used by Bird [1] to verify the VHS model and Macrossan [45] to verify the μ-DSMC technique. The three cases each have all the same initial conditions and numerical parameters, and only differ by the specified wall temperature. Use of the same number density and wall velocity results in differing Knudsen numbers, Kn, and Mach numbers, M, between the cases, respectively. The flow conditions for each of the three cases as well as the numerical parameters used are summarized in table 4.3.

Table 4.3.. Summary of flow conditions and numerical parameters used for the subsonic and supersonic Couette flow cases

Quantities	Case 1	Case 2	Case 3
Wall Temperature, T_{wall} (K)	273	40	1,000
Initial Number Density, n $(1/m^3)$	1.4×10^{20}	1.4×10^{20}	1.4×10^{20}
Moving Wall Velocity, v_{wall} (m/s)	300	300	300
Mach number, M	0.97	2.55	0.51
Knudsen number, Kn	0.012	0.0051	0.017
$\langle \epsilon^* \rangle$ based on wall temperature	3.86	0.57	12.1
Wall Separation, L (m)	1	1	1
$\epsilon_{LJ}(eV)$	0.0103	0.0103	0.0103
$\sigma_{LJ}(\mathring{A})$	3.405	3.405	3.405
ω	0.81	0.81	0.81
$d_{ref}(\mathring{A})$	4.17	4.17	4.17
$T_{ref}(K)$	273	273	273
$\Delta t(\mu s)$	1	1	1
Number of Cells	500	500	500
Number of Particles	10^4	10^4	10^4
Number of Transient Time-Steps	2×10^5	2×10^5	2×10^5
Total Number of Time-Steps	21×10^6	21×10^6	21×10^6

The Knudsen numbers reported in table 4.3 are defined based on the mean free path,

$$\lambda = \frac{2\mu}{\rho\bar{c}}\,, \tag{4.10}$$

obtained using the mean free path theory [51]. The viscosity, μ, is the viscosity corresponding to the wall temperature, ρ is the initial density, and $\bar{c}$ is the mean thermal velocity based on the wall temperature. Apart from the theoretical viscosity, the viscosity in DSMC simulations may be computed given shear stresses and velocity gradients.

Viscosity is computed from DSMC simulations through its relationship to shear stress and velocity gradient. Since both shear stresses,

$$\tau_{\mathrm{DSMC}} = < \rho c_x c_y >\,, \tag{4.11}$$

and velocity gradients, $\partial v/\partial x$, are directly calculated from microscopic properties, viscosity may then be determined through the relationship

$$\mu_{DSMC} = \frac{\tau_{DSMC}}{(dv/dx)_{DSMC}}\,. \tag{4.12}$$

The brackets, $< \ldots >$, in the expression for shear stress (Eq. 4.11) denote an average value. In the sections that follow, reported average viscosity and shear stress values are averaged over the central 60% of the domain. This averaging procedure is used in order to exclude the Knudsen layer, which extends several mean free paths from the walls. The sampled viscosities and shear stresses have statistical errors inherent to the DSMC method, but are estimated to be below 0.2% and 0.001% for viscosity and shear stress, respectively.

Case 1: Moderate-Temperature, Subsonic, Slip Flow

For the compressible, subsonic Couette flow problem, a moderate wall temperature of 273 K was chosen. This temperature corresponds to the reference temperature for the VHS model, and as such the VHS model is expected to perform well in this case. The Kn for this wall temperature is 0.012 and is therefore in the slip regime.

Figure 4.3 compares the variation of normalized temperature obtained using the VHS model and the LJPA model. The agreement between the two models is excellent with the maximum difference in normalized temperature being 0.12%. The only non-zero shear stress component for the Couette flow is $\tau_{xy} = \tau_{yx}$ which is computed directly by the DSMC simulation. The difference between velocities obtained assuming incompressible Couette flow, $v_{inc} = v_{wall}\, X/L$, and those from DSMC simulations may be observed in Figure 4.3. Due to the larger mean free path between collisions under the conditions of Case 1, the flow is characterized by the slip regime and hence a velocity slip is observed near the walls. The deviation from incompressible Couette flow is comparable between the LJPA and VHS models.

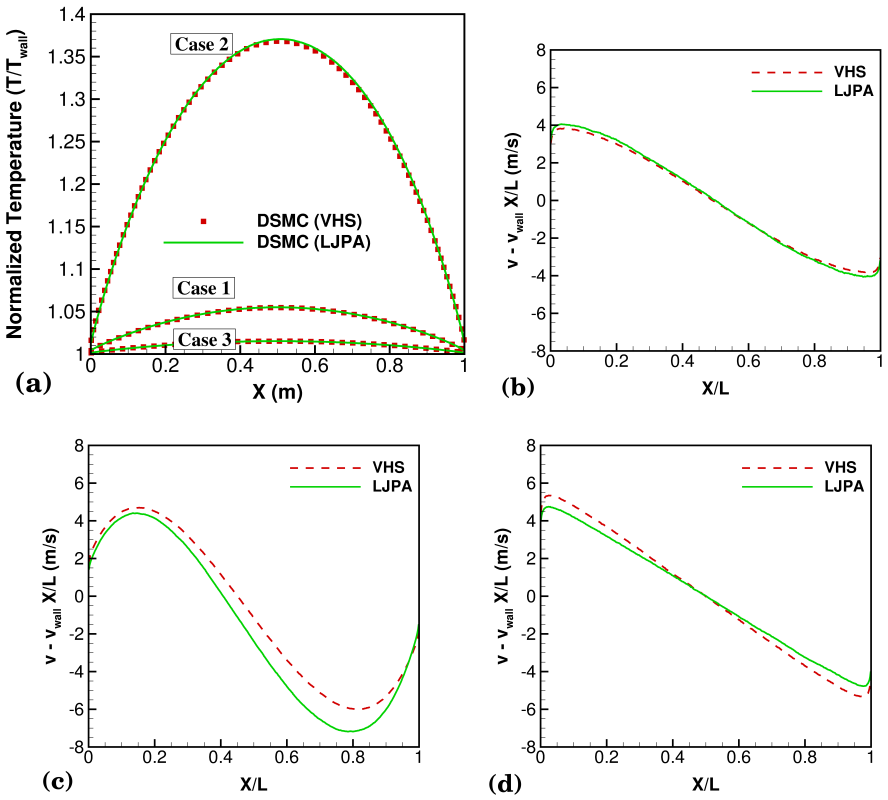

Figure 4.3.. Comparison of (a) normalized temperatures for Cases 1-3, (b) velocity variation for Case 1, (c) velocity variation for Case 2, and (d) velocity variation for Case 3, in the gap obtained using VHS and LJPA models

Figure 4.4 compares the shear stress variation in the gap, which has to be constant across the gap for the Couette flow, obtained using the VHS model and the LJPA model. Since the viscosity obtained using VHS model and LJ potential agree very well at 273 K the difference in shear stress is expected to be small. The average values of shear stress, including statistical error estimates, obtained using the VHS model and LJPA model are 6.28 $\times 10^{-3}$ Pa and 6.60 $\times 10^{-3}$ Pa; which corresponds to a difference of about 5%.

Viscosities obtained from DSMC simulations are compared to the theoretical viscosities obtained using the LJ intermolecular potential and the VHS model at the local temperature, T_{DSMC} in Figure 4.4. The LJPA model agrees with the theoretical value obtained using the LJ intermolecular potential with an average error of 1.0% in regions outside the Knudsen layer where the DSMC viscosity computed using Eq.(4.12) is not expected to match the theoretical value. The DSMC viscosity obtained using the VHS model agrees with the theoretical value with an average error of 1.15%. Statistical errors are estimated to be less than 0.1% for this case and therefore have negligible effects on the DSMC viscosity comparisons to theory.

Comparisons of theoretical viscosity to the experimental fit of Maitland and Smith [52] are also shown Figure 4.4, where the fit corresponds to the local temperatures, T_{DSMC} at each of the spatial locations. The VHS model is in better agreement with the experimental fit than LJ. While VHS is in error by 4.9%, the LJ model has a 9.5% error. This is expected since the VHS model parameters are based on viscosity measurements made at 273 K.

The difference in shear stress of about 5% for the VHS model and LJPA model reported earlier is a combination of the models deviating to small degrees from the theoretical value and also the LJ theoretical viscosity being about 4% higher than the VHS viscosity at 273 K. The other key aspect that can be observed in Figure 4.4 is the Knudsen layer where the DSMC viscosity deviates from theoretical viscosity. It can also be seen that the Knudsen layer is smaller for the LJPA model due to smaller mean free path.

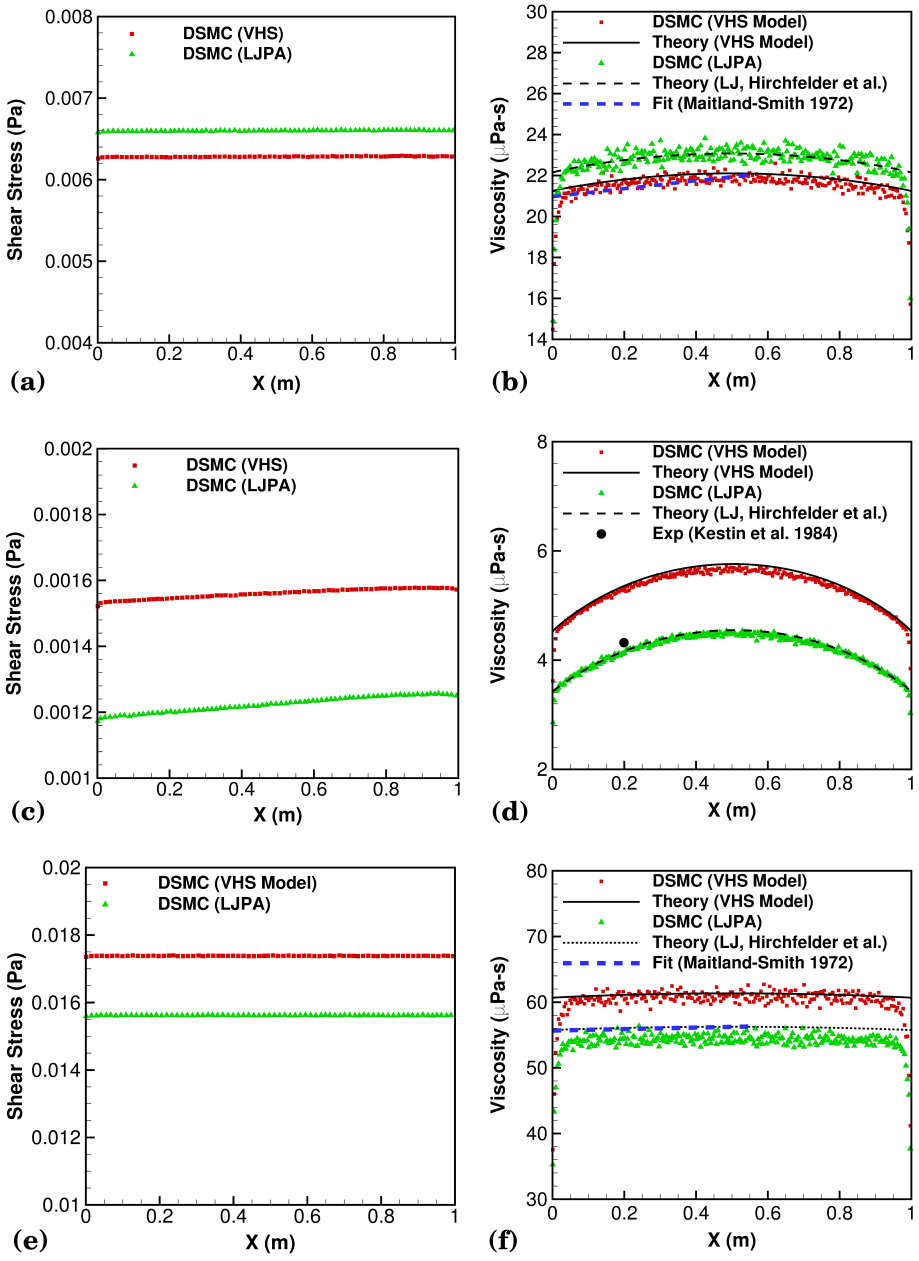

Figure 4.4.. Comparison of (a) shear stress for Case 1, (b) viscosity variation for Case 1, (c) shear stress for Case 2, (d) viscosity variation for Case 2, (e) shear stress for Case 3, and (f) viscosity variation for Case 3, in the gap obtained using VHS and LJPA models

For Case 1, the time taken for 1,000,000 sampling time-steps using the VHS model was 2,288 s whereas for the LJPA model, the time taken was 3,623 s which is about one and a half times larger than that of the VHS model. However, it should be mentioned that most of this increase is contributed by the higher number of collision events due to to the long-range nature of the LJ potential. A collision pair is selected at a rate of approximately 6 for every 10 collision attempts, per the acceptance-rejection method [1], for both VSS and LJPA models. The GSS model which is the closest to the LJPA model in terms of fidelity was also implemented in DSMC1.FOR for comparison with LJPA and VHS models. The ratio of collision events to selections remains about the same for all cases, but the collision frequency significantly changes. Thus, the low-energy collisions in Case 2 result in less collisions occurring each sampling time-step - reducing the computational time required. Applying the same reasoning, Case 3 requires more computational time as a result of the increased collision frequency.

Case 2: Low-Temperature, Supersonic, Slip Flow

The comparison performed for the subsonic compressible Couette flow was repeated for a much lower wall temperature of 40 K, at which differences are expected between the VHS model and the LJ potential. Sound travels much slower at low temperatures, and therefore the Mach number is higher under these conditions than in the other two cases. The Mach number is 2.55 and hence a significant region of the flow in the gap is supersonic as opposed to the other two cases in which the flow never becomes supersonic in the entire gap. The Knudsen number of 0.0051 is approximately half the value for Case 1. All flow conditions and numerical parameters for Case 2 are summarized in Table 4.3.

Figure 4.3 shows a comparison of the normalized temperature and velocity variation in the gap obtained using the VHS and LJPA models. Temperature variation across the gap is more significant for this case due to increased viscous dissipation. While a maximum difference of only 0.4% is observed in the normalized temperature

profile between VHS and LJ models, the velocity profiles for both VHS and LJPA models significantly differ from that of incompressible Couette flow. A linear velocity profile is the analytic solution to an incompressible Couette flow, but this case has compressible, supersonic flow. Thus, the deviation from the analytic solution is greatest in this case. The velocity slip at the wall is the least in this case as a result of the smaller mean free path, and the VHS and LJPA models are in worse agreement than in Case 1.

Figure 4.4 compares the shear stress variation in the gap obtained using the two models and the higher VHS viscosity at temperatures around 40 K leads to a significantly higher shear stress in the gap. A slight increase in shear stress across the gap is observed in both models as a result of the nonlinear velocity profile typical of compressible Couette flow. The average shear stress obtained using the VHS model and the LJPA are 1.22 $\times 10^{-3}$ Pa and 1.56 $\times 10^{-3}$ Pa respectively. This corresponds to a 28% higher shear stress predicted by the VHS model when compared to the LJPA model. In order to verify that the viscosity variation predicted theoretically is reproduced by the DSMC simulations, Figure 4.4 compares μ_{theory} with μ_{DSMC} for both VHS and LJPA models for the supersonic Couette flow. The agreement with theory is good again with the average error being 1.64% for the VHS model and 1.26% for the LJPA model. A viscosity measurement by Kestin et al. [53] at 50 K is also illustrated in Figure 4.4 (shown at a location corresponding to a local temperature of 50 K), and the LJPA model is observed to be in better agreement than the VHS model.

One of the important aspects to be considered in order to evaluate the practical applicability of this method is the computational overhead associated with the polynomial computations. The use of pre-computed scattering angles makes the implementation very efficient with insignificant overhead as compared to the VHS model. The time taken for 1,000,000 sampling time-steps is 2,786 s for the LJPA model; while for the VHS model only 1,961 s is required. Again, the additional time required for

the LJPA model is a result of the higher number of collision events due to to the long-range nature of the LJ potential.

Case 3: High-Temperature, Subsonic, Slip Flow

The behavior of the LJPA and VHS models are studied at higher temperatures in this case. A wall temperature of 1,000 K is set with the same wall velocity as in previous cases. The Knudsen number is 0.017, which indicates the flow is in the slip regime similar to Case 1. The Mach number for this case is 0.51, and is the least of the three cases. All flow conditions and numerical parameters are summarized in Table 4.3.

The variation in normalized temperature for both LJPA and VHS models are observed in Figure 4.3 to be in excellent agreement with each other, and have the least variation across the gap relative to the previous two cases. Figure 4.3 shows a more significant difference in velocity profiles between the two models at the walls. The velocity slip for this case is the largest as a result of the larger mean free path, with the VHS model predicting a larger velocity slip than the LJPA model. A mostly linear velocity profile is also observed in Figure 4.3 for most of the domain due to the lower Mach number.

Figures 4.4 and 4.4 show the shear stress and viscosity variations across the gap, respectively, using the LJPA and VHS models. The shear stresses remain constant across the gap, with a mean value of $1.56 \times 10^{-2}\, Pa$ for LJPA and $1.74 \times 10^{-2}\, Pa$ for VHS models. The larger Knudsen layer observed for the VHS model in Figure 4.4 is due to the larger mean free path, and in turn causes larger shear stresses and viscosities. Agreement between the VHS model viscosities computed from DSMC and theory is better than that of the LJPA model. The average error in VHS model viscosity relative to theory is 1.09% while for the LJPA model the error is 3.45%. The Maitland and Smith [52] fit of viscosity measurements shown in Figure 4.4 indicate the LJPA model viscosities are in better agreement than the VHS; with errors of

2.06% and 9.51% for LJPA and VHS models, respectively. The reason for the larger deviation in viscosity computed from the LJPA model in DSMC relative to theory is as yet unclear.

Several additional cases have been analyzed in order to determine the source of this error including: varied number of simulated particles per cell, varied Knudsen number, varied minimum cut-off angle, and varied time step and cell size. The DSMC computed viscosities and viscosity errors relative to theory are presented in table 4.4 for each of these diagnostic cases. Most of the cases show little effect on the viscosity errors between DSMC and theory, but a sufficiently small time step and cell size appears to be an important factor. Decreasing the cell size to 1.43 μm, or 7% of the mean free path, and the time step to 0.90 ns resulted in a –6.64% error between DSMC and theoretical viscosity. This is about a percent lower in magnitude, and is therefore significant. Furthermore, decreasing both the cell size and time step to just 5% of the mean free path and mean collision time, respectively, reduced the viscosity error to –2.37%. Although the ratios of cell size to mean free path and time step to mean collision time were kept constant between 900 K and 1500 K cases, the no-time counter [1] (NTC) method requires these smaller cell sizes and time steps.

Table 4.4.. Errors in viscosities computed from L-J model in DSMC relative to theory at 1500 K and $\tau_{eq} = 8.49ns$, $\lambda = 20.1\mu m$

Case Description	$\Delta t(ns)$	$\Delta x(\mu m)$	μ_{DSMC} $(\mu Pa \cdot s)$	$\frac{\mu_{DSMC}-\mu_{theory}}{/\mu_{theory}}$ (%)	$\tau_{xy}(Pa)$
LJPA Baseline	2.80	2.50	66.767 ± 0.041	-7.63	12.227
LJPA 2,000 Particles	2.80	2.50	66.761 ± 0.041	-7.65	12.169
LJPA Low $\Delta x, \Delta t$	1.40	2.00	67.085 ± 0.035	-7.20	12.220
LJPA Lower $\Delta x, \Delta t$	0.90	1.43	67.490 ± 0.039	-6.64	12.219
LJPA Lowest $\Delta x, \Delta t$	0.425	1.00	70.951 ± 0.108	-2.37	12.210

Case 3 requires the most computational time of the three cases due to the higher number of collision events. One million sampling time-steps take 4,016 s for the LJPA model and nearly half that, 2,370 s, for the VHS model.

4.1.4 Couette Simulations in the Transitional Regime

The low-temperature, supersonic, Couette flow simulations of Section 4.1.3 are repeated here for Knudsen numbers ranging from slip to transitional regimes in order to study the importance of a realistic potential as Knudsen number increases. The wall temperatures are kept at a constant 40 K for each of the cases considered in this section; with the Knudsen number varied through the initial number density. A domain length of 1 m and 20 particles per cell are again used, and the time-step and cell width are set to be approximately 15% of the mean collision time and 15% of the mean free path, respectively. These case conditions are summarized in Table 4.5.

Table 4.5.. Summary of flow conditions and numerical parameters used for the Couette flow in the transitional regime

Quantities	Case A	Case B	Case C	Case D	Case E
Wall Temperature, T_{wall} (K)	40	40	40	40	40
Initial Number Density, n $(1/m^3)$	1.4×10^{20}	7.0×10^{19}	1.4×10^{19}	7.0×10^{18}	7.0×10^{17}
Moving Wall Velocity, v_{wall} (m/s)	300	300	300	300	300
Mach number, M	2.55	2.55	2.55	2.55	2.55
Knudsen number, Kn	0.0051	0.01	0.051	0.1	1
Wall Separation, L (m)	1	1	1	1	1
$\Delta t(\mu s)$	1	2.9	10	29	290
Number of Cells	1,500	650	1,500	65	10
Number of Particles	3×10^4	1.3×10^4	3×10^4	1.3×10^3	2×10^2

In the free-molecular limit, there are no collisions and hence the choice of inter-molecular potential is inconsequential. The differences in shear stress between the

LJ and VHS models are shown in Table 4.6 to be tending towards zero as Knudsen number is increased - in agreement with the previous statement.

Table 4.6.. Shear stresses and viscosities computed from LJ and VHS models in the slip and transitional regimes

Kn	$\tau_{xy,VHS}(Pa)$	$\tau_{xy,LJ}(Pa)$	$\frac{\tau_{xy,VHS}-\tau_{xy,LJ}}{/\tau_{xy,LJ}}$ (%)
0.0051	1.559×10^{-3}	1.221×10^{-3}	27.68
0.01	1.549×10^{-3}	1.212×10^{-3}	27.14
0.051	1.430×10^{-3}	1.115×10^{-3}	24.08
0.1	1.254×10^{-3}	1.049×10^{-3}	19.46
1	3.785×10^{-4}	3.549×10^{-4}	6.654

Another measure for quantifying the effect of the intermolecular potential on Couette flow is the difference in velocity distribution function relative to the equilibrium distribution function,

$$|f(u,v) - f^{eq}(u,v)| \ . \tag{4.13}$$

The original 3-D velocity distribution function has been integrated over the velocity in the z-direction, w, to produce the 2-D distribution function, $f(u,v)$. The shear stress is anyways in the xy-plane, and the w velocities are not affected. The equilibrium distribution function in Eq. (4.13) may be written as [1]

$$f^{eq}(u,v) = \left(\frac{m}{2\pi kT}\right) \exp\left(-\frac{m\left(u-u_0\right)^2}{2kT} - \frac{m\left(v-v_0\right)^2}{2kT}\right) . \tag{4.14}$$

A 1-D velocity distribution, $f(v)$, may similarly be obtained by further integration over the x-velocities, u. Doing so allows for the computation of statistical moments such as mean v-velocities and skewness of the distribution function; which also indicate the degree of non-equilibrium. The skewness,

$$\gamma = \mathrm{E}\left[\left(\frac{\mathrm{v}-\mathrm{v}_0}{\sigma}\right)^3\right] = \frac{\mathrm{E}\left[\mathrm{v}^3\right] - 3\mathrm{v}_0\sigma^2 - \mathrm{v}_0^3}{\sigma^3} \tag{4.15}$$

is a third-order moment where the expectations are integrations over the distribution function,

$$\mathrm{E}\left[\mathrm{v^n}\right] = \int_{-\infty}^{\infty} \mathrm{v^n\, f(v)\, dv}\,. \tag{4.16}$$

The distribution function was computed for both VHS and LJ models in Case A and Case C using more than 700 million samples in 150x500x150 ($u \times v \times w$) velocity bins at the spatial location: $X = 10^{-3}\, m$. Several observations can be made from Figure 4.5. First, both L-J and VHS models have similar deviations from equilibrium relative to the u-velocity at the lower Knudsen number of 0.0051. Also, the VHS model deviations from the equilibrium distribution function are shifted to higher v-velocities relative to the L-J model. This is an indication of higher skewness in the distribution function for v-velocities, and is confirmed when the skewness is computed from Eq. (4.15). The skewness in the $f(v)$ distribution function for the VHS model is 0.577 - nearly four times greater than that of the L-J model. The equilibrium distribution function has zero skewness, and therefore larger values of skewness indicate larger deviation from equilibrium. This result is in agreement with previous discussions about the relative sizes of the Knudsen layer - the VHS model is predicting a larger degree of nonequilibrium and therefore has a larger Knudsen layer. More can be deduced from the deviations in the 2-D velocity distribution functions as a Knudsen number of 0.051.

One obvious difference in the errors at the higher Knudsen number is the distortion in the contours for both L-J and VHS models. This indicates that under these conditions both U- and V-velocities are affected such that the distribution function is skewed in both directions. The skewness is larger for this case indicating a larger degree of nonequilibrium; with the skewness for the L-J and VHS models being 0.605 and 0.723, respectively. However, both models are similarly predicting high degrees of nonequilibrium, and the contours of distribution function errors in Figure 4.5 show close agreement between the two models.

The non-smooth transition near u-velocity of 0 m/s for the higher Knudsen number in Figure 4.5 is due to differences in the incident and reflected distribution functions

near the wall. These 2-D velocity distribution functions are sampled next to the stationary left wall, and the gas-surface interactions are assumed to be entirely diffusive such that the particles are reflected according to the Maxwellian distribution at the wall temperature. Therefore, incident particles have one distribution function shifted due to the moving wall, the reflected particles have another distribution function following Maxwellian, and insufficient collisions are occuring to equilibriate resulting in the bi-modal distribution observed.

A relationship between the degree of nonequilibrium and intermolecular potentials is now clear. The differences in degree of nonequilibrium between the L-J and VHS models is greatest at lower Knudsen numbers and thus results in the largest differences in shear stress and viscosity. As the Knudsen number is increased towards the free-molecular limit both models will indicate the same degree of nonequilibrium, and the choice of intermolecular potential on shear stress and viscosity will be negligible.

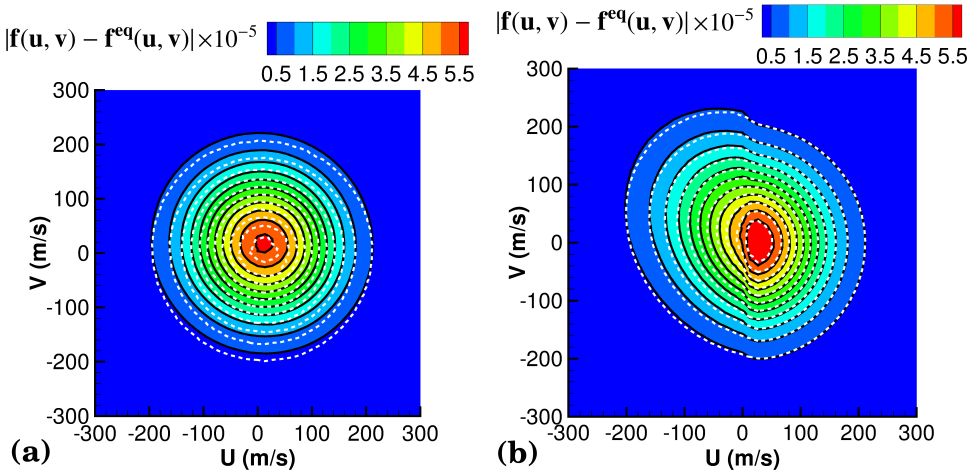

Figure 4.5.. Contours of 2-D velocity distribution errors relative to the equilibrium distribution function using VHS (solid lines) and L-J (dashed lines) models. (a) $Kn = 0.0051$, (b) $Kn = 0.051$

4.2 Recommended VSS and L-J Parameters

For many problems involving a relatively small temperature range the VSS model may reproduce experimentally observed viscosity and self-diffusion coefficients well, as the model parameters are determined based on such measurements. However, many gas flow problems involve a wide temperature ranges, such as those found in shock waves [54, 55], in-space propulsion systems [56], and vacuum technology [57, 58]. It is possible to divide a temperature range into a number of intervals and define a new set of model parameters for each interval, but it would be preferable to use a single set of parameters.

A number of sources are already available for obtaining L-J parameters [59–62], but to the knowledge of the authors are either not based on viscosity and self-diffusion measurements of interest here or are based on more dated measurements and methods. [30] Fewer sources yet are available for VSS model parameters [1, 9, 63]. While more accurate potentials exist for most of the gas species interactions considered, the focus of this paper is on simpler models which may be more readily applied to areas of study such as rarefied gas dynamics [64, 65] and molecular dynamics. [66, 67] Thus, a single set of parameters to use in the range 50 K to 2200 K is recommended for eight common gases based on a critical review of experimental measurements [52, 53, 68–72] and *ab-initio* calculations for shear viscosity, thermal conductivity, and self-diffusion coefficients. [73–76]

4.2.1 Numerical Procedure

Determining the optimal set of model parameters for each gas requires the theory described previously in this section, reference values of viscosity and self-diffusion coefficients obtained from experimental measurements or *ab-initio* calculations, and a numerical scheme such as the Nelder Mead Simplex method. [77, 78] The Nelder Mead Simplex method only requires the objective function to be defined, and initial guesses and tolerances to be specified. It is an efficient method, but it is also a

local optimization method. Therefore, on the order of 200 runs are performed with different initial guesses to span the parameter space. Two separate objective functions are used: (1) maximize the number of viscosity and self-diffusion calculations within a specified range from the measured values and (2) minimize the least square error between the calculated viscosity and self-diffusion and the measurements. In some cases, the estimated measurement uncertainty is much less than 1%, but for practical engineering purposes in rarefied gas dynamics or plasma physics 1% error would constitute acceptable agreement. Therefore, the first objective function maximizes the number of points which either lie within 1% of the measured values or within the measurement error - whichever is greater.

The calculations are based on Eqs. (2.16), (2.13), and (2.20) for the L-J model and Eqs. (2.34), (2.37), and (2.20) for the VSS model. The priority is to obtain model parameters which result in transport properties which lie within the experimental measurements, but several parameters may produce the same maximum number of points. Therefore, the optimized set model parameters which result in the least square error,

$$\varepsilon = \frac{1}{N}\sum_{i=1}^{N}\left(\frac{\mu_i - \mu_{i,exp}}{\mu_{i,exp}}\right)^2, \tag{4.17}$$

are selected as the recommended parameters. The summation in Eq. (4.17) is over the number of experimental data points, N, and the error is normalized by the measured value, $\mu_{i,exp}$.

Each gas used function tolerances of 10^{-6} and the objective function returns the number of data points which lie within the measurement uncertainty, normalized by the total number of data points. This indicates that the model parameters correspond to a maximum validity range. Initial guesses were varied relative to the values found in literature for L-J parameters: $\epsilon_0/k = [\max\left(\epsilon^{(Hirschfelder)} - 20, 5\right), 1.5\epsilon^{(Hirschfelder)}]$, $\sigma_0 = \sigma^{(Hirschfelder)} \pm 0.2$. The VSS parameter, ω, was varied between the two limits: 0.5 for hard sphere and 1.0 for a Maxwell molecule. The second VSS model parameter, α, may then be computed directly from Eq. (2.39). The last VSS parameter, $\mu_{\mathrm{ref}}(T_{\mathrm{ref}})$, is varied according to the temperatures at which both viscosity and self-diffusion are

measured. Thus, the optimal ω and α parameters are recorded for each reference temperature, and the objective functions are compared to determine the optimal parameters overall.

4.3 Results and Discussion

Recommendations for VSS and L-J model parameters based on a critical review of experimental measurements and *ab-initio* calculations of viscosity are made in this section. The performance of the optimized parameters are assessed relative to a critical review of experimental measurements and *ab-initio* calculations of thermal conductivity. The sources of all the viscosity, self-diffusion coefficient, and thermal conductivity reference values are detailed first and listed in tables 4.7 and 4.8, and then comparisons to the reference values of the lighter and heavier gases are made using several sets of VSS and L-J model parameters.

Table 4.7.: Sources of viscosity and self-diffusion coefficient measurements, correlations, and *ab-initio* calculations for 8 common gases. Underlined reference indicates source used for reference values.

Interaction	Viscosity References	Self-Diffusion References
H_2–H_2	Maitland and Smith 1972 [52] May *et al.* 2007 [79] Mehl *et al.* 2010 [80]	Bendt 1958 [71]
He–He	Cencek *et al.* 2012 [73] Kestin *et al.* 1972 [81] Kestin and Wakeham 1983 [82] Vogel 1984 [83] Hurly and Moldover 2000 [76]	Hurly and Moldover 2000 [76] Kestin *et al.* 1984 [53]

Continued on next page

Table 4.7 – *Continued from previous page*

Interaction	Viscosity References	Self-Diffusion References
Ne–Ne	Bich *et al.* 2008 [75] Kestin and Leidenfrost 1959 [84] Kestin and Nagashima 1964 [85] DiPippo *et al.* 1967 [86] Flynn *et al.* 1963 [87] Kestin *et al.* 1972 [81] Vogel 1984 [83] Evers *et al.* 2002 [88]	Kestin *et al.* 1984 [53]
N_2–N_2	Lemmon and Jacobsen 2004 [68] Seibt *et al.* 2006 [89] Hellmann 2013 [90]	Winn 1950 [70]
O_2–O_2	Lemmon and Jacobsen 2004 [68]	Winn 1950 [70]
Ar–Ar	Vogel *et al.* [74] Lemmon and Jacobsen 2004 [68] May *et al.* 2006 [91] Vogel 2010 [92] Zhang *et al.* [93]	Kestin *et al.* 1984 [53]
Kr–Kr	Bich *et al.* 1990 [69] Evers *et al.* 2002 [88]	Kestin *et al.* 1984 [53]
Xe–Xe	Bich *et al.* 1990 [69] May *et al.* 2007 [79]	Kestin *et al.* 1984 [53]

The reference values of viscosity for O_2 and N_2, are all taken from recent correlations provided by Lemmon and Jacobsen, [68] which are based on comparisons to a large set of experimental data. More recent N_2 viscosity measurements made by Seibt *et al.* in 2006 [89] agree to within 0.7% of Lemmon and Jacobsen's correlation. *Ab-initio* calculations by Hellmann [90] are in close agreement at temperatures above 100 K.

Reference viscosities of Ar gas are taken from *ab-initio* calculations by Vogel *et al.* [74]; which are within 0.1% of recent, accurate viscosity measurements by May

Table 4.8.. Sources of thermal conductivity measurements, correlations, and *ab-initio* calculations for 8 common gases. Underlined reference indicates source used for reference values.

Interaction	Thermal Conductivity References	Interaction	Thermal Conductivity References
H_2–H_2	Blais and Mann 1960 [72] Johnston and Grilly 1946 [94] Mehl *et al.* 2010 [80]	O_2–O_2	Lemmon and Jacobsen 2004 [68] Jain and Saxena 1977 [95]
He–He	Cencek *et al.* 2012 [73] Kestin *et al.* 1984 [53] Bich *et al.* [69] 1990 Wakeham *et al.* 1991 [96] Hurly and Moldover 2000 [76]	Ar–Ar	Vogel *et al.* [74] Lemmon and Jacobsen 2004 [68] Kestin *et al.* 1984 [53] Bich *et al.* 1990 [69]
Ne–Ne	Bich *et al.* 2008 [75] Kestin *et al.* 1980 [97] Kestin *et al.* 1984 [53] Millat *et al.* 1988 [98]	Kr–Kr	Bich *et al.* 1990 [69] Haarman [99] 1973 Kestin *et al.* 1984 [53]
N_2–N_2	Lemmon and Jacobsen 2004 [68] Stephan *et al.* 1987 [100] Duan *et al.* 1997 [101] Hellmann 2013 [90]	Xe–Xe	Bich *et al.* 1990 [69] Springer and Wingeier 1973 [102] Assael *et al.* 1981 [103] Kestin *et al.* 1984 [53]

et al., [91] Vogel, [92] and Zhang *et al.* [93] The Ar viscosity correlation of Lemmon and Jacobsen [68] is also observed to be within 1% of Vogel *et al.* [74] over the entire temperature range considered in this work.

Viscosity correlations made by Bich *et al.* [69] are used as reference values for Kr and Xe. Reported viscosities are in better agreement with recent measurements by May *et al.* [79] than the correlation by Maitland and Smith [52] for Xe. Agreement with Kr viscosity measurements made by Evers *et al.* [88] is better than 0.2%, especially near room temperature.

For H_2 gas, the viscosity correlation by Maitland and Smith [52] is within the experimental measurement errors of more recent measurements made by May *et al.* [79],

and are therefore used as reference values. Agreement with *ab-initio* calculations of H_2 viscosity by Mehl *et al.* [80] is also well within the estimated uncertainties of the Maitland and Smith [52] correlation near ambient temperature.

Reference values of He viscosity taken from *ab-initio* calculations by Cencek *et al.* [73] The reported viscosities deviate by no more than 0.06% of the previous *ab-initio* calculations of Hurly and Moldover, [76] and are in best agreement with measurements made by Vogel [83], Kestin *et al.* [81], and Kestin and Wakeham. [82]

Ab-initio calculations of Ne viscosity by Bich *et al.* [75] are in good agreement with the most accurate experimental data [81, 83–88] at ambient temperatures and are therefore used as reference values.

Reference values of self-diffusion are largely based on measurements by Kestin *et al.* [53] and Winn [70]. Diffusion coefficients for all of the noble gases, with the exception of He, are taken from Kestin *et al.* [53]. Reference values of self-diffusion coefficient for He are instead taken from more recent *ab-initio* calculations by Hurly and Moldover. [76] Self-diffusion measurements made by Winn [70] are used as reference values for O_2, and N_2 while measurements by Bendt [71] are used for H_2.

Many of the same sources for viscosity also provide experimental or *ab-initio* calculations of thermal conductivity. Reference values of He thermal conductivity are taken from *ab-initio* calculations by Cencek *et al.* [73]; which are within 0.15% of the previous *ab-initio* calculations of Hurly and Moldover. [76] and are within 0.6% of measurements made by Bich *et al.* [69] These results are also in good agreement with measurements made by Wakeham *et al.* [96] and Kestin *et al.* [53]

Ab-initio calculations of Ne thermal conductivity by Bich *et al.* [75] are in good agreement with the most accurate experimental data using the transient hot-wire technique [97,103] at ambient temperatures and are therefore used as reference values. The reference values of thermal conductivity for O_2 and N_2 are taken from recent correlations provided by Lemmon and Jacobsen [68]; which are based on comparisons to a large set of experimental data. Uncertainties for the dilute gas limit relative are typically within $\pm 2\%$ for N_2, but are $\pm 5\%$ O_2. Recent *ab-initio* calculations

by Hellmann [90] are in good agreement with thermal conductivity correlations by Lemmon and Jacobsen [68] below 500 K, but are 10% higher at 2000 K. This is a discrepancy between theoretical calculations and experimental measurements. The correlation of Lemmon and Jacobsen [68] is used with the knowledge that significantly larger uncertainties are present at higher temperatures.

Thermal conductivity correlations made by Bich *et al.* [69] are used as reference values for Kr and Xe. Bich *et al.* [69] values for Kr are in good agreement with a previous correlation made by Kestin *et al.* [53] up to 2200 K, and are within ±1% of measurements made by Haarman [99] near ambient temperatures. The correlation for Xe [69] is in good agreement with the most accurate experimental data using the transient hot-wire technique [103] and is within 1.5 % of both measurements by Springer and Wingeier [102] and a previous correlation by Kestin *et al.* [53].

H_2 data is the most unreliable, with few thermal conductivity measurements made after Blais and Mann [72] in 1960. Stated uncertainties in Blais and Mann measurements [72] are 4%, but may be around 10% near ambient temperatures based on previous measurements by Johnston and Grilly [94]. At higher temperatures, this uncertainty may be larger.

The model parameters are tabulated in tables 4.9 and 4.10 for eight common gases using both the VSS and L-J models. Reported temperature ranges indicate the ranges for which the model parameters have been optimized, and the least square error relative to the reference values are provided in the last column.

4.3.1 Lighter Gases Including: H_2, He, and Ne

Agreement between computed and measured viscosities is most improved for the VSS model applied to the lighter gases. This is due to the shallow well depth of the lighter gases; leading to accurate representation of viscosity and self-diffusion coefficient dependency on temperature with a purely repulsive potential. Figures 4.6- 4.8

show the errors in viscosity and self-diffusion coefficient calculations relative to experimental measurements for the H_2–H_2, He–He, and Ne–Ne interactions, respectively.

Agreement with the H_2 viscosity correlation of Maitland and Smith [52] may be observed from Fig. 4.6. The VSS model using the recommended parameters in table 4.9 is in excellent agreement, except at temperatures below 100 K where the use of classical mechanics to describe the collisions is invalid. Use of the recommended L-J parameters in table 4.10 results in better agreement near ambient temperature. Viscosities calculated using the recommended L-J parameters are within the measurement error of ± 1.5% between 150 K and 1000 K, but the deviations increase with increasing temperature. Again, due to the increased importance of quantum effects at lower temperatures, the agreement with self-diffusion measurements of Bendt [71] is worst below 100 K.

The viscosities for the He–He interaction are again much better modeled using the recommended parameters for the VSS model rather than those from literature [1]. The estimated measurement uncertainty is only ± 0.01%, but neither model is capable of such close agreement over the temperature range considered. However, the VSS model with the recommended parameters in table 4.9 deviates by no more than 1% between 300 K and 2000 K. The least square error, as defined in Eq. (4.17) and reported in the last column of tables 4.9 and 4.10, is reduced by a factor of four with use of the recommended L-J parameters. Fewer experiments are available for self-diffusion coefficient, and the deviation between them is rather large. The deviation between Hurly and Moldover [76] and experiments [71, 104, 105] is between -7% and 6%. Only the VSS and L-J models with the parameters recommended in this work are within this measurement uncertainty at higher temperatures.

Both L-J and VSS model parameters from literature [1, 30, 106] are mostly outside of the estimated uncertainty of the viscosity calculations for Ne gas, but the agreement is significantly improved through the use of the recommended parameters in table 4.10. The viscosity error for the VSS model is nearly -2% from 400 K and higher when using the model parameters from literature [1]. With the recommended

model parameters, the least square error is reduced by more than a factor of five, and excellent agreement may be observed in Fig. 4.8 Large errors at the lower temperatures are observable for the L-J model when using the recommended parameters in table 4.10 because the parameters are chosen to increase the range of validity relative to viscosity and self-diffusion measurements. More accurate *ab-initio* potentials for Ne have potential well depths on the order of 42 K, such as reported by Bich *et al.* [75] Thus, the recommended value of 72.614 K exaggerates the dominating attractive forces at lower temperatures. The resulting exaggeration in attractive forces causes the collision cross-section to be larger and conversely the viscosity to be smaller. Between 300 K and 1300 K, the L-J model using the recommended parameters in table 4.10 deviates by no more than 1% from the *ab-initio* calculations of Bich *et al.* [75]

Figure 4.8 shows that the L-J model, even with the recommended parameters, is not within the self-diffusion coefficient measurement uncertainty. The VSS model, on the other hand, is in good agreement above 200 K.

Thermal conductivities of H_2 and He are shown in Figure 4.14. It is clear that theoretical values follow a different trend from the measurements of Blais and Mann [72] for H_2 gas. All models are within the relatively large measurement error until 600 K where they continue to diverge from the measured values. Unfortunately, few measurements exist for H_2 gas to confirm this behavior. However, Saxena, Saksena, and Gambhir [107] have also reported similar disagreements and attributed it to errors in the thermal conductivity data.

Agreement between theoretical and measured thermal conductivity for He gas is similar to that of viscosity. Figure 4.14 shows that the VSS model is in best agreement with *ab-initio* calculations of Cencek *et al.* [73] over most of the temperature range considered.

Errors in the calculations of thermal conductivity of a Ne gas using VSS and L-J models relative to *ab-initio* calculations are shown in Figure 4.15. The use of the recommended parameters listed in table 4.9 improves the VSS model agreement with

Bich *et al.* [75] to be within 1% above 300 K. The L-J model follows a similar trend for thermal conductivity as for viscosity and deviates by more than 5% at temperatures below 250 K and above 1450 K.

4.3.2 Heavier Gases Including: N_2, O_2, Ar, Kr, and Xe

Attractive forces are more important over a wider temperature range for heavier gases owing to their deeper potential well, and therefore agreement between L-J model predictions and reference values of viscosity, self-diffusion coefficient, and thermal conductivity is better. Errors in viscosity and self-diffusion coefficient measurements relative to experimental measurements are illustrated in Fig. 4.9- 4.13 for the N_2–N_2, O_2–O_2, Ar–Ar, Kr–Kr, Xe–Xe, interactions, respectively.

The VSS model using recommended parameter values in table 4.9 greatly improves agreement with the viscosity correlation by Lemmon and Jacobsen [68] at higher temperatures. Both the L-J and VSS models with the recommended model parameters in tables 4.10 and 4.9, respectively, remain within the estimated measurement uncertainty above 300 K. Using the recommended parameters for the VSS model also improves its agreement with self-diffusion coefficient measurements, as shown in Fig. 4.9. The recommended parameters in table 4.10 for the L-J model result in self-diffusion coefficients which deviate slightly more from measurements than those corresponding to either of the two sets of parameters in literature. [30, 106]

Agreement with viscosity and self-diffusion coefficient measurements of the O_2–O_2 interaction is noticeably better with the recommended parameters for both VSS and L-J models. The VSS model, even with the recommended parameters in table 4.9, deviates more rapidly at higher temperatures than the L-J model, but remains within the estimated measurement uncertainty of Lemmon and Jacobsen. [68]

Also shown in Figure 4.9 are the self-diffusion calculations for the VSS model using parameters from Stephani *et al.* [63] The parameter values from Stephani *et al.* [63] result in viscosities and thermal conductivities which are in error by more than a factor

of two, and are therefore not shown in the plots for O_2 and N_2. This error is due to the significantly higher reference temperature of 2880 K on which the parameters are based. Both VSS and L-J models using the recommended values in tables 4.9 and 4.10, respectively, agree well with the self-diffusion coefficient measurements of Winn. [70]

For the Ar–Ar interaction, the ranges of validity for the L-J model are only slightly increased relative to the values provided by Hirschfelder *et al.* [30], improving agreement at ambient temperatures. Figure 4.11 shows that the viscosities computed using the L-J model and parameters from Mourits and Rummens [106] are in the worst agreement with viscosity measurements over most of the considered temperature range. Agreement between the VSS model using the recommended parameters in table 4.9 and *ab-initio* calculations of Vogel *et al.* [74] are generally better than 1%, except at temperatures below 400 K where the VSS model begins to deviate significantly.

In regards to the self-diffusion coefficient for Ar gas, the VSS model is somewhat improved at higher temperatures using the recommended parameters. The L-J model is observed in Fig. 4.11 to be in reasonable agreement with measurements over a wider temperature range using the recommended parameters, and is within 2% of measurements between 250 K and 1000 K.

The recommended L-J parameters in table 4.10 for the Kr–Kr interaction are close to the values reported by Hirschfelder *et al.* [30], and therefore only slight differences may be observed in viscosity and self-diffusion coefficient calculations shown in Fig. 4.12. Deviations of the L-J model with the recommended parameters from viscosity measurements by Bich *et al.* [69] are within the estimated measurement uncertainty over the entire temperature range considered. The VSS model using the recommended parameters in table 4.9 has a larger least square error than that of the VSS model with parameters from Bird [1], and this is due to the more rapid deviations from viscosity measurements at temperatures below 500 K. At ambient temperatures, the VSS model using the recommended parameters are in error by more than 5%.

Both the recommended L-J parameters in table 4.10 and parameters by Hirschfelder *et al.* [30] result in good agreement with self-diffusion coefficient measurements of Kestin *et al.* [82] The trends observed in Fig. 4.12 for the VSS models are similar to that of the viscosity calculations. Self-diffusion coefficient calculations using the recommended VSS parameters in table 4.9 are in best agreement near the reference temperature of 473.15 K, and deviate rapidly as the temperature decreases.

The agreement with viscosity measurements of Xe is markedly better for the L-J model than the VSS model at lower temperatures. The VSS model using the recommended parameters in table 4.9 compares the best at temperatures above 600 K, where the deviations from viscosity measurements of Bich *et al.* [69] are within the measurement error of $\pm$ 1%. The L-J model using the recommended parameters in table 4.10 is within 2% of the viscosity measurements of Bich *et al.* [69] above 300 K, and is within the measurement error between 350 K and 1500 K. The least square error is drastically reduced between the viscosity calculations and the experimental measurements when the recommended L-J parameters in table 4.10 are used.

Agreement with self-diffusion coefficient measurements is improved in the region near the reference temperature of 723.15 K when the recommended VSS model parameters in table 4.9 are used. However, the VSS viscosity using the recommended parameters is observed in Fig. 4.13 to significantly deviate from the self-diffusion coefficient measurements of Kestin *et al.* [82] as the temperature decreases. Values of self-diffusion coefficients using the recommended L-J parameters are generally within 2% of the measured values, except for temperatures below 300 K. Agreement between both sets of L-J model parameters from literature [30, 106] and self-diffusion coefficient measurements is best at ambient temperatures and deviates increasingly as temperature increases.

Figure 4.15 shows the errors in thermal conductivities computed from VSS and L-J models relative to the experimental fit of Lemmon and Jacobsen. [68] The VSS model is observed to diverge more slowly with the recommended parameters and is within the measurement error beyond 1100 K. Thermal conductivity calculations

using the L-J parameters from Hirschfelder *et al.* [30] are in the best agreement with measured values at higher temperatures. All models agree reasonably well near room temperature. Caution should be placed on these comparisons above 500 K, however, since recent *ab-initio* calculations of Hellmann [90] show that the correlation of Lemmon and Jacobsen [68] deviates increasingly as the temperature increases. At 2000 K, the calculations of Hellmann [90] are approximately 10% higher than the measurement-based correlations of Lemmon and Jacobsen. [68]

All models are within the ± 5% thermal conductivity measurement error for O_2 over most of the temperature range considered. More noticeable difference is present in Figure 4.16 between the VSS models using parameters from literature and from the recommendations in this work.

The L-J model is observed in Figure 4.16 to be in excellent agreement with thermal conductivity measurements of Ar over the majority of the temperature range considered. Only the L-J model using parameters from Mourits and Rummens [106] and the VSS model using parameters from Bird [1] are outside of the measurement error above 1300 K.

Figure 4.17 shows thermal conductivity calculation errors for the Kr–Kr and Xe–Xe interactions. Both the L-J models using the recommended parameters in table 4.10 and those from Hirschfelder *et al.* [30] are in good agreement with thermal conductivity measurements by Bich *et al.* [69] Above 1300 K, both L-J models then continue to deviate from the reference values of Bich *et al.* [69] and lie outside of the estimated measurement uncertainty. The agreement between the VSS model with the recommended parameters in table 4.9 and the thermal conductivity measurements is within the estimated measurement uncertainty for all temperatures above 400 K.

The L-J model using the recommended parameters in table 4.10 is in best agreement with thermal conductivity measurements of Xe gas overall. The error is slightly more than 3% at room temperature for the present L-J but is within the measurement error between 400 K and 1600 K. Agreement between the present VSS model and experimental measurements is best near room temperature; with errors rapidly

increasing at temperatures both below 100 K and above 700 K. At 1600 K, errors in the theoretical calculations of the present VSS model are as much as 16%.

Table 4.10.: L-J Model Parameters for 8 Common Gases in Temperature Range 20-2200 K

Interaction	T Range (K)	Reference	$\epsilon/k(K)$	$\sigma(\mathring{A})$	ε (%)
H_2–H_2	—	[30]	33.3	2.968	0.23
	20–1000	Present	58.66	2.8415	0.34
He–He	—	[30]	10.22	2.576	0.60
	140–1000	Present	4.8083	2.6536	0.15
Ne–Ne	—	[30]	35.7	2.789	0.08
	—	[106]	32.0	2.822	0.11
	80–2200	Present	72.614	2.6484	0.05
N_2–N_2	—	[30]	91.5	3.681	0.02
	—	[106]	82	3.738	0.02
	50–2200	Present	88.5859	3.7273	0.02
O_2–O_2	—	[30]	113.0	3.433	0.03
	—	[106]	102.6	3.480	0.02
	50–2000	Present	116.612	3.450	8.8×10^{-3}
Ar–Ar	—	[30]	124.0	3.418	0.02
	—	[106]	113.5	3.465	0.06
	90–2200	Present	152.56	3.351	0.02
Kr–Kr	—	[30]	190	3.610	0.02
	—	[106]	178.0	3.662	0.06
	140–2000	Present	187.83	3.612	0.02

Continued on next page

Table 4.10 – *Continued from previous page*

Interaction	T Range (K)	Reference	$\epsilon/k(K)$	$\sigma(\mathring{A})$	ε (%)
Xe–Xe	—	[30]	229.0	4.055	0.09
	—	[106]	230.2	4.050	0.08
	180–1500	Present	273.99	3.932	0.01

Table 4.9.. VSS Model Parameters for 8 Common Gases in Temperature Range 20-2200 K

Interaction	T Range (K)	Reference	$d_{\text{ref}}(\mathring{A})$	ω	α	$T_{\text{ref}}(K)$	$\mu_{\text{ref}}(Pa \cdot s) \times 10^{-6}$	$\left(\frac{\rho D_{11}}{\mu}\right)_{\text{ref}}$	ε (%)
H_2–H_2	Near 273	[1]	2.88	0.67	1.35	273	8.45	1.37	0.11
	20–2200	Present	2.9016	0.689	1.370	296	8.86	1.37	0.05
He–He	Near 273	[1]	2.30	0.66	1.26	273	18.65	1.32	0.38
	140–2000	Present	2.2980	0.712	1.429	350	22.13	1.39	6.6×10^{-3}
Ne–Ne	Near 273	[1]	2.72	0.66	1.31	273	29.75	1.35	0.04
	80–2200	Present	2.4840	0.675	1.331	823.15	64.96	1.35	6.9×10^{-3}
N_2–N_2	Near 273	[1]	4.11	0.74	1.36	273	16.56	1.34	0.59
	1000–5000	[63]	3.25	0.68	1.4	2880	172.91	1.39	118
	50–2200	Present	3.8705	0.686	1.365	353.15	20.24	1.37	0.46
O_2–O_2	Near 273	[1]	4.01	0.77	1.4	273	19.19	1.35	0.59
	1000–5000	[63]	2.90	0.70	1.8	2880	239.7	1.59	118
	50–2200	Present	3.8631	0.7154	1.2929	298.15	20.53	1.31	0.42
Ar–Ar	Near 273	[1]	4.11	0.81	1.40	273	21.17	1.33	1.67
	90–2200	Present	3.5645	0.697	1.311	523.15	35.07	1.33	0.38
Kr–Kr	Near 273	[1]	4.70	0.80	1.32	273	23.28	1.29	0.14
	140–2000	Present	4.0957	0.7344	1.312	473.15	37.87	1.31	0.22
Xe–Xe	Near 273	[1]	5.65	0.85	1.44	273	21.07	1.33	0.16
	180–2000	Present	4.4165	0.7407	1.336	723.15	50.67	1.33	0.36

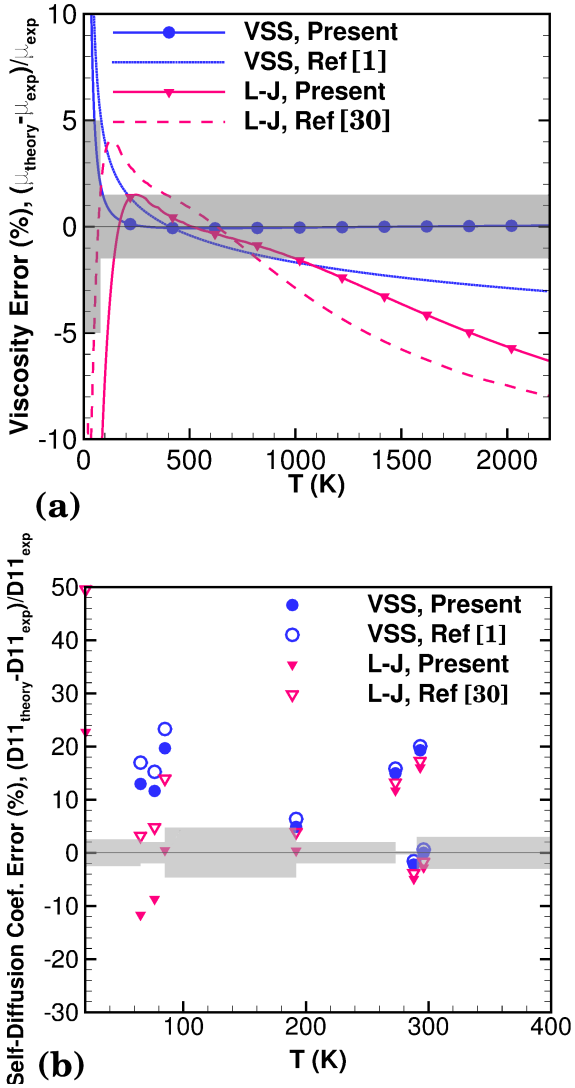

Figure 4.6.. VSS and L-J model (a) viscosity errors for H_2 gas relative to experimental fit of Maitland and Smith [52] and (b) self-diffusion errors for H_2 gas relative to experimental measurements of Bendt [71]. Shaded region indicates the estimated uncertainty of the experimental measurements.

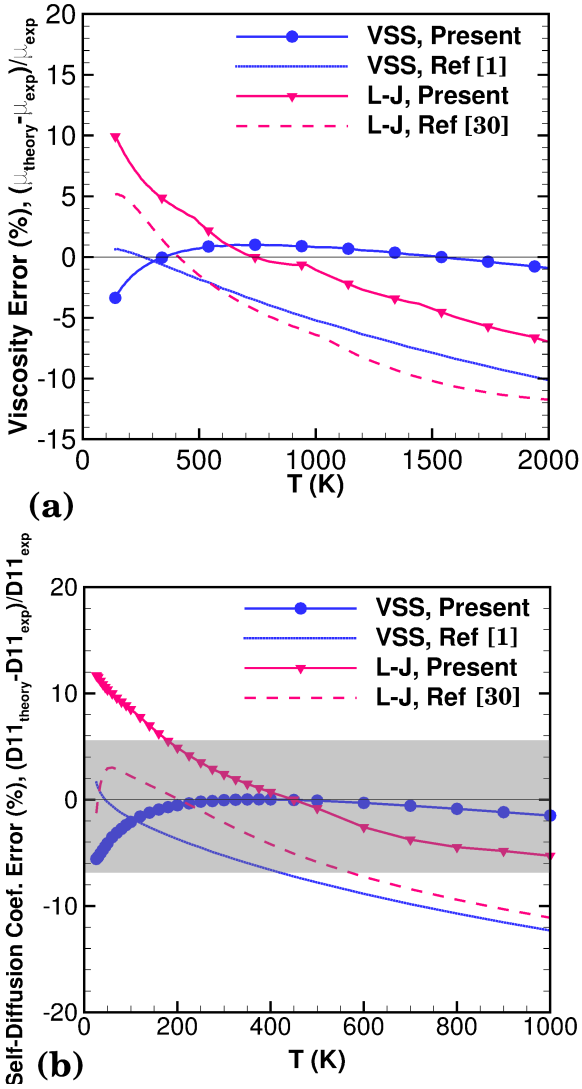

Figure 4.7.. VSS and L-J model (a) viscosity errors for He gas relative to *ab-initio* calculations of Cencek *et al.* [73] and (b) self-diffusion errors for He gas relative to *ab-initio* calculations of Cencek *et al.* [73] Shaded region indicates the estimated uncertainty of the *ab-initio* calculations.

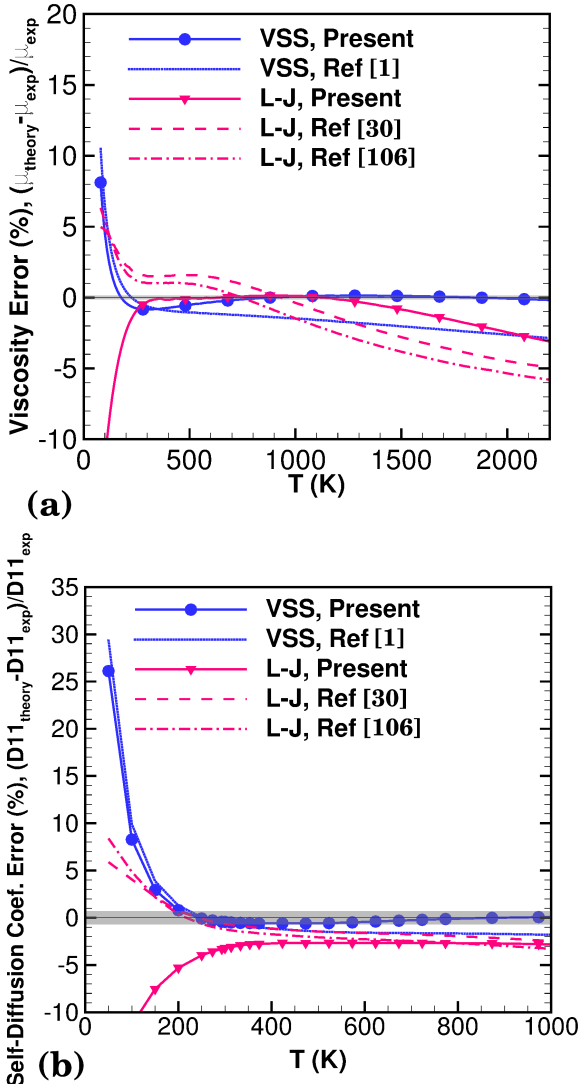

Figure 4.8.. VSS and L-J model (a) viscosity errors for Ne gas relative to *ab-initio* calculations of Bich *et al.* [75] and (b) self-diffusion errors for Ne gas relative to experimental measurements of Kestin *et al.* [53] Shaded region indicates the estimated uncertainty of the *ab-initio* calculations and experimental measurements.

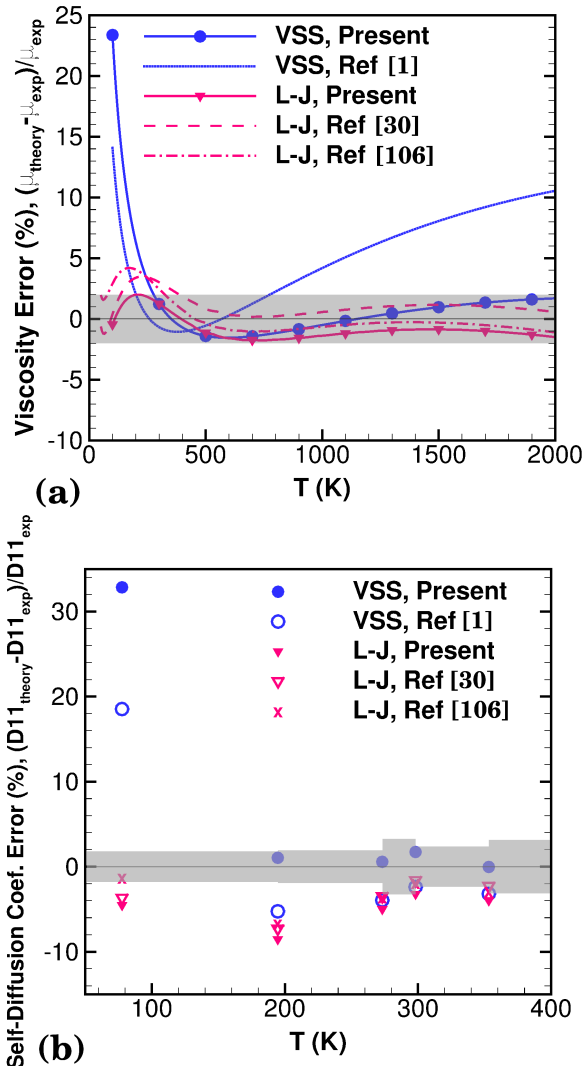

Figure 4.9.. VSS and L-J model (a) viscosity errors for N_2 gas relative to experimental fit of Lemmon and Jacobsen [68] and (b) self-diffusion errors for N_2 gas relative to experimental measurements of Winn. [70] Shaded region indicates the estimated uncertainty of the experimental measurements.

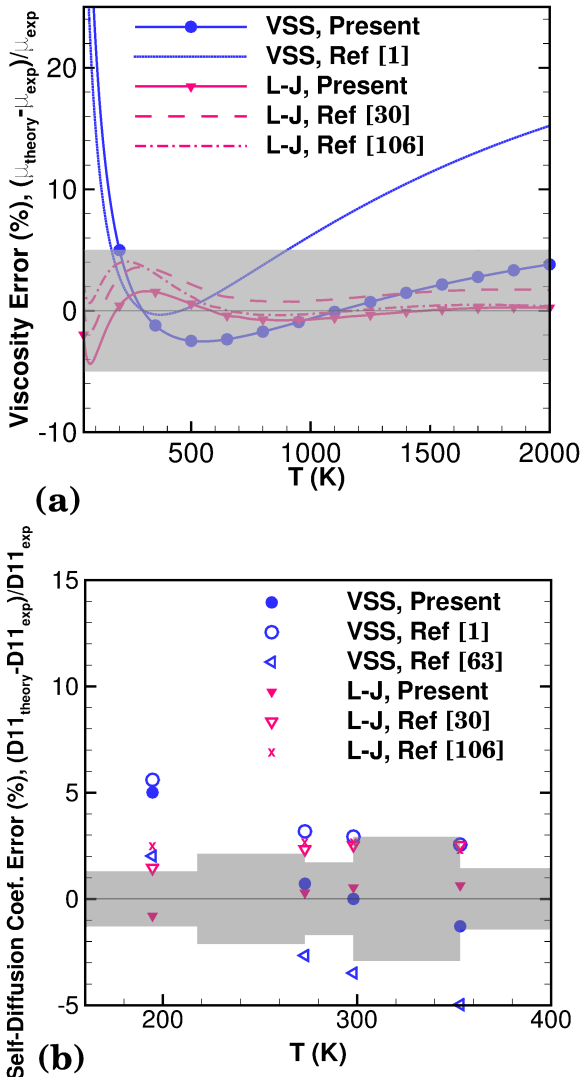

Figure 4.10.. VSS and L-J model (a) viscosity errors for O_2 gas relative to experimental fit of Lemmon and Jacobsen [68] and (b) self-diffusion errors for O_2 gas relative to experimental measurements of Winn. [70] Shaded region indicates the estimated uncertainty of the experimental measurements.

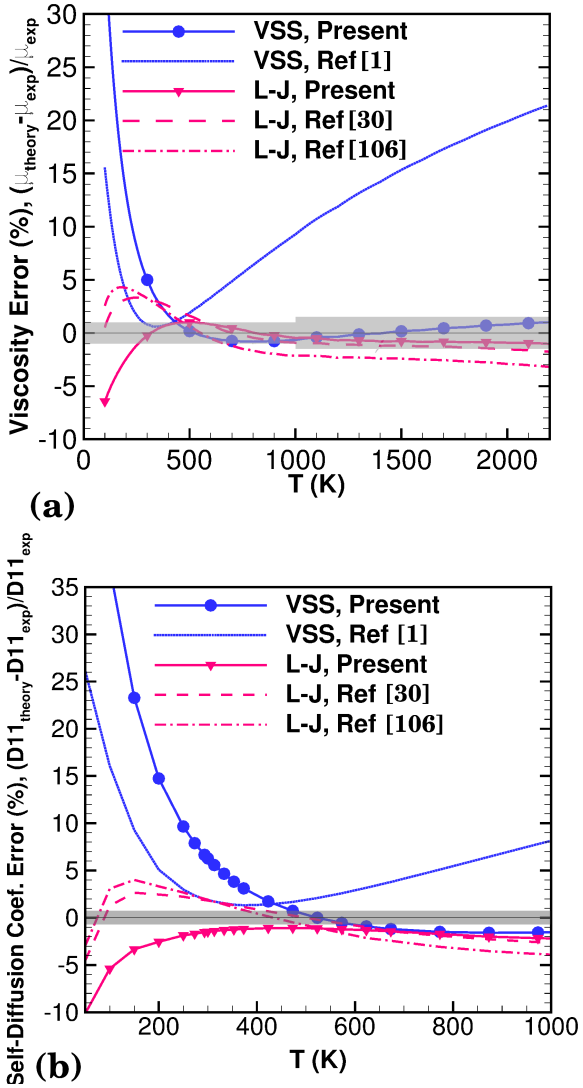

Figure 4.11.. VSS and L-J model (a) viscosity errors for Ar gas relative to *ab-initio* calculations of Vogel *et al.* [74] and (b) self-diffusion errors for Ar gas relative to experimental measurements of Kestin *et al.* [53] Shaded region indicates the estimated uncertainty of the *ab-initio* calculations and experimental measurements.

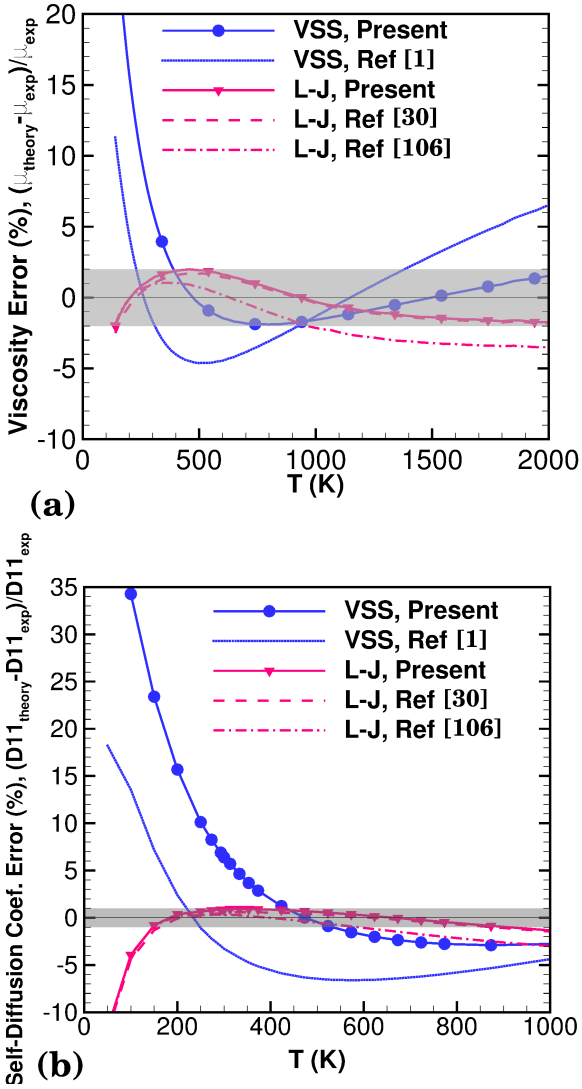

Figure 4.12.. VSS and L-J model (a) viscosity errors for Kr gas relative to experimental fit of Bich *et al.* [69] and (b) self-diffusion errors for Kr gas relative to experimental measurements of Kestin *et al.* [53] Shaded region indicates the estimated uncertainty of the experimental measurements.

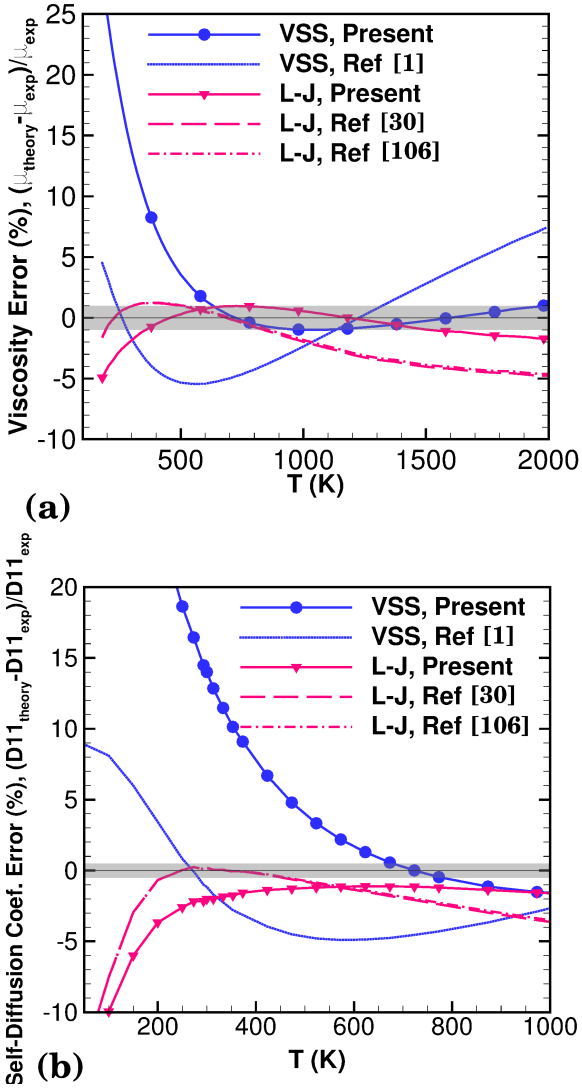

Figure 4.13.. VSS and L-J model (a) viscosity errors for Xe gas relative to experimental fit of Bich *et al.* [69] and (b) self-diffusion errors for Xe gas relative to experimental measurements of Kestin *et al.* [53] Shaded region indicates the estimated uncertainty of the experimental measurements.

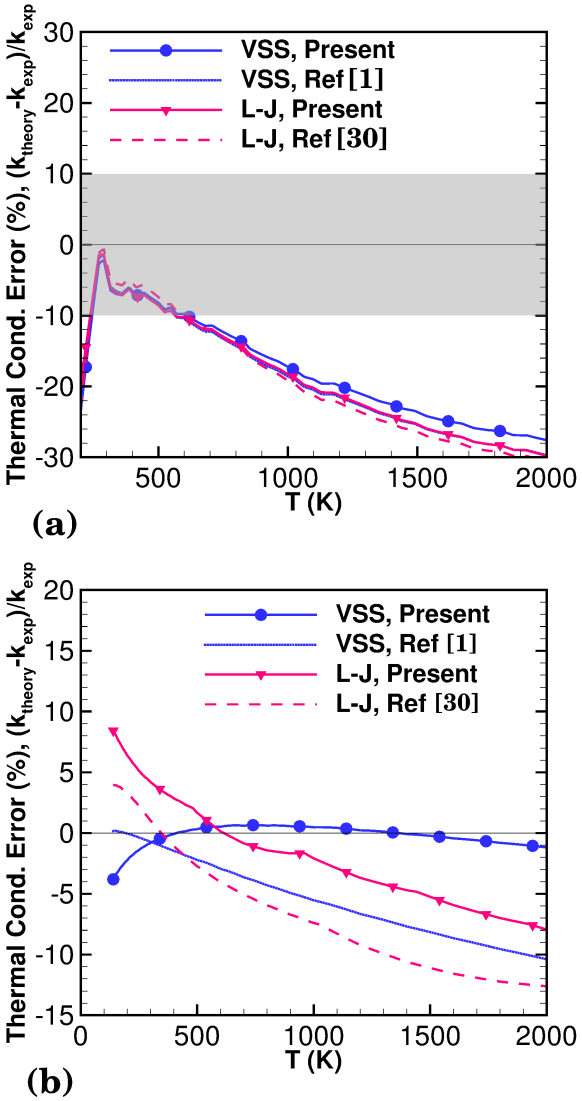

Figure 4.14.. VSS and L-J model thermal conductivity errors for (a) H_2 gas relative to experimental measurements of Blais and Mann [72] and (b) He gas relative to *ab-initio* calculations of Cencek *et al.* [73] Shaded region indicates the estimated uncertainty of the experimental measurements and *ab-initio* calculations.

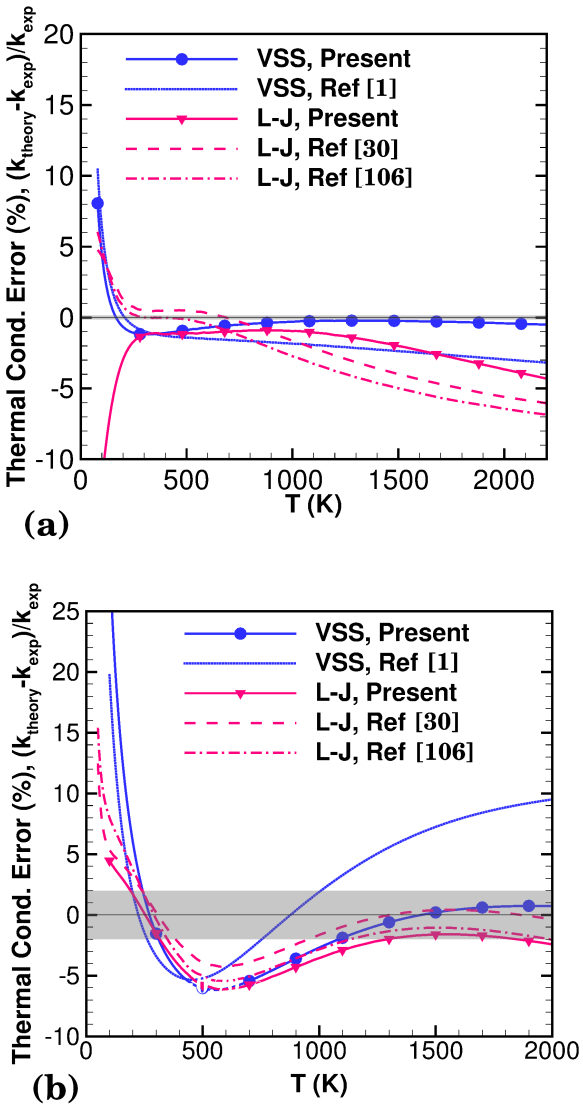

Figure 4.15.. VSS and L-J model thermal conductivity errors for (a) Ne gas relative to *ab-initio* calculations of Bich *et al.* [75] and (b) N_2 gas relative to experimental fit of Lemmon and Jacobsen. [68] Shaded region indicates the estimated uncertainty of the *ab-initio* calculations and experimental measurements.

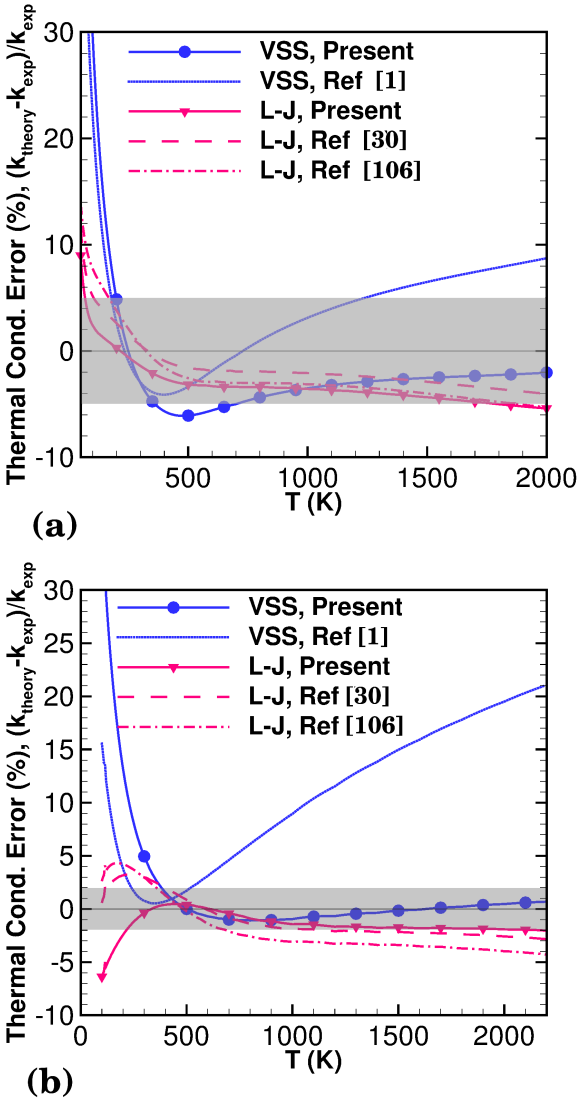

Figure 4.16.. VSS and L-J model (a) thermal conductivity errors for O_2 gas relative to experimental fit of Lemmon and Jacobsen [68] and (b) Ar gas relative to *ab-initio* calculations of Vogel *et al.* [74] Shaded region indicates the estimated uncertainty of the experimental measurements and *ab-initio* calculations.

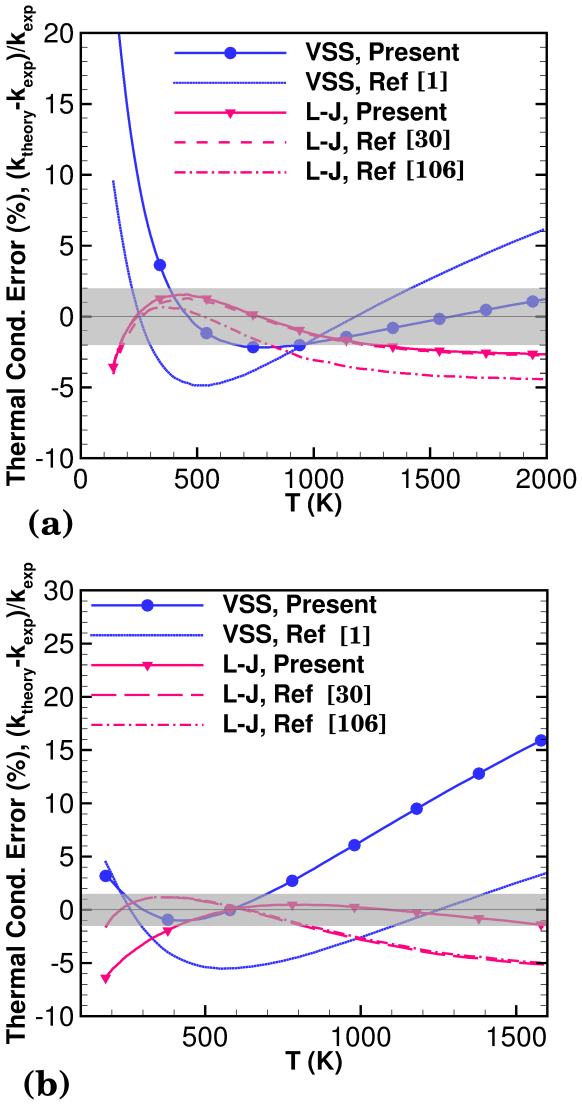

Figure 4.17.. VSS and L-J model (a) thermal conductivity errors for Kr gas relative to experimental fit of Bich *et al.* [69] and (b) Xe gas relative to experimental fit of Bich *et al.* [69] Shaded region indicates the estimated uncertainty of the experimental measurements.

4.4 Binary Scattering for Ground State Atomic Oxygen Collisions

Significant effort has been placed on accurately computing transport collision integrals [108–112]; with more recent focus on *ab-initio* potentials [20,21,24,25]. Accurate

transport collision integrals are useful in a variety of research areas including hypersonics [111, 113] astrophysics [114, 115], and thermal plasmas [116] and have thus benefited. One area which has yet to make significant use of any realistic potential beyond the L-J (12-6) potential is rarefied gas dynamics.

Of particular importance in gas dynamics is matching observed transport properties, and this is the key to the success of phenomenological models such as the variable hard sphere [1] (VHS) and variable soft sphere [9] (VSS) models. These are both simple models, possessing only repulsive forces as with the hard sphere (HS) model, but modified to better match viscosity and self-diffusion measurements. Such models have been shown to work well over a wide temperature range for lighter gases possessing a shallow potential well, but less so for gases with a deeper potential well [117].

Transport properties are macroscopic properties which are naturally obtained from the microscopic interactions specified by the potential. Rather than defining a model which matches observed macroscopic properties the idea here is to use a model based on first principles. In the case where experimental measurements are limited, what do you do to obtain model parameters for such phenomenological models? One could use the models based on *ab-initio* potentials to compute the required transport properties and thereby determine the optimal parameters. However, for some gases, such as those with significant attractive forces, this may be insufficient over a wide temperature range [117].

Atomic oxygen is one such gas which possesses a deep potential well and is a prevalent species formed during reentry of hypersonic vehicles. It is also one of the main constituents of the upper atmosphere known as the Thermosphere. [118] In the Thermosphere, which encompasses altitudes between approximately 85 and 500 km, the temperatures range from 170 to more than 1,000 K. [118] At these altitudes, the densities are six orders of magnitude lower than at sea level and therefore modeling the transport under these conditions requires kinetic theory based methods such as DSMC [1].

Previous studies [112, 119] have reviewed collision integrals using various potentials, but were focused on implementation into continuum fluid dynamics. That is, only the viscosity and mass-diffusion type collision integrals were investigated. A recent publication by Bruno, Frezzotti, and Ghiroldi [120] demonstrated the accuracy of a coupled DSMC-classical trajectory (DSMC-CT) method using an accurate potential energy surface for molecular oxygen interactions. Their focus was also on the computation of transport properties. However, the DSMC method [1] is a particle-based method which requires more fundamental properties such as scattering angles and total collision cross-sections.

The ground state O-O interaction is investigated in regards to scattering angles, total cross-sections, and collision integrals using: (1) VSS model, (2) L-J model, (3) Morse potential based on spectroscopic constants [121], (4) Morse potential based on *ab-initio* potentials [109], and (5) *ab-initio* potential of Varandas and Pais [20]. Optimal VSS parameters are determined based on viscosity calculations using Varandas and Pais potential and compared in terms of computational cost and accuracy of transport properties.

The only potential considered in this section which has not already been discussed in Chapter 2 is the potential by Varandas and Pais [20]. Therefore, a few comments will be made here.

Varandas and Pais [20] had generated a potential energy surface for ground state ozone, O_3, using a combination of *ab-initio* calculations and experimental data from spectroscopic, incomplete total scattering cross-section, and kinetic thermal rate measurements. The three-body potential may be represented as a summation of an extended-Hartree-Fock type (EHF) energy and the dynamical correlation energy,

$$\phi(\mathbf{r}) = \phi_{EHF}(\mathbf{r}) + \phi_{corr}(\mathbf{r})\,. \tag{4.18}$$

The potential for the EHF energies contains the exponential repulsive terms while the potential for the dynamical correlation energy contains the dispersion terms. Intermolecular separation distances must be specified between each of the three oxygen

atoms, and therefore a bold-face notation is used for the array of separation distances, **r**. Since the analysis in this work is only focused on the two-body interaction, the remaining oxygen atom is specified a large distance away (∼1000 Å) such that the potential reduces to a two-body potential. For details on the potential and corresponding parameter values, the reader is referred to the article by Varandas and Pais. [20] The behavior of the potential of Varandas and Pais [20] is shown in Fig. 4.18 relative to VSS, L-J, and Morse potentials for ground-state O-O.

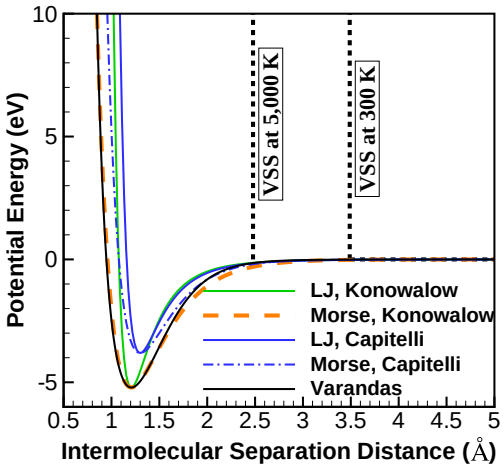

Figure 4.18.. Comparison of VSS, L-J, Morse, and Varandas potentials for ground state O-O

4.4.1 Verification of Collision Integral Calculations

Verification of the program used to compute the transport collision integrals has been performed by comparing to accepted values for Morse potentials tabulated in literature [122,123]. Smith and Munn [122] had calculated the diffusion and viscosity type collision integrals for the Morse potential using several values of the parameter, C. This parameter is related to the scaling parameter, α, defined in Section 2.7 as

$\alpha = C/\sigma$. The values obtained using the present program described in Section 2.8 are compared to those of Smith and Munn [122] in table 4.11.

Table 4.11.. Verification of collision integral calculations for Morse potential

	$\Omega^{*(1,1)}$			$\Omega^{*(2,2)}$		
T^*	Present	Smith and Munn [122]	Error (%)	Present	Smith and Munn [122]	Error (%)
$C = 2.0$						
0.004	21.3039	21.3303	-0.12	21.6525	21.6425	0.05
0.010	18.5246	18.5383	-0.07	17.7215	17.7060	0.09
0.020	16.3234	16.3252	-0.01	15.0360	14.9869	0.33
0.040	13.9444	13.9429	0.01	12.5565	12.5350	0.17
0.100	10.6493	10.6486	0.01	9.7042	9.7379	-0.35
0.200	7.6446	7.6296	0.20	7.8079	7.8154	-0.10
0.400	4.4328	4.4535	-0.46	5.0462	5.0400	0.12
1.000	1.8106	1.8140	-0.19	2.1444	2.1403	0.19
2.000	0.9764	0.9790	-0.27	1.1815	1.1794	0.18
4.000	0.5837	0.5830	0.12	0.7366	0.7362	0.05
$C = 4.0$						
0.004	7.0149	7.0039	0.16	7.9047	7.9153	-0.13
0.010	6.0869	6.0782	0.14	6.7212	6.7197	0.02
0.020	5.4461	5.4385	0.14	5.8887	5.8879	0.01
0.040	4.8395	4.8363	0.07	5.1130	5.1122	0.02
0.100	4.0428	4.0509	-0.20	4.1731	4.1757	-0.06
0.200	3.3738	3.3969	-0.68	3.5418	3.5466	-0.14
0.400	2.5277	2.543	-0.60	2.8178	2.8232	-0.19
1.000	1.4814	1.4859	-0.30	1.6866	1.6903	-0.22
2.000	1.0315	1.0321	-0.06	1.1712	1.1708	0.04
4.000	0.7883	0.7889	-0.07	0.9092	0.9084	0.09

There is good agreement between the two sets of collision integrals, with a maximum deviation of -0.68% occurring at a reduced temperature of 0.2. Otherwise, the deviations are typically better than 0.2%.

4.4.2 Scattering Angles and Total Collision Cross-Sections

Scattering angles and total collision cross-sections, σ_T, are computed for the: VSS model based on Varandas and Pais potential [20], (12-6) L-J potential, Morse (K-H) potential [121], Morse (C-F) potential [109], and the potential by Varandas and Pais [20]. All model parameters, with the exception of the potential by Varandas and Pais, are listed in table 4.12.

Table 4.12.. Intermolecular potential model parameters

Potential	Parameters				
VSS	ω	α	$T_{ref}(K)$	$d_{ref}(\mathring{A})$	$\mu_{ref}(\mu Pa \cdot s)$
	0.7376	1.29	300	3.4886	18.2307
L-J	$\sigma(\mathring{A})$	$\epsilon(eV)$			
	1.07579	5.2133			
Morse (K-H) [121]	$r_e(\mathring{A})$	$D_e(eV)$	α	$\sigma(\mathring{A})$	
	1.207	5.2133	2.7766	0.958	
Morse (C-F) [109]	$r_e(\mathring{A})$	$D_e(eV)$	α	$\sigma(\mathring{A})$	
	1.30	3.81	3.1068	1.077	

At low collision energies there exists orbiting collisions, wherein the scattering angles become infinite. This is a result of the attractive component of the potential, and therefore the purely repulsive VSS model does not exhibit this behavior. At higher collision energies such as those shown in figure 4.19 for a temperature of 100,000 K, the forces are predominantly repulsive. The scattering for the Morse (K-H) potential [121] is in best agreement with that of the potential of Varandas and Pais [20].

Figure 4.20 shows the dependence of the total collision cross-section on temperature for the various potentials considered in this work. It may be observed that the L-J potential has the largest total collision cross-section; while the VSS model is significantly smaller than all other potentials. In regards to computational efficiency

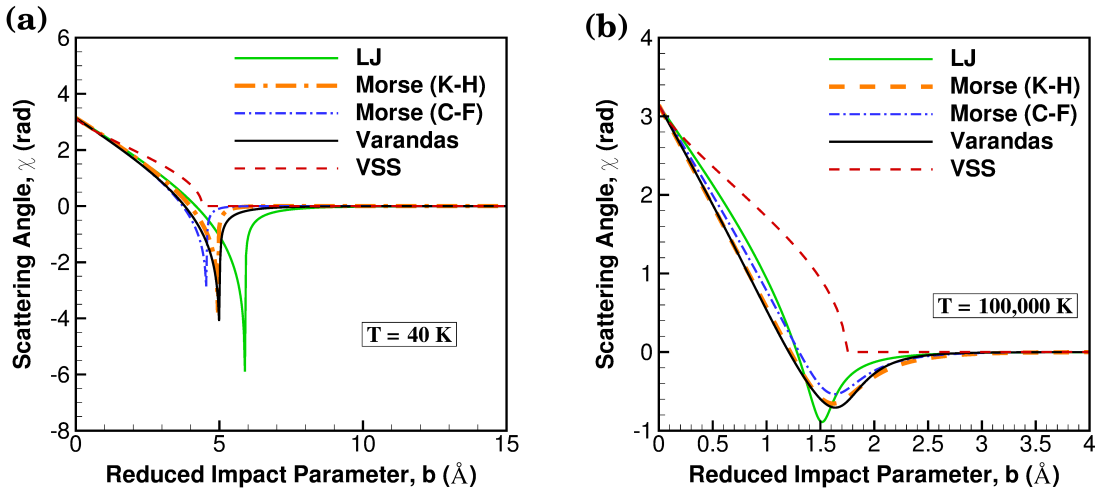

Figure 4.19.. Scattering angles as a function of impact parameter at (a) 40 K and (b) 100,000 K for VSS, L-J, Morse, and Varandas potentials

in the DSMC method, this implies that the VSS model is optimal since fewer collision events are occur. The total collision cross section for the potential of Varandas and Pais [20] is more comparable to the Morse (K-H) and Morse (C-F) potentials.

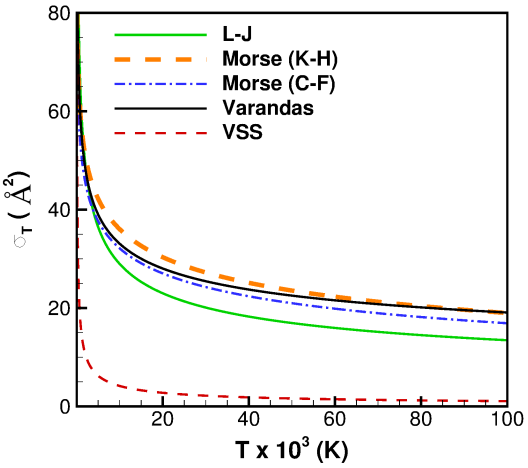

Figure 4.20.. Total collision cross-sections as a function of temperature for VSS, L-J, Morse, and Varandas potentials

Convenient expressions for computing the maximum reduced impact parameter as a function of reduced collision energy are also provided for the Morse and Varandas and Pais potentials. Logarithmic functions of the form,

$$b^*_{max}(\epsilon^*) = \left(\log(\epsilon^*) - B\right)/A\,, \tag{4.19}$$

and exponential functions of the form,

$$b^*_{max}(\epsilon^*) = \exp\left[\left(\log(\epsilon^*) - B\right)/A\right]\,, \tag{4.20}$$

may be used with the A and B parameters provided in table 4.13 to obtain the reduced impact parameters as a function of reduced collision energy. The use of these parameters neglects scattering angles less than 0.1 radians.

Table 4.13.. Parameters in collision cross-section expressions for Morse and Varandas and Pais potentials

Potential	A	B	Expression
Morse (K-H)	-2.37408099365	7.00079740986	$b^*_{max}(\epsilon^*) = \left(\log(\epsilon^*) - B\right)/A$
Morse (C-F)	-2.82074462832	7.29710727228	$b^*_{max}(\epsilon^*) = \left(\log(\epsilon^*) - B\right)/A$
Varandas and Pais	-8.36980407022	8.45885632883	$b^*_{max}(\epsilon^*) = \exp\left[\left(\log(\epsilon^*) - B\right)/A\right]$

The computational cost for calculating scattering angles scales with the complexity of the potential. Therefore, the *ab-initio* potential of Varandas and Pais [20] requires the most time of those considered in this work. On a personal laptop with a Intel Core 2.00 GHz i7-3537U CPU the computational cost of the Varandas and Pais potential is 4 seconds per scattering angle, while for the Morse (K-H) and Morse (C-F) potentials this cost is 0.2 seconds per scattering angle. The cost of using the L-J potential is half that at 0.1 seconds per scattering angle, and the VSS model is by far the most efficient with a cost of 2 microseconds per scattering angle. For implementation in particle-based methods such as DSMC, there are alternatives to directly calculating on-the-fly such as a polynomial approximation [37], or interpolating from pre-computed tables.

4.4.3 Collision Integrals and Transport Properties

The diffusion and viscosity-type collision integrals contributing to the first-approximation of the transport properties are compared for each intermolecular potential. The values of $\Omega^{*(1,1)}$ and $\Omega^{*(2,2)}$ are reported in tables 4.14 and 4.15 for each potential, and the deviations are reported relative to the *ab-initio* potential of Varandas and Pais [20].

Table 4.14.. Self-diffusion type collision integrals $\Omega^{(1,1)}$ for L-J, Morse, and Varandas and Pais potentials

	L-J		Morse (K-H)		Morse (C-F)		Varandas
$T(K)$	$\Omega^{(1,1)}(\mathring{A}^2)$	Dev. (%)	$\Omega^{(1,1)}(\mathring{A}^2)$	Dev. (%)	$\Omega^{(1,1)}(\mathring{A}^2)$	Dev. (%)	$\Omega^{(1,1)}(\mathring{A}^2)$
150	16.04	43.19	12.81	14.39	10.79	-3.68	11.20
300	12.72	35.21	11.56	22.92	9.70	3.12	9.41
500	10.72	28.50	10.69	28.26	8.95	7.34	8.34
1,000	8.50	17.52	9.55	32.05	7.98	10.38	7.23
2,000	6.74	6.10	8.39	32.07	7.03	10.70	6.35
4,000	5.34	-3.22	7.16	29.72	6.04	9.48	5.52
5,000	4.95	-6.14	6.75	27.93	5.70	8.19	5.27
6,000	4.65	-8.44	6.40	26.11	5.42	6.73	5.08
8,000	4.21	-11.59	5.84	22.71	4.94	3.76	4.76
10,000	3.89	-13.23	5.36	19.75	4.52	1.04	4.48
15,000	3.32	-13.47	4.38	14.12	3.69	-3.82	3.84
20,000	2.93	-11.26	3.65	10.41	3.10	-6.29	3.30

Collision integrals computed from the Morse (C-F) model are in best agreement with those from the potential of Varandas and Pais [20]. The root mean square deviation in the collision integrals are nearly 7%, whereas those computed from the Morse (K-H) model are on the order of 20%. This is despite the much better agreement of the intermolecular potential and scattering angles for the Morse (K-H) model. The L-J model, while possessing the same potential well depth as that of the Varandas and

Table 4.15.. Viscosity type collision integrals $\Omega^{(2,2)}$ for L-J, Morse, and Varandas and Pais potentials

	L-J		Morse (K-H)		Morse (C-F)		Varandas
$T(K)$	$\Omega^{(2,2)}(\mathring{A}^2)$	Dev. (%)	$\Omega^{(2,2)}(\mathring{A}^2)$	Dev. (%)	$\Omega^{(2,2)}(\mathring{A}^2)$	Dev. (%)	$\Omega^{(2,2)}(\mathring{A}^2)$
150	16.23	32.42	14.04	14.53	12.02	-1.97	12.26
300	12.90	26.73	12.31	20.93	10.58	3.96	10.18
500	10.89	21.58	11.11	24.00	9.59	7.04	8.96
1,000	8.65	13.47	9.56	25.46	8.31	9.06	7.62
2,000	6.87	6.58	8.13	26.10	7.13	10.56	6.44
4,000	5.46	0.14	6.81	24.97	6.02	10.57	5.45
5,000	5.07	-2.64	6.41	23.27	5.70	9.45	5.20
6,000	4.77	-5.00	6.11	21.74	5.44	8.42	5.02
8,000	4.33	-8.71	5.67	19.39	5.06	6.55	4.75
10,000	4.03	-11.33	5.34	17.49	4.75	4.51	4.54
15,000	3.53	-14.01	4.64	13.29	4.07	-0.75	4.10
20,000	3.17	-13.27	4.03	9.99	3.50	-4.48	3.66

Pais potential, the root mean square of the deviation is also nearly 20%. However, the maximum deviation is significantly larger for the L-J model in comparison to Morse (K-H) model. This occurs at relatively low collision energies where the differences in attractive forces have a more significant effect on scattering angles.

Self-diffusion coefficient and viscosity of ground-state oxygen shown in figure 4.21 follow similar trends as for the collision integrals. Remarkable agreement between the VSS model and Varandas and Pais [20] is observable, especially for viscosity. The maximum difference in viscosity is only 3% for the VSS model, while for the Morse (C-F) model this difference is 10%. These viscosity calculations are also in reasonably good agreement with those made by Banks and Kockarts [124] using a power law similar to the VHS model. The differences in self-diffusion coefficients relative to Varandas and Pais are comparable between Morse (C-F) and VSS models.

This demonstrates the success of the VSS model for its ability to match observed macroscopic properties of certain chemical species. Again, the Morse (C-F) model is in better agreement overall for both self-diffusion and viscosity calculations relative to the Morse (K-H) model, and the L-J model is in worst agreement.

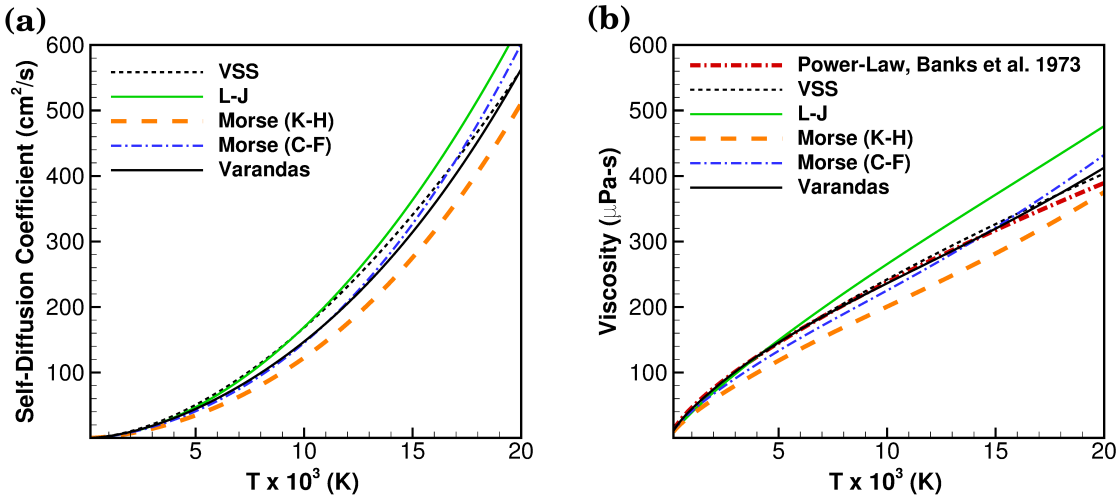

Figure 4.21.. (a) Self-diffusion and (b) viscosity variation with temperature for VSS, L-J, Morse, and Varandas potentials

5. INELASTIC COLLISION MODELING

Low-density, microscale, and hypersonic environments are each prone to experiencing non-equilibrium effects; which may significantly influence the design of systems operating in such environments. Non-equilibrium is a classification which may be described as any instance the characteristic time of the process of energy transfer is on the order of the transit time of the gas particles. Due to the scarcity of particles to collide with in low-density environments, insufficient number of transitions occur to allow for the energy modes to equilibrate. As for both microscale and hypersonic environments the transit time of the gas particles is short relative to the size of the body being studied and therefore leads to significant non-equilibrium effects. Accounting for these non-equilibrium effects is important for a variety of applications including the prediction of accurate heating rates on a re-entry vehicle [125] as well as flow structures and performances of supersonic microreactors/microthrusters. [126]

The need for accurate energy transfer rates amongst the internal modes of gas species has lead to the development of first-order perturbative, [127–129] empirical, [4, 130] forced harmonic oscillator [6, 131] (FHO) and FHO with free-rotations [132] (FHO-FR), quasi-classical multi-dimensional scattering theory, [133] close-coupled quantum-mechanical, [134–137] and quasi-classical trajectory [138] (QCT) methods. Each of these methods has increased complexity, and in the past quantifying the energy transfer rate in direct simulation Monte Carlo (DSMC) has been typically achieved using the empirically-based model of Larsen-Borgnakke (L-B). [4]

The L-B model uses inelastic collision numbers representing the number of collisions for relaxation based on experimental data, typically shock-tube studies. In addition, the total energy in any inelastic binary collision is redistributed amongst the two molecules so as to equilibrate them both immediately. Doing so during a relaxation process results in a progression of Boltzmann distributions at increasing/decreasing

temperatures as reported by Boyd and Josyula. [5] In this same paper, Boyd and Josyula [5] make a comparison of L-B to a FHO model developed by Adamovich et al. [6, 7] by presenting vibrational transition rates and non-Boltzmann distributions during a non-equilibrium, relaxation process. As with any model there are limitations and, for a numerical scheme, optimal implementations.

In this chapter, the practical limitations of the FHO model proposed by Adamovich et al. [6] will be clearly addressed as well as the challenges of implementing this model into a DSMC solver. This encompasses microscopic reversibility and the method employed to satisfy detailed balance, numerical round-off errors for high-energy collisions, limitation of second-order anharmonic oscillator model, reducing the number of quantum jumps possible, and a computational resource comparison between the L-B and FHO model implementations in DSMC. [139] Furthermore, a consistent elastic/inelastic collision model utilizing the FHO model is presented.

5.1 Theory of Larsen-Borgnakke (L-B) Energy Redistribution

The L-B model is described in detail by Bird [1] and is reiterated here for completeness. First, the collision energy, E_c, may be defined as the sum of relative translational and internal energies of the colliding molecules, $E_c = E_t + E_i$. The probability density for a combination of internal and translational energy may be written as a product per Eq. (5.1),

$$f(E_t, E_i) = E_t^{3/2-\omega} E_i^{\zeta-1} \exp\left[-\left(E_t + E_i\right) / \left(kT\right)\right], \tag{5.1}$$

where ζ is the number of degrees of freedom for the internal energy mode. Recalling that the collision energy is $E_t + E_i$, this may be substituted into the above equation, and the exponential term is a constant since the temperature is defined by the collision energy.

A specific internal energy mode may also be represented similar to Eq. (5.1) by replacing the internal energy term with the mode of interest. In this case, the distri-

bution function for vibrational energy is used; where the Dirac delta function allows for the discretization of the vibrational energy. The probability density may then be written as shown in Eq. (5.2).

$$f(E_t, E_v) = (E_c - E_v)^{3/2-\omega_{12}} \, \delta\left(E_v - ik\Theta_v\right) \exp\left[-E_c/\left(kT\right)\right] \tag{5.2}$$

The use of $ik\Theta_v$ in Eq. (5.2) implies a harmonic potential approximation for the vibrational levels, however a more accurate, anharmonic potential may be used instead. A vibrational transition then occurs in the L-B model according to a probability given by Eq. (5.3).

$$P_{i\to f} = \left(1 - \frac{fk\Theta_v}{E_c}\right)^{3/2-\omega_{12}} \tag{5.3}$$

This probability is a ratio of the probability of a particular level to the maximum probability.

Since the L-B model only redistributes the relative collision energies of collisions deemed to be inelastic, it is important to now discuss which collisions are inelastic. Collisions are considered to be inelastic according to collision numbers which result in the experimentally determined relaxation times. Thus, for vibrational relaxation times, Millikan and White's [1] expression may be written as $\tau = Z_v/\nu$, where ν is the mean collision frequency and Z_v is the collision number defined in Eq. (5.4).

$$Z_v = \left(C_1/T^{\omega}\right) \exp\left(C_2 T^{-1/3}\right). \tag{5.4}$$

The constants C_1 and C_2 are different for each molecular species, and the relaxation times are expressed with a temperature dependence.

The L-B model may be implemented serially such that each energy mode is treated one after the other. [1] The vibrational mode, as described above, is treated differently from the rotational mode owing to the relatively large spacing between energy levels.

When considering redistribution of energy to a single energy mode with two degrees of freedom, it can be shown that its inverse cumulative distribution function is [1]

$$\frac{E_a}{E_a + E_b} = 1 - R_f^{1/\Xi_b} \,. \tag{5.5}$$

The acceptance-rejection method [1] may be applied to Eq. (5.5) to determine the post-collision rotational energy, E_a, based on the sum of the remaining energies in the redistribution, E_b, the sum of the remaining average degrees of freedom, Ξ_b, and a uniformly sampled number, R_f. Thus, if the L-B model is applied serially, then only two energy modes are redistributed at a time.

A analytic expression for the sum of the remaining average degrees of freedom exists for the VSS model [1], but not for most others. For example, when considering redistribution of energy between the rotational and translational modes, Ξ_b will refer to the translational mode. This parameter is related to the average relative translational energy in collisions. This average is in regards to equilibrium conditions such that the average relative translational energy may be expressed in terms of the Boltzmann distribution as follows. [1]

$$\overline{E_t} = \frac{1}{2}\overline{m_r c_r^2} = \frac{\frac{1}{2}\int_0^\infty m_r c_r^2 \, \sigma_T c_r^3 \, \exp\left[-m_r c_r^2/(2kT)\right] \, \mathrm{d}c_r}{\int_0^\infty \sigma_T c_r^3 \, \exp\left[-m_r c_r^2/(2kT)\right] \, \mathrm{d}c_r} \tag{5.6}$$

For the VSS model, the evaluation of the Eq. (5.6) for the average relative translational energy reduces to the form,

$$\overline{E_t} = \left(\frac{5}{2} - \omega\right) kT \,. \tag{5.7}$$

The average degrees of freedom, Ξ_b, is then equal to the factor, $\left(\frac{5}{2} - \omega\right)$. When considering other potentials such as the Born-Mayer potential, Eq. (5.6) must be evaluated numerically in order to determine the average degrees of freedom. It is then possible, as will be discussed in Section 5.4.2, to fit a polynomial to the average degrees of freedom as a function of collision energy.

5.2 Theory of Forced Harmonic Oscillator (FHO) Model for V-V-T Transitions

The vibrational energy transfer for the FHO model, on the other hand, is based on the semi-classical formulation for collinear diatom-diatom interactions of Zelechow *et al.* [131]. For completeness, the formulation for the FHO model between an atom and a diatom is provided in Appendix B. It is a semi-classical formulation because it treats the translational mode classically but the vibrational mode quantum mechanically. Essentially, the FHO model represents the initial vibrational wavefunctions as stationary harmonic oscillators and perturbs them through some force according to the intermolecular model (assumed to be exponential repulsive here) to a final, stationary harmonic oscillator wavefunction. The probability of a vibrational-vibrational-translational energy transition is given by Eq. (5.8), where the subscripts i_1, i_2 and f_1, f_2 refer to initial and final states of molecules 1 and 2, respectively.

$$\begin{aligned} P_{i_1,i_2\to f_1,f_2}(\bar{v}) = & \left| \sum_{r=0}^{q} (-1)^{i_1+i_2-r} \, \mathcal{C}_{r+1,i_2+1}^{(i_1+i_2)} \, \mathcal{C}_{r+1,f_2+1}^{(f_1+f_2)} \, \epsilon^{(i_1+i_2+f_1+f_2)/2-r} \, \mathrm{e}^{-\epsilon/2} \right. \\ \times & \sqrt{(i_1+i_2-r)!(f_1+f_2-r)!} \, \mathrm{e}^{-i(f_1+f_2-r)\rho} \\ \times & \left. \sum_{p=0}^{q-r} \frac{(-1)^p}{(i_1+i_2-r-p)!(f_1+f_2-r-p)!p!\epsilon^p} \right|^2 \end{aligned} \tag{5.8}$$

In the previous expression for the V-V-T transition probability, ϵ is the total energy of an oscillator at rest subjected to the transient force of the interaction,

$$\epsilon = S_{VT} \frac{8\pi^3 \omega m_r^2 \gamma^2}{\alpha^2 h \mu} \, \sinh^{-2}\left(\frac{\pi\omega}{\alpha\bar{v}}\right) . \tag{5.9}$$

The parameter, ρ, is defined as

$$\rho = \left(S_{VV} \frac{\alpha^2 \bar{v}^2}{\omega_1 \omega_2} \right)^{1/2} \tag{5.10}$$

and the coefficients $\mathcal{C}_{ij}^{(n)}$ denote the transformation matrix, [131]

$$\mathcal{C}_{ij}^{(n)} = 2^{-n/2} \binom{n}{k-1}^{1/2} \binom{n}{j-1}^{-1/2} \sum_{\nu=0}^{j-1} (-1)^{n-1-\nu} \binom{n-k+1}{j-\nu-1} \binom{k-1}{\nu} . \tag{5.11}$$

The summations in Eq. (5.8) include q and $q - r$ terms, where q is the minimum of $(i_1 + i_2, f_1 + f_2)$. S_{VT} and S_{VV} are steric factors accounting for non-collinear effects [6, 7], and i without a subscript is $\sqrt{-1}$.

In Eq. (5.9) and (5.10) m_r is the collision-reduced mass between molecules AB and CD $m_r = m_{AB}m_{BA}/(m_{AB}+m_{BA})$, μ is the oscillator-reduced mass $\mu = m_A m_B/(m_A + m_B)$, $\gamma = m_B/(m_A + m_B)$, and $\bar{v}$ is the symmetrized collision velocity, $\bar{v} = (v_i + v_f)/2$ discussed more in Section 5.3.1.

5.3 Forced Harmonic Oscillator (FHO) Model Implementation in DSMC

5.3.1 Detailed Balance and Microscopic Reversibility

Microscopic reversibility is a more fundamental principle which leads to detailed balance under equilibrium conditions. Reif [140] describes microscopic reversibility as a process which is invariant under the reversal of the time from t to -t. In terms of transition probabilities, the relation in Eq. (5.12) states that the probability of a forward transition is equal to the reverse transition.

$$P_{i\to f}(E_i) = P_{f\to i}(E_f) \tag{5.12}$$

In the previous equation E_i refers to the initial energy involved in the transition, E_f is the final energy as a result of the transition, and i and f are the initial and final states, respectively.

Detailed balance may be observed for a system of molecules if the rate of molecules transitioning from state i to f is equal to the rate of the molecules transitioning from state f to i. Thus, detailed balance will be satisfied if the product of the population of molecules in state i and the transition rate from state i to f is equal to the product of the population of molecules in state f and the transition rate from state f to i,

$$\mathrm{e}^{-\mathcal{E}_i/kT}\, K_{i\to f}(T) = \mathrm{e}^{-\mathcal{E}_f/kT}\, K_{f\to i}(T)\,. \tag{5.13}$$

Since detailed balance refers to an equilibrium conditions, the transition rate $K(T)$ is an integration over the Boltzmann distribution,

$$\mathrm{e}^{-\mathcal{E}_i/kT}\, K_{i\to f}(T) = \mathrm{e}^{-\mathcal{E}_i/kT}\, 4\pi \left(\frac{\mu}{2\pi kT}\right)^{3/2} \int_0^\infty v_i^3 \exp\left[\frac{-\mu v_i^2}{2kT}\right] P_{i\to f}(v_i)\sigma_T(v_i)\,\mathrm{d}v_i\,. \tag{5.14}$$

Thus, a velocity symmetrization [6], $\bar{v}$, is introduced so that detailed balance and microscopic reversibility may be satisfied. This is an arithmetic average of the initial and final velocities so that Eq. (5.12) may be rewritten as

$$P_{i\to f}(\bar{v}) = P_{f\to i}(\bar{v}), \qquad \bar{v} = \frac{v_i + v_f}{2} \tag{5.15}$$

The right hand side of Eq. (5.13) may be subtracted from the left hand side and final velocity substituted as a function of initial velocity shown in Eq. (5.16).

$$v_f = \sqrt{v_i^2 + 2(\mathcal{E}_i - \mathcal{E}_f)/\mu} \tag{5.16}$$

With this substitution, the integrations are with respect to the same variable and the integrand must be equal to zero for the detailed balance to be satisfied. After simplification, the ratio of total cross-sections is found to be inversely proportional to the velocities.

$$\frac{v_i^2}{v_f^2} = \frac{\sigma_T(v_f)}{\sigma_T(v_i)} \tag{5.17}$$

Satisfying both microscopic reversibility and detailed balance simultaneously puts a severe limitation on the form of the intermolecular potential used. Instead, an arbitrary intermolecular potential such as VHS may be used and detailed balance ensured by multiplying the de-excitation probability by a factor which would satisfy Eq. (5.17). To express this explicitly, refer to Eq. (5.18) below.

$$P_{i\to f}(\bar{v}) = \frac{v_i^2\sigma_T(v_i)}{v_f^2\sigma_T(v_f)} P_{f\to i}(\bar{v}) \tag{5.18}$$

5.3.2 Reduction in Round-Off Errors

Round-off errors become significant at higher energies where the instantaneous total energy parameter, ϵ, is large. High values of ϵ, as defined in Eq. (5.9), cause the $\epsilon^{(i_1+i_2+f_1+f_2)/2}$ and ϵ^p terms to be large. The inner summation of Eq. (5.8) contains ϵ^p in the denominator and hence each term of the summation is small; while the $(-1)^p$ factor further reduces the summed value through alternating signs. These are two areas in which round-off errors in the calculation of transition probabilities are significant.

The round-off error induced by the first term containing the sum of the initial and final states in the exponent, $\epsilon^{(i_1+i_2+f_1+f_2)/2}$, may be dealt with by applying a cut-off value beyond which a more reasonable probability is set. This is simple to implement as all that is required is a conditional statement as shown in listing 1.

```
! Check if (1/2)(i1 + i2 + f1 + f2) lnε > 128
!
If (0.5*(i1+i2+f1+f2)*log(epsil) .GT. 128.0)  Then
    Prob = 1.0e-4              ! P_{i1,i2 → f1,f2}(v̄) = 10^{-4}
End If
```

Listing 1: Pseudo-code for limiting round-off errors originating from large values of $\epsilon^{(i_1+i_2+f_1+f_2)/2}$

The cut-off value of 128 and set value of 10^{-4} have been found to reduce the round-off errors, and hence are included in the above conditional statement for clarity.

The inner summation of Eq. (5.8) causes round-off errors due to the differences of small values and may therefore be reduced by checking the minimum value in the summation. If this minimum value is less than another specified cut-off value; while simultaneously the condition in listing 1 is true, then again assign a more reasonable value for the probability. A snippet of pseudo-code is provided in listing 2.

```
! Sum = Sum + (-1)^p ε^(i1+i2+f1+f2)/2-r-p / p!(i1+i2-r-p)!(f1+f2-r-p)!
!
If (abs(Sum) .LT. abs(Min))  Then
    Min = Sum
End If
!    ⋮
! After exiting both summation loops...
If ((log(abs(Min) .LT. -42.0) .AND.
&  0.5*(i1+i2+f1+f2)*log(epsil) .GT. 128.0)  Then
      Prob = 1.0e-4     ! P_{i1,i2 → f1,f2}(v̄) = 10^-4
End If
```

Listing 2: Pseudo-code for limiting round-off errors originating from inner summation

To illustrate the effects of the round-off errors, comparisons are made to both calculations involving higher-precision arithmetic and the algorithms stated in listings 1 and 2. Diatomic molecules which have higher dissociation energies such as N_2 are expected to induce larger round-off errors in the transition probability computations, but these errors were studied for both N_2 and O_2. Figure 5.1(a) compares double precision with quadruple precision computations for the $(18, 18 \rightarrow 17, 18)$ transition while figure 5.1(b) is for the $(20, 20 \rightarrow 18, 20)$ transition during N_2-N_2 collisions.

While quadruple precision eliminates the errors observed from double precision calculations, it only delays the round-off errors to slightly higher energies. This is an inevitable problem which causes high-energy transitions to occur with absolute certainty, but a cut-off may be set to circumvent the issue. It may be observed from figures 5.1(a) and 5.1(b) that the probabilities at the higher energies indicated by the solid blue lines are small - on the order of 10^{-4}.

Oxygen molecules have lower dissociation energies and have been observed to have only about a 4 km/s region in which the round-off errors are significantly high, and

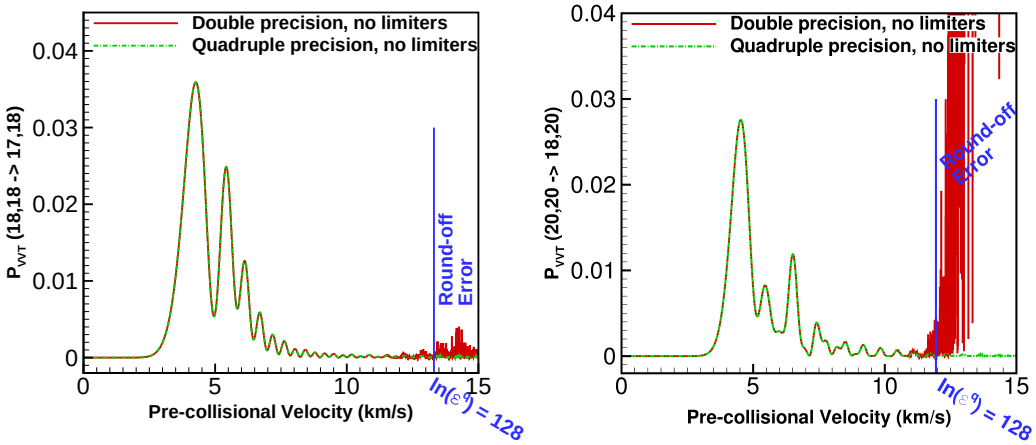

(a) (18,18 - 17,18) transition

(b) (20,20 - 18,20) transition

Figure 5.1.. Round-off errors for high-energy N_2–N_2 V-V-T transfers using double and quadruple precision

beyond this region double precision is acceptable. Both conditions as expressed in listing 2 must be satisfied simultaneously to validate setting the probability to 10^{-4}, but near pre-collisional velocities of 13 km/s for the $(20, 20 \rightarrow 18, 20)$ transition the errors originating from the inner summation loop drastically reduce. This trend is shown for the $(18, 18 \rightarrow 17, 18)$ and $(20, 20 \rightarrow 18, 20)$ transitions in figures 5.2(a) and 5.2(b), respectively.

The accuracy of using the prescribed limits on the transition probabilities is illustrated in figures 5.3(a)- 5.4(b). Relative to the double precision cases without limiters, the use of limiters clearly reduces the errors such that the probabilities are at least the same order of magnitude.

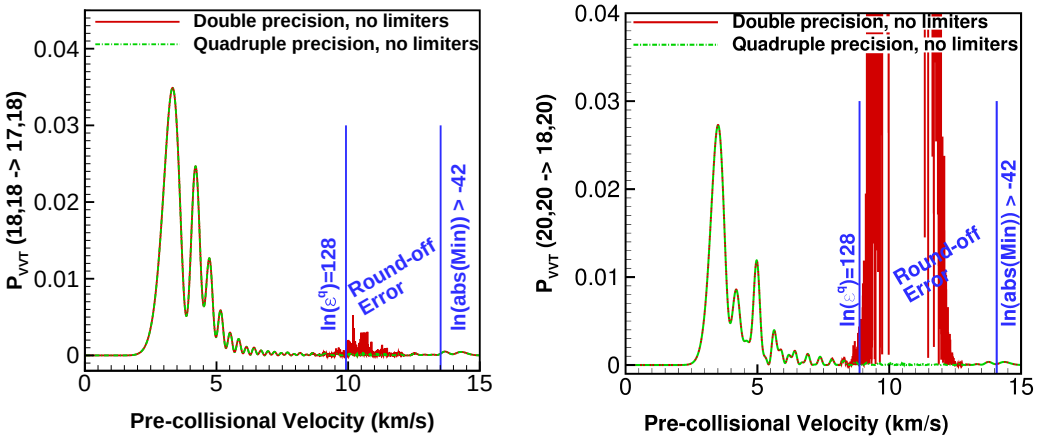

(a) (18,18 - 17,18) transition (b) (20,20 - 18,20) transition

Figure 5.2.. Round-off errors for high-energy O_2–O_2 V-V-T transfers using double and quadruple precision

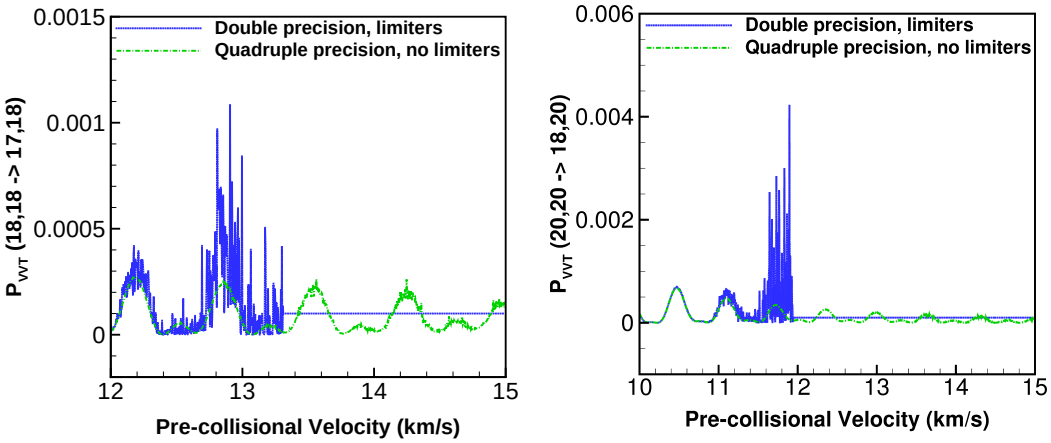

(a) (18,18 - 17,18) transition (b) (20,20 - 18,20) transition

Figure 5.3.. Region for use of limiters for high-energy N_2–N_2 V-V-T transfers using double and quadruple precision

5.4 Consistent Elastic/Inelastic Collision Model Using the Forced Harmonic Oscillator (FHO)

It was mentioned in Section 5.2 that the FHO model is based on the Born-Mayer exponential repulsive potential. Therefore, the scattering angles and total collision

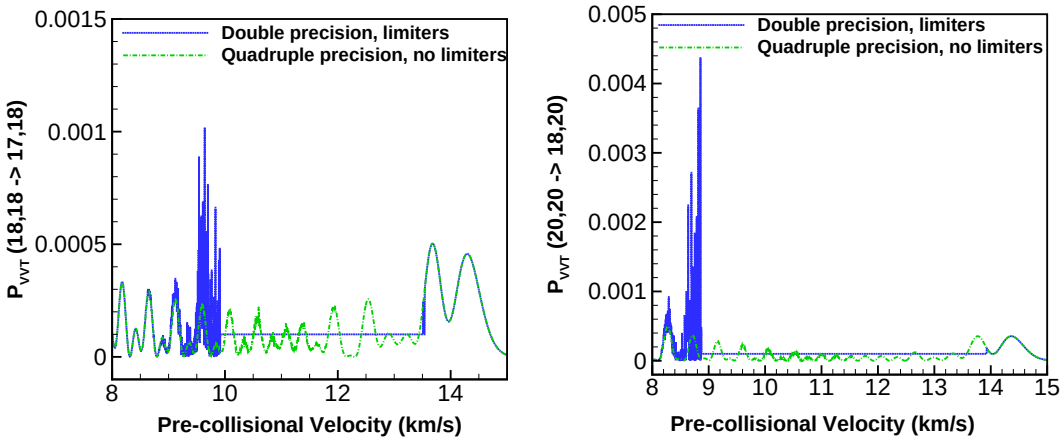

(a) (18,18 - 17,18) transition

(b) (20,20 - 18,20) transition

Figure 5.4.. Region for use of limiters for high-energy O_2–O_2 V-V-T transfers using double and quadruple precision

cross-sections should also be based on the same Born-Mayer exponential repulsive potential in order to be consistent. Although this may seem the most logical path, often times computational burdens prevents such paths to be taken. To help understand why, recall the scattering angle calculations in Chapter 2. When no analytic expressions exist, the numerical evaluation of Eq. (2.6) must be used instead. This is the case for the Born-Mayer potential. Thus, one alternative to circumvent additional computations within DSMC is to use the VSS model.

With the current state of computer technology, it is possible to either pre-compute scattering angles and store in memory or to directly evaluate the scattering angles. One could even follow the work of Norman *et al.* [66] and use GPUs to accelerate the scattering angle calculations. The focus of this section is on the assessment of the consistent elastic/inelastic collision model relative to the more commonly used VSS model combined with the FHO model.

5.4.1 Equilibrium Vibrational Transition Rate Coefficients

Both the FHO and L-B models have parameters which may be adjusted to fit measured or more accurate vibrational transition rate coefficients. For the FHO model, the parameters are S_{VT} and S_{VV} in Eq. (5.9) and (5.10), respectively, to account for 3-D effects. For the L-B model, the parameters are C_1 and C_2 in Eq. (5.4) to define the vibrational collision number. If the Born-Mayer potential is to also be used for the elastic collisions, then the pre-exponential factor, A, must also be specified. This section details the choice in the FHO and L-B parameters based on comparisons to the 3-D quantum classical calculations of Billing and Fisher. [134]

Adamovich *et al.* [6] had determined a value of 4.4 $\mathring{A}^{-1}$ for the Born-Mayer interaction range parameter, α, best fits the N_2 transition rate coefficient data of Billing and Fisher [134] The pre-exponential factor, A, which best fits the viscosity data of Lemmon and Jacobsen [68] is determined to be $2 \times 10^{-14}\,J$. Using these parameters, the numerical procedure detailed in Section 2.8 is used to compute the transport properties of molecular nitrogen with the Born-Mayer potential. Agreements between the Born-Mayer potential using the proposed model parameters and the VSS model using the recommended parameters in Table 4.9 with viscosity measurements of Lemmon and Jacobsen [68] are illustrated in Figure 5.5.

The VSS model is observed to be in better agreement with viscosity measurements than the Born-Mayer potential at temperatures less than 1,000 K but begins to deviate at higher temperatures. Molecular nitrogen has a characteristic vibrational temperature of more than 3,000 K, and therefore agreement at higher temperatures will be important for the relaxation process. Unfortunately, no viscosity measurements were found for molecular nitrogen beyond 2,200 K, but theoretical results presented by Stallcop *et al.* [23] agree well with viscosities computed from the Born-Mayer potential.

It is worthwhile to mention that a new set of VSS parameters may be obtained for temperatures greater than 1,000 K in a similar manner as outlined in Section 4.2. In

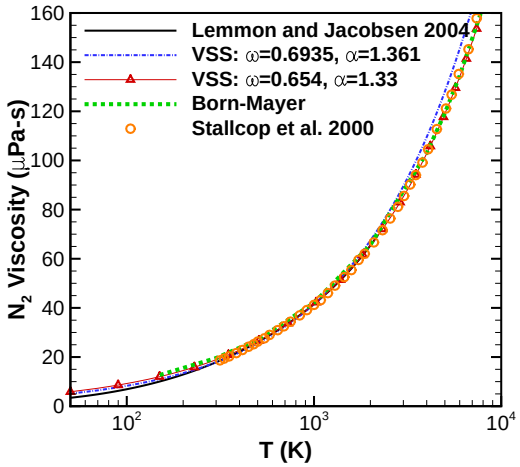

Figure 5.5.. Molecular nitrogen viscosities using Born-Mayer and VSS potentials

doing so, better agreement with viscosity measurements and theoretical calculations at higher temperatures is achieved. The higher temperature VSS parameters are: $\omega = 0.654, \alpha = 1.33, T_{ref} = 1035K$, and $\mu_{ref} = 42.48\mu Pa \cdot s$.

Once the Born-Mayer potential parameters are specified, the next step is to determine the FHO parameters, S_{VT} and S_{VV}, for both the Born-Mayer-FHO and VSS-FHO models. This is accomplished through comparisons of the de-excitation rate coefficient from states (1,0) to (0,0) for S_{VT} and from states (1,0) to (0,1) for S_{VV}. In addition, a comparison is made to L-B rate coefficients using C_1 and C_2 parameters recommended by Bird [1] and those suggested presently to better match computations of Billing and Fisher. [134] The spectroscopic constants, ω_e and $\omega_e\chi_e$, used by the FHO model [6] are as reported by Laurendeau [31] to be 2358.57 cm^{-1} and 14.324 cm^{-1}, respectively.

Figure 5.6(a) shows that every model is in excellent agreement with the computations of Billing and Fisher [134], with the exception of L-B with Bird's [1] parameters. It may be observed from Figure 5.6(b) that neither L-B model compares well with computations of Billing and Fisher, but both Born-Mayer-FHO and VSS-FHO are

in good agreement. Only a slight improvement is noticeable at lower temperatures with the use of the Born-Mayer-FHO model. No discernible differences between the two VSS-FHO models are present in Figures 5.6(a)- 5.7(b), and therefore only the VSS-FHO model with model parameters recommended in Table 4.9 are shown.

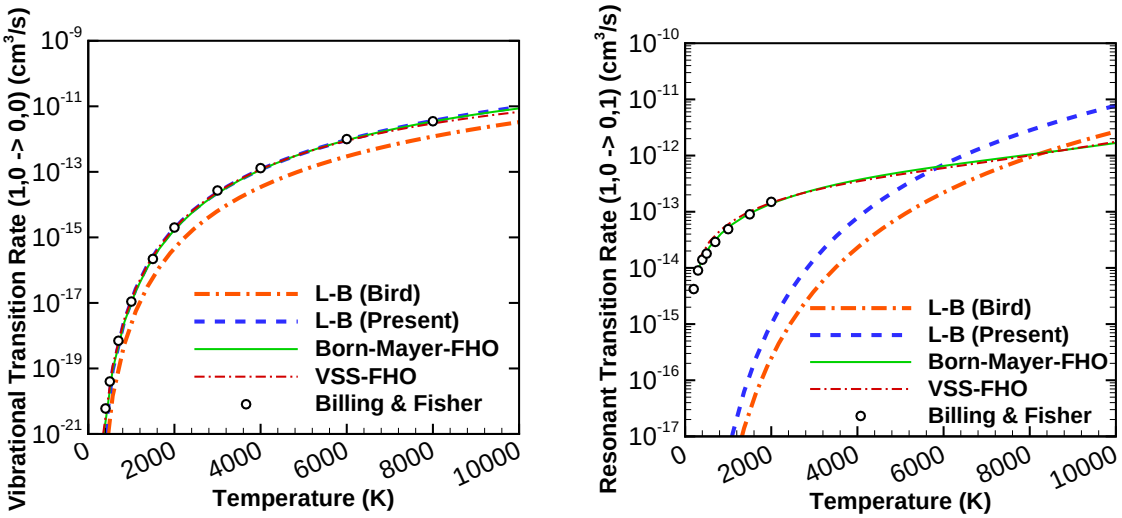

(a) (1,0 - 0,0) transition

(b) (1,0 - 0,1) transition

Figure 5.6.. V-V-T transitions for N_2 using L-B model with Bird's [1] parameters: $C_1 = 9.1, C_2 = 220$, L-B model with present parameters: $C_1 = 5, C_2 = 210$, VSS-FHO, and Born-Mayer-FHO models

De-excitation rate coefficients for higher vibrational levels are also compared in Figures 5.7(a) and 5.7(b). In both cases, the Born-Mayer-FHO and VSS-FHO models agree well with each other until approximately 2,000 K where the Born-Mayer-FHO model begins to predict higher rate coefficients. Neither L-B model compares well with computations of Billing and Fisher [134] for either case. For the transition from states (10,5) to (9,5), the lower rate coefficient computed with the VSS-FHO model is in better agreement with computations of Billing and Fisher [134]. The computations of Billing and Fisher [134] lie in between the Born-Mayer-FHO and VSS-FHO models beyond 4,000 K for the transition from states (20,10) to (19,10). These trends are somewhat reversed for the multi-quantum jump from states (10,5) to (8,5).

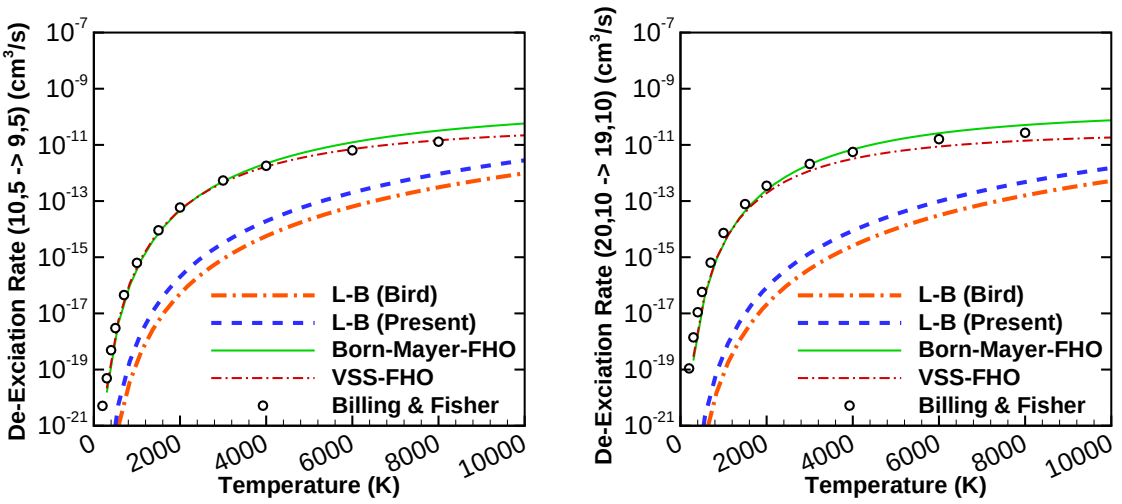

(a) (10,5 - 9,5) transition

(b) (20,10 - 19,10) transition

Figure 5.7.. V-V-T transitions for N_2 using L-B model with Bird's [1] parameters: $C_1 = 9.1, C_2 = 220$, L-B model with present parameters: $C_1 = 5, C_2 = 210$, VSS-FHO, and Born-Mayer-FHO models

Figure 5.8 shows the VSS-FHO model to predict higher transition rate coefficients over much of the 200–10,000 temperature range than the Born-Mayer-FHO model. Moreover, the VSS-FHO model is also in better agreement with the more accurate quantum-classical calculations of Billing and Fisher [134] at these temperatures. There are no observable differences between the two L-B models for this transition and tend to underpredict the transition rates beyond about 1,500 K. These differences in transition rate coefficients will be important for the 1-D normal shock wave calculations in the later section.

5.4.2 Vibrational Relaxation in 0-D Heat Bath

One simple analysis to study the vibrational relaxation processes in DSMC is the 0-D heat bath analysis. This is a zero bulk velocity flow where the translational and rotational temperatures are set at an initial temperature, $T_{t,0}$, and the vibrational

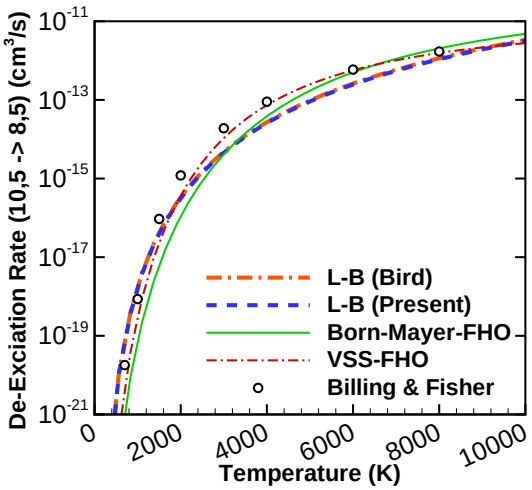

Figure 5.8.. V-V-T (10,5 - 8,5) transition for N_2 using L-B model with Bird's [1] parameters: $C_1 = 9.1, C_2 = 220$, L-B model with present parameters: $C_1 = 5, C_2 = 210$, VSS-FHO, and Born-Mayer-FHO models

temperature set to an initial temperature, $T_{v,0}$. The molecules system will tend to relax towards an equilibrium state where each energy mode may be represented by the same temperature, T. This relaxation process occurs as a result of the molecular collisions, which are modeled in DSMC with the Born-Mayer-FHO and VSS-FHO models.

The FHO model accounts only for V-V-T transitions, and therefore the serial implementation of the L-B model is still used to redistribute the energy to the rotational mode. Thus, as mentioned in Section 5.1, the use of a Born-Mayer potential with the L-B model requires the numerical evaluation of Eq. (5.6) to determine the average degrees of freedom, Ξ_b. This integration has been performed with a similar, adaptive quadrature technique as that used in the transport property calculations of Section 2.8. The integration was based on a specified tolerance of 10^{-14} and a fourth-order polynomial fit,

$$\Xi_b = \frac{\overline{E_t}}{kT} = \frac{a}{k}T^3 + \frac{b}{k}T^2 + \frac{c}{k}T + \frac{d}{k} + \frac{e}{k}T^{-1}\,. \tag{5.19}$$

The coefficients in Eq. (5.19) correspond to the $N_2 - N_2$ interaction with the Born-Mayer potential and are: $a = -1.3434045425 \times 10^{-38}, b = 7.32629672251 \times 10^{-34}, c = -1.75679134942 \times 10^{-29}, d = 2.63077087383 \times 10^{-23}$, and $e = 4.9293203878 \times 10^{-23}$. This particular fit was determined using the Born-Mayer potential parameters listed in Table 5.1.

Table 5.1.. Physical and numerical parameters for 0-D heat bath analysis

Parameter	Value
T_t	8,000 K
T_r	8,000 K
T_v	0 K
n	$10^{18}\, m^{-3}$
Δx	0.25 m
Δt	68 μs
Number of molecules	100,000
Born-Mayer α	4.4 $\mathring{A}^{-1}$
A	$2 \times 10^{-14}\, J$
ω	0.70
VSS α	1.37
(Born-Mayer, VSS) S_{VT}	(1/25, 1/7)
(Born-Mayer, VSS) S_{VV}	(1/110, 1/40)

Figure 5.9 shows that the relaxation process for a stationary gas is nearly the same whether the VSS or Born-Mayer models are used with the FHO model. Only slight differences are observable later in the relaxation process. However, the vibrational mode for the VSS-LB model using values of $C_1 = 9.1$ and $C_2 = 220$ relax much more slowly than the other two models. This result is consistent with previous studies regarding the VSS-FHO model. [5, 141]

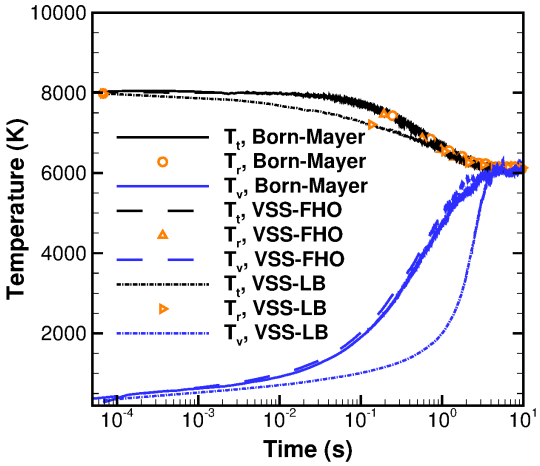

Figure 5.9.. 0-D N_2 heat bath comparing Born-Mayer-FHO, VSS-FHO, and VSS-LB models

5.4.3 Vibrational Relaxation Across a 1-D Normal Shock Wave

The consistent elastic/inelastic collision model is investigated in this section for its effect on 1-D normal shock wave density and temperature profiles. Two Mach numbers, three and ten, are studied to test a range of collision energies. At Mach 3 the energies are substantially less than the characteristic vibrational temperature of 3,393 K for ground-state molecular nitrogen. Therefore, only the translational and rotational modes are equilibrating within this short distance.

The conditions for the Mach 3 flow are as follows. The upstream number density and temperatures are $n = 10^{20}\, m^{-3}$ and $T_t = T_r = T_v = 293\, K$, respectively. An upstream velocity of 1,047 m/s corresponding to Mach 3 flow of molecular nitrogen at 293 K is specified. A number of real to simulated molecules ratio of 5×10^{15} is set with a total number of 300 sampling cells and 1800 collision cells. A time step of 0.1 μs is used for each model based on approximately 1% of the molecule transit time across a cell and the mean collision frequency. The collision cell width is 167 μm and corresponds to roughly 5% of the mean free path, λ. Unless otherwise stated,

the rotational numbers are assumed equal to a constant value of 5, as reported by Bird. [1]

Figures 5.10(a) and 5.10(b) show the density and temperature profiles across a Mach 3 shock wave. First, note that both sets of VSS parameters result in negligible differences in both number density and temperature profiles, and therefore the results are shown for the recommended parameters in table 4.9. It may also be observed that the VSS-FHO and VSS-LB models are in excellent agreement with each other. This is expected since the L-B method is used in both models for redistribution to the rotational mode. The notable difference is the Born-Mayer-FHO model (labeled B-M for short); which relaxes much more quickly than the rest. Since the effective degrees of freedom, Eq. (5.19), has changed the rotational collision number, Z_r, should also change. Therefore, a constant rotational collision number of 13 is found to agree well with both density and temperature calculations across the shock.

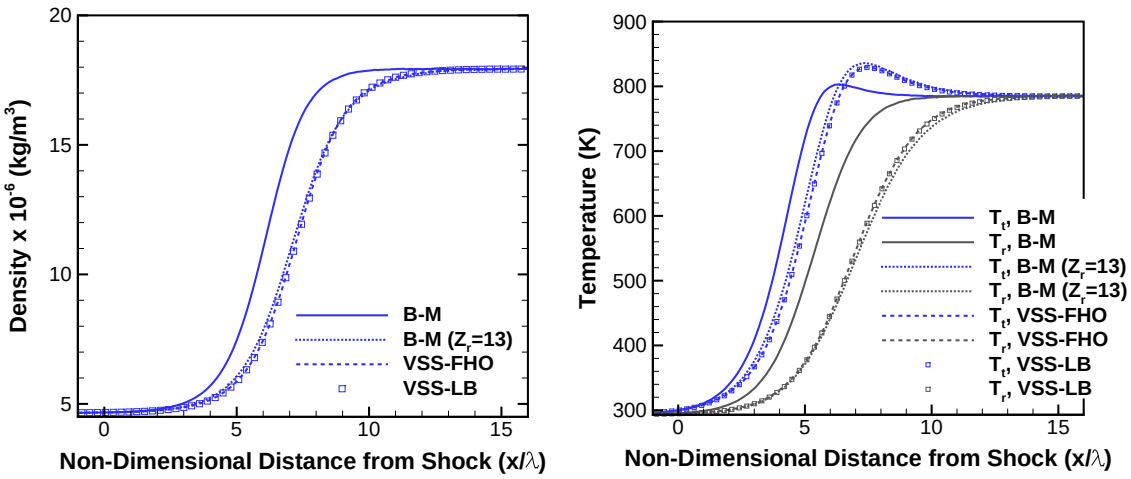

(a) Density profile

(b) Temperature profile

Figure 5.10.. Density and temperature profiles across a Mach 3 normal shock wave using Born-Mayer-FHO, VSS-FHO, and VSS-LB models

At Mach 10 the translational temperatures across the shock jump to about 6,000 K, and therefore both rotational and vibrational modes may be observed to relax behind the shock. The conditions for the Mach 10 flow are as follows. The upstream number density and temperatures are the same as for the Mach 3 flow: $n = 10^{20}\, m^{-3}$ and $T_t = T_r = T_v = 293\, K$, respectively. An upstream velocity of 3,489.9 m/s corresponding to Mach 10 flow of molecular nitrogen at 293 K is specified. The number of real to simulated molecules ratio is increased from the Mach 3 flow to 5×10^{16}, and a total number of 2,000 sampling cells and 10,000 collision cells are used. A time step of 32 ns is used for each model based on approximately 1% of the molecule transit time across a cell and the mean collision frequency. The collision cell width is 800 μm and corresponds to roughly 5% of the mean free path.

Figures 5.11(a) and 5.11(b) show the density and temperature profiles for molecular nitrogen across a Mach 10 shock wave. With these larger temperature variations, more significant differences may be observed between the models. The density increases the slowest for the VSS-FHO model using the high temperature VSS parameters because the equilibration between the translational and rotational modes is the slowest for this model. The Born-Mayer-FHO model is shown to equilibrate the rotational mode the quickest, such that a higher rotational collision number may be preferred for higher energy flows. This is in agreement with a similar conclusion recently made by Adamovich. [142]

Deviations in vibrational temperature between both the VSS-FHO models and the Born-Mayer-FHO model increase with distance downstream of the shock. The reason for the slower vibrational relaxation of the Born-Mayer-FHO model may point towards the much lower excitation rates for the multi-quantum jumps, as shown in Fig. 5.8. Since both models use the FHO model, then the difference in multi-quantum transition rates originates from the collision cross-section. As may be observed in Fig. 5.5, the Born-Mayer potential predicts higher viscosities at relatively low temperatures (below 1000 K). This indicates the cross-section of the Born-Mayer potential is too small, and therefore the smaller cross-section at lower temperatures reduces decreases

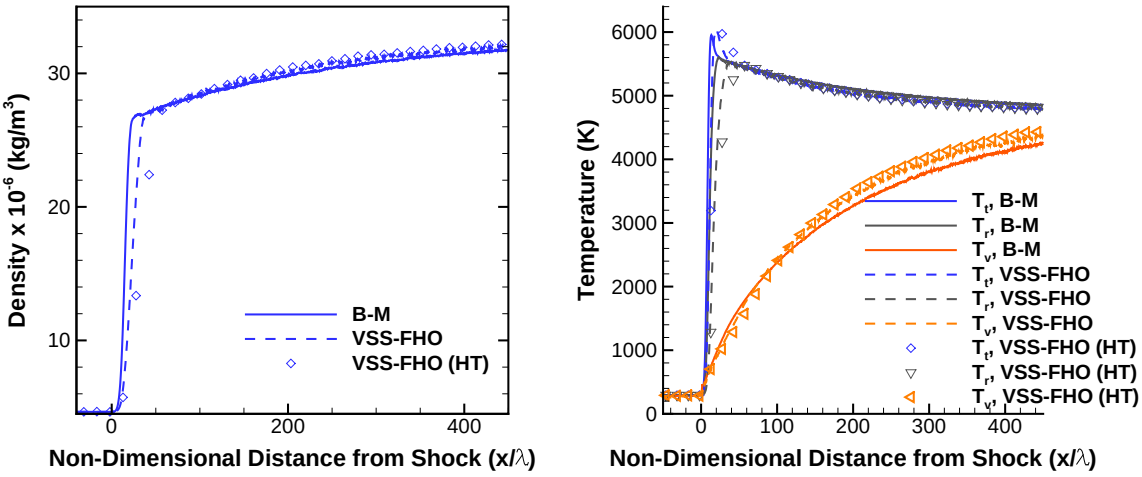

(a) Density profile

(b) Temperature profile

Figure 5.11.. Density and temperature profiles across a Mach 10 normal shock wave using Born-Mayer-FHO and VSS-FHO models. VSS refers to the recommended model parameters in Table 4.9, VSS (HT) is with the high-temperature parameters: $\omega = 0.654, \alpha = 1.33$

the number of transitions causing multi-quantum jumps. Vibrational level populations at two locations, $x/\lambda = 296.3$ and $x/\lambda = 518.5$, are shown in Fig. 5.12(a), and confirm that higher vibrational levels are more heavily populated for the VSS-FHO model.

Translational, rotational, and vibrational temperatures are shown in Fig. 5.12(b) for Mach 10 flow across a shock using Born-Mayer-FHO and VSS-LB models. The use of the VSS-LB model with C_1 and C_2 constants calibrated to match Billing and Fisher [134] data clearly results in a much faster relaxation time. Using the vibrational collision number constants, C_1 and C_2, as recommended by Bird [1] results in a slightly slower relaxation of the vibrational mode, as is consistently found in literature. [5, 141] Therefore, the vibrational collision number constants determined through comparisons to Billing and Fisher [134] give poor agreement with both the

Born-Mayer-FHO and VSS-FHO models and the parameters from Bird [1] should be used instead.

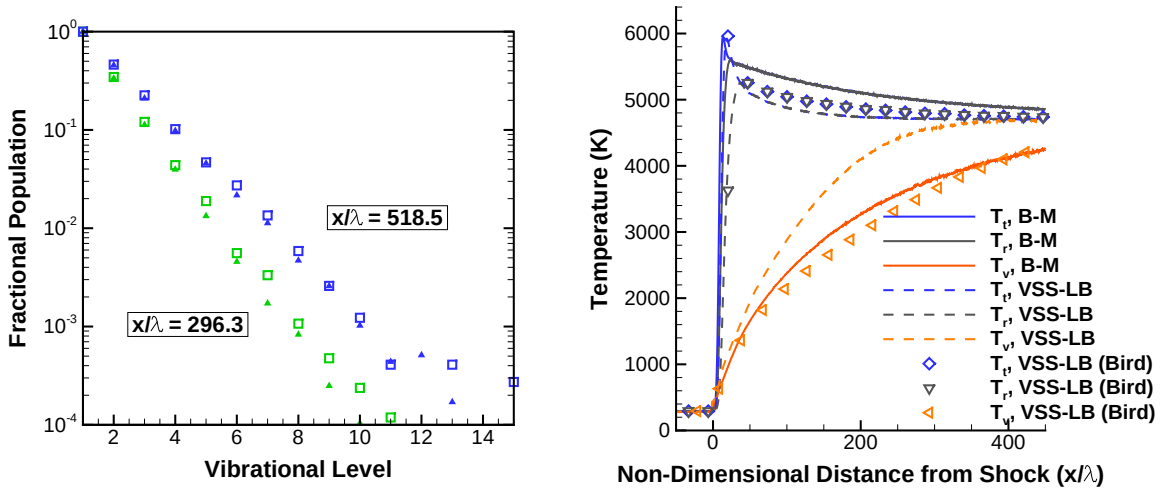

(a) Vibrational populations

(b) Temperature profile

Figure 5.12.. (a) Vibrational level populations using *triangles*: Born-Mayer-FHO, *squares*: VSS-FHO (HT) (b) temperature profiles across a Mach 10 normal shock wave using Born-Mayer-FHO and VSS-LB models. VSS-LB (Bird) uses $C_1 = 9.1, C_2 = 220$, and VSS-LB model uses $C_1 = 5, C_2 = 210$

6. SUMMARY

Advances in computer technology over the decades has allowed for more complex physics to be modeled in the DSMC method. Beginning with the first paper on DSMC in 1963, 30,000 collision events per hour were simulated using a simple hard sphere model. Today, more than 10 billion collision events can be simulated per hour for the same problem. Many new and more physically realistic collision models such as the Lennard-Jones potential and the forced harmonic oscillator model have been introduced into DSMC. The fact that computer resources are more readily available and higher-fidelity models have been developed should not necessitate their usage. It is important to understand how such high-fidelity models affect the output quantities of interest in engineering applications. The effect of elastic and inelastic collision models on compressible Couette flow, ground-state atomic oxygen transport properties, and normal shock waves have therefore been investigated.

Effects of intermolecular interaction models are evaluated in DSMC through the analysis of compressible Couette flow in the slip and transitional regimes. Flows in the continuum and slip regimes involving wide temperature ranges are expected to be most affected by the choice of molecular models. This includes flows with moderate to strong shock waves, in-space propulsion and vacuum technology. The theory of polynomial approximations was used to represent the scattering angle for the LJ potential using a two-variable polynomial of degree 7. The formulation for the scattering angle was first verified via equilibrium collision frequency calculations for argon. The agreement for viscosity between the two models is within 5% at a temperature of 273 K. On the other hand, at a temperature of 40 K the higher viscosity of the VHS model leads to a shear stress that is about 28% higher than the LJPA shear stress due to the importance of the attractive component of the force between molecules. At 1,000 K the VHS model predicts a 12% higher shear stress

than the LJPA model, and again over-predicts the viscosity relative to experimental measurements. The DSMC simulations performed using the LJPA model were shown to reproduce the theoretical LJ potential viscosity of all three cases to within 3.5%.

The large difference in shear stress between the VHS and LJ models observed for the low-temperature Couette flow diminishes as the Knudsen number is increased. Only a 7% difference is observed for a Knudsen number of 1, and this trend is in agreement with what is expected as the flow approaches the free-molecular limit. Comparisons of 2-D velocity distribution functions relative to the equilibrium distribution function for the VHS and LJ models also indicate more significant differences at lower Knudsen numbers. A larger skewness in the velocity distribution function for the VHS model provides more evidence that the VHS model experiences a higher degree of nonequilibrium at the lower Knudsen numbers. In the free-molecular limit, there are no molecular collisions and hence the intermolecular potential plays no role in the velocity distribution functions.

The LJPA model has a computational cost that is comparable to the VHS and GSS models with an increase largely attributed to the higher number of collisions due to long-range nature of the LJ potential. The polynomial expansion approach enhances the fidelity of DSMC simulations and may be applied to other complex intermolecular potentials.

Effects of VSS and L-J model parameters on transport property calculations have been investigated and new parameters are recommended for 8 common gases. Appropriate choice of model parameters drastically improves the accuracy of viscosity, self-diffusion coefficient, and thermal conductivity predictions over a wide temperature range of 20–2200 K. L-J and VSS model parameters based on a compilation of correlations and *ab-initio* calculations for shear viscosity, thermal conductivity, and self-diffusion have thus been recommended.

Viscosities, thermal conductivities, and self-diffusion coefficients are more accurately predicted by the VSS model for lighter gases such as H_2, and He. For such light gases, the range of influence for the attractive forces would be minimal. Ranges

of validity are increased to cover temperatures up to 2200 K. In contrast, the heavier gases such as Ar and Xe have deeper potential wells and therefore the attractive forces are more important over a wider temperature range. The agreement between the L-J model and measured viscosity and self-diffusion for heavier gases support this statement.

In general, agreement between transport properties computed using the VSS model and accurate experimental measurements and *ab-initio* calculations is improved for heavier gases if higher reference temperatures are used. Doing so improves the agreement at higher temperatures at the expense of lower temperatures, including ambient temperatures.

With the technological advancement of computers in the past few decades, it has become possible to implement more complex intermolecular potentials in methods involving the transport of gas species, such as DSMC. As a step to incorporate more complex potentials in either state-to-state kinetic models or DSMC, a kinetic theory code has been developed to compute collision cross-sections, binary scattering angles, transport collision integrals, and transport properties from arbitrary potentials. An accurate *ab-initio* potential from Varandas and Pais [20] has been compared to both empirically and *ab-initio* based Morse potentials, (12-6) L-J potential, and VSS model for ground-state oxygen.

Curve fits for the total collision cross-section are provided for both the Morse (K-H) and Morse (C-F) potentials as well as for the Varandas and Pais potential. These fits neglect scattering angles less than 0.1 radians, and are therefore more suitable for DSMC simulations with respect to computational efficiency. Model parameters for the VSS model based on viscosity calculations from the Varandas and Pais potential are also provided.

At both low collision energies typical of a 40 K gas and high collision energies of a 100,000 K gas the Morse (K-H) model is in best agreement with the *ab-initio* potential of Varandas and Pais. Despite this fact, the Morse (C-F) model is in better agreement for the transport collision integrals and transport properties. Viscosity and

self-diffusion calculations using the VSS model are also in surprisingly good agreement (within 3%) with those using the Varandas and Pais potential.

Directly computing the scattering angles for the Varandas and Pais potential requires a factor of twenty more time than for the L-J potential; while the Morse potentials require only two times more. The VSS model is nearly 10,000 times faster than the L-J potential. Thus, the VSS model may be used to a reasonable accuracy while significantly reducing the computational cost. Alternatively, one may interpolate between tabulated scattering angles as a function of collision energy and impact parameter to reduce the cost of any potential at the expense of system memory.

When considering inelastic collision models in DSMC, the most popular is the Larsen-Borgnakke (L-B) model. This is an efficient method which satisfies detailed balance, but is a purely phenomenological model. The forced harmonic oscillator (FHO) model is a semi-classical formulation which has more ties to the quantum physics describing such collisions. However, it requires significantly more computational resources within DSMC and extra steps to satisfy detailed balance.

The FHO model is based on the Born-Mayer potential, but is often times implemented in DSMC with a VSS model for the elastic collisions. The effect of using a VSS-FHO model relative to a consistent Born-Mayer-FHO model is investigated through comparisons of a 0-D heat bath 1-D normal shock waves.

Born-Mayer potentials are more valid at higher collision energies, and at the lower temperatures the cross-section is too small resulting in lower multi-quantum transition rates. This is the likely cause for the slower relaxation of the Born-Mayer-FHO model relative to the VSS-FHO model in the Mach 10 shock wave. Comparisons with the VSS-LB model indicate vibrational collision number constants obtained through calibration with Billing and Fisher [134] rates cause unreasonably fast relaxation of the vibrational mode. The constants from Bird [1] result in better agreement, albeit slower relaxation than Born-Mayer-FHO, and are recommended instead.

REFERENCES

REFERENCES

[1] G. A. Bird. *Molecular Gas Dynamics and the Direct Simulation of Gas Flows*. Oxford University Press, New York, 2nd revised edition, 1994.

[2] James Jeans. *An Introduction to the Kinetic Theory of Gases*. Cambridge University Press, Cambridge, 1 edition, 1967.

[3] S. Chapman and T.G. Cowling. *The Mathematical Theory of Non-Uniform Gases*. Cambridge University Press, Cambridge, 1970.

[4] Claus Borgnakke and Poul S. Larsen. Statistical Collision Model for Monte Carlo Simulation of Polyatomic Gas Mixture. *J. Comput. Phys.*, 18:405–420, 1975.

[5] Iain D. Boyd and Eswar Josyula. State resolved vibrational relaxation modeling for strongly nonequilibrium flows. *Phys. Fluids*, 23(5):057101–1—-057101–9, 2011.

[6] Igor V. Adamovich, Sergey O. Macheret, J. William Rich, and Charles E. Treanor. Vibrational Relaxation and Dissociation behind Shock Waves Part 1: Kinetic Rate Models. *AIAA J.*, 33(6):1064–1069, 1995.

[7] Igor V. Adamovich, Sergey O. Macheret, J. William Rich, and Charles E. Treanor. Vibrational energy transfer rates using a forced harmonic oscillator model. *J. Thermophys. Heat Transf.*, 12(1):57–65, 1998.

[8] G.A. Bird. Monte-carlo simulation in an engineering context. *Progr. Astro. Aero.*, 74:239–255, 1981.

[9] K. Koura and H. Matsumoto. Variable soft sphere molecular model for inverse-power-law or Lennard-Jones potential. *Physics of Fluids A: Fluid Dynamics*, 3:2459, 1991.

[10] Katsuhisa Koura and Hiroaki Matsumoto. Variable soft sphere molecular model for air species. *Phys. Fluids A*, 4:1083–1085, 1992.

[11] J. E. Lennard-Jones. On the Forces between Atoms and Ions. *Proc. R. Soc. A Math. Phys. Eng. Sci.*, 109(752):584–597, 1925.

[12] Jason Sanders and Edward Kandrot. *CUDA by Example: An introduction to general-purpose GPU programming*. Addison-Wesley, Upper Saddle River, NJ, 2011.

[13] Benjamin K Bergen, Marcus G Daniels, and Paul M Weber. A hybrid programming model for compressible gas dynamics using OpenCL. In *Parallel Processing Workshops (ICPPW), 2010 39th International Conference on*, pages 397–404. IEEE, 2010.

[14] NVIDIA Corp. Gpu applications: Transforming computational research and engineering, Oct. 2013.

[15] G.A. Bird. Approach to Translational Equilibrium in a Rigid Sphere Gas. *Phys. Fluids*, 6(10):1518, 1963.

[16] G.A. Bird. Aspects of the Structure of Strong Shock Waves. *Phys. Fluids*, 13(5):1172, 1970.

[17] M.S. Ivanov, S.V. Rogasinsky, and V. Ya. Rudyak. Direct statistical simulation method and master kinetic equation. *Progr. Astro. Aero.*, 117:171–181, 1989.

[18] G.A. Bird. Perception of numerical methods in rarefied gas dynamics. *Progr. Astro. Aero.*, 118:211–226, 1989.

[19] Katsuhisa Koura. A set of model cross sections for the monte carlo simulations of rarefied real gases: atom-diatom collisions. *Phys. Fluids*, 6(10):3473–3486, 1994.

[20] A.J.C. Varandas and A.A.C.C. Pais. A realistic double many-body expansion (DMBE) potential energy surface for ground-state O 3 from a multiproperty fit to ab initio calculations, and to experimental spectroscopic, inelastic scattering, and kinetic isotope thermal rate data. *Mol. Phys.*, 65(4):843–860, 1988.

[21] Eugene Levin, Harry Partridge, and James R. Stallcop. Collision Integrals and High Temperature Transport Properties for N-N, O-O, and N-O. *J. Thermophys. Heat Transf.*, 4(4):469, 1990.

[22] Ira N. Levine. *Quantum Chemistry*. Prentice-Hall, Upper Saddle River, 5 edition, 2000.

[23] James Stallcop, Harry Partridge, and Eugene Levin. Effective potential energies and transport cross sections for interactions of hydrogen and nitrogen. *Phys. Rev. A*, 62(6):062709, 2000.

[24] Harry Partridge, James R. Stallcop, and Eugene Levin. Potential energy curves and transport properties for the interaction of He with other ground-state atoms. *J. Chem. Phys.*, 115(14):6471, 2001.

[25] James Stallcop, Harry Partridge, and Eugene Levin. Effective potential energies and transport cross sections for atom-molecule interactions of nitrogen and oxygen. *Phys. Rev. A*, 64(4):042722, 2001.

[26] Richard Jaffe, David W. Schwenke, Galina Chaban, and Winifred Huo. Vibrational and Rotational Excitation and Relaxation of Nitrogen from Accurate Theoretical Calculations. In *46th AIAA Aerosp. Sci. Meet. Exhib.*, pages 1–14, Reno, 2008. AIAA.

[27] A.T. Droege and P.C. Engelking. Supersonic expansion cooling of electronically excited oh radicals. *Chem. Phys. Let.*, 96(3):316–318, 1983.

[28] A. Kersch, W. Morokoff, and Chr. Werner. Selfconsistent simulation of sputter deposition with the Monte Carlo method. *J. Appl. Phys.*, 75(4):2278, 1994.

[29] Walter G. Vincenti and Jr. Kruger, Charles H. *Introduction to physical gas dynamics*. Krieger Publishing Company, Malabar, 1965.

[30] J. O. Hirschfelder, C. F. Curtiss, and R. B. Bird. *Molecular Theory of Gases and Liquids*. Wiley, New York, 1954.

[31] Normand M Laurendeau. *Statistical thermodynamics: fundamentals and applications*. Cambridge University Press, 2005.

[32] M.W. Chase, C.A. Davies, J.R. Downey, D.R. Frurip, R.A. McDonald, and A.N. Syverd. Janaf thermochemical tables, third edition. *J. Phys. Chem. Ref. Data, Supplement No. 1*, 14:1–1856, 1985.

[33] Malcolm W. Jr. Chase. Nist-janaf thermochemical tables, fourth edition. *J. Phys. Chem. Ref. Data, Monograph*, 9, 1998.

[34] HA Hassan and D.B. Hash. A generalized hard-sphere model for Monte Carlo simulation. *Physics of Fluids A: Fluid Dynamics*, 5:738, 1993.

[35] Max Born and Joseph E Mayer. Zur gittertheorie der ionenkristalle. *Zeitschrift für Physik*, 75(1-2):1–18, 1932.

[36] H. Matsumoto and K. Koura. Comparison of velocity distribution functions in an argon shock wave between experiments and Monte Carlo calculations for Lennard-Jones potential. *Physics of Fluids A: Fluid Dynamics*, 3:30–38, 1991.

[37] A. Venkattraman and A.A. Alexeenko. Binary scattering model for Lennard-Jones potential: Transport coefficients and collision integrals for non-equilibrium gas flow simulations. *Physics of Fluids*, 24:027101, 2012.

[38] G. Colonna and A. Laricchiuta. General numerical algorithm for classical collision integral calculation. *Comput. Phys. Commun.*, 178(11):809–816, 2008.

[39] C K Birdsall and a B Langdon. *Plasma Physics via Computer Simulation*. IOP Publishing Ltd, New York, 1991.

[40] G. A. Bird. *Molecular Gas Dynamics*. Oxford University Press, New York, 1976.

[41] Katsuhisa Koura. Null-collision technique in the direct-simulation Monte Carlo method. *Phys. Fluids*, 29(11):3509–3511, 1986.

[42] MS Ivanov and SV Rogasinsky. Analysis of numerical techniques of the direct simulation monte carlo method in the rarefied gas dynamics. *Russian Journal of numerical analysis and mathematical modelling*, 3(6):453–466, 1988.

[43] J. Fan. A generalized soft-sphere model for Monte Carlo simulation. *Physics of Fluids*, 14:4399, 2002.

[44] W.L. Dimpfl, I.J. Wysong, S.F. Gimelshein, M. Braunstein, and L.S. Bernstein. Application of the Born-Mayer potential with a hard-sphere scattering kernel to rarefied hyperthermal gas flow modeling. In *AIP Conference Proceedings*, volume 1084, 2008, page 323, 2008.

[45] M. N. Macrossan. [mu]-DSMC: a general viscosity method for rarefied flow. *Journal of Computational Physics*, 185(2):612–627, 2003.

[46] J. Davis, R. G. Dominy, J. K. Harvey, and M. N. Macrossan. An evaluation of some collision models used for Monte Carlo calculations of diatomic rarefied hypersonic flows. *Journal of Fluid Mechanics*, 135:355–371, 1983.

[47] Paolo Valentini and Thomas E. Schwartzentruber. Large-scale molecular dynamics simulations of normal shock waves in dilute argon. *Phys. Fluids*, 21(6):066101, 2009.

[48] Felix Sharipov and Jose L. Strapasson. Direct simulation monte carlo method for an arbitrary intermolecular potential. *Physics of Fluids*, 24(1):011703, 2012.

[49] Andrew B Weaver, A Venkattraman, and Alina A Alexeenko. Effect of intermolecular potential on compressible couette flow in slip and transitional regimes. *Physics of Fluids (1994-present)*, 26(10):107102, 2014.

[50] G. A. Bird. *The DSMC Method*. G. A. Bird, Sydney, 2013.

[51] S. Chapman and T.G. Cowling. *The Mathematical Theory of Non-Uniform Gases: An Account of the Kinetic Theory of Viscosity, Thermal Conduction and Diffusion in Gases*. Cambridge Univ Press, 1990.

[52] G.C. Maitland and E.B. Smith. Critical reassessment of viscosities of 11 common gases. *Journal of Chemical and Engineering Data*, 17(2):150–156, 1972.

[53] J. Kestin, K. Knierim, E. A. Mason, B. Najafi, S. T. Ro, and M. Waldman. Equilibrium and transport properties of the noble gases and their mixtures at low density. *J. Phys. Chem. Ref. Data*, 13(1):229–303, 1984.

[54] MS Ivanov and SF Gimelshein. Computational hypersonic rarefied flows. *Annual Review of Fluid Mechanics*, 30(1):469–505, 1998.

[55] GJ LeBeau. A parallel implementation of the direct simulation Monte Carlo method. *Computer methods in applied mechanics and engineering*, 174(3-4):319–337, 1999.

[56] SF Gimelshein, AA Alexeenko, and DA Levin. Modeling of the interaction of a side jet with a rarefied atmosphere. *Journal of Spacecraft and Rockets*, 39(2):168–176, 2002.

[57] J. Balakrishnan, I.D. Boyd, and D.G. Braun. Monte Carlo simulation of vapor transport in physical vapor deposition of titanium. *Journal of Vacuum Science & Technology A: Vacuum, Surfaces, and Films*, 18:907, 2000.

[58] A. Venkattraman and AA Alexeenko. Direct simulation Monte Carlo modeling of e-beam metal deposition. *Journal of Vacuum Science & Technology A: Vacuum, Surfaces, and Films*, 28(4):916–924, 2010.

[59] Walter H. Stockmayer and James A. Beattie. Determination of the Lennard-Jones Parameters from Second Virial Coefficients Tabulation of the Second Virial Coefficient. *J. Chem. Phys.*, 10(7):476–477, 1942.

[60] S. A. Lebedeff. Determination of the Lennard-Jones Parameters from Total Scattering Cross-Section Measurements. *J. Chem. Phys.*, 40(9):2716–2721, 1964.

[61] Emmerich Wilhelm and Rubin Battino. Estimation of Lennard-Jones (6,12) Pair Potential Parameters from Gas Solubility Data. *J. Chem. Phys.*, 55(8):4012, 1971.

[62] Daxu Yin and Alexander D. Mackerell. Combined Ab Initio / Empirical Approach for Optimization of Lennard-Jones Parameters. *J. Comput. Chem.*, 19(3):334–348, 1998.

[63] K. a. Stephani, D. B. Goldstein, and P. L. Varghese. Consistent treatment of transport properties for five-species air direct simulation Monte Carlo/Navier-Stokes applications. *Phys. Fluids*, 24(7):077101, 2012.

[64] Ayyaswamy Venkattraman and Alina A Alexeenko. Direct simulation monte carlo modeling of metal vapor flows in application to thin film deposition. *Vacuum*, 86(11):1748–1758, 2012.

[65] Masoud Darbandi and Ehsan Roohi. Study of subsonic–supersonic gas flow through micro/nanoscale nozzles using unstructured dsmc solver. *Microfluidics and nanofluidics*, 10(2):321–335, 2011.

[66] Paul Norman, Paolo Valentini, and Thomas Schwartzentruber. GPU-accelerated Classical Trajectory Calculation Direct Simulation Monte Carlo applied to shock waves. *J. Comput. Phys.*, 247:153–167, 2013.

[67] Paolo Valentini, Patrick A Tump, Chonglin Zhang, and Thomas E Schwartzentruber. Molecular dynamics simulations of shock waves in mixtures of noble gases. *Journal of Thermophysics and Heat Transfer*, 27(2):226–234, 2013.

[68] E. W. Lemmon and R. T Jacobsen. Viscosity and Thermal Conductivity Equations for Nitrogen, Oxygen, Argon, and Air. *Int. J. Thermophys.*, 25(1):21–69, 2004.

[69] E. Bich, J. Millat, and E. Vogel. The viscosity and thermal conductivity of pure monatomic gases from their normal boiling point up to 5000 K in the limit of zero density and at 0.101325 MPa. *J. Phys. Chem. Ref. Data*, 19(6):1289, 1990.

[70] Edward B. Winn. The Temperature Dependence of the Self-Diffusion Coefficients of Argon, Neon, Nitrogen, Oxygen, Carbon Dioxide, and Methane. *Phys. Rev.*, 80(6):1024–1027, 1950.

[71] Philip J. Bendt. Measurements of He3-He4 and H2-D2 Gas Diffusion Coefficients. *Phys. Rev.*, 110(1):85–89, 1958.

[72] Normand C. Blais and Joseph B. Mann. Thermal Conductivity of Helium and Hydrogen at High Temperatures. *J. Chem. Phys.*, 32(5):1459–1465, 1960.

[73] Wojciech Cencek, Micha Przybytek, Jacek Komasa, James B. Mehl, Bogumi Jeziorski, and Krzysztof Szalewicz. Effects of adiabatic, relativistic, and quantum electrodynamics interactions on the pair potential and thermophysical properties of helium. *J. Chem. Phys.*, 136(22):224303, 2012.

[74] Eckhard Vogel, Benjamin Jäger, Robert Hellmann, and Eckard Bich. pair potential energy curve for the argon atom pair and thermophysical properties for the dilute argon gas. II. Thermophysical properties for low-density argon. *Mol. Phys.*, 108(4):3335–3352, 2010.

[75] Eckard Bich, Robert Hellmann, and Eckhard Vogel. Ab initio potential energy curve for the neon atom pair and thermophysical properties for the dilute neon gas. II. Thermophysical properties for low-density neon. *Mol. Phys.*, 106(6):813–825, 2008.

[76] John J. Hurly and Michael R. Moldover. Ab Initio Values of the Thermophysical Properties of Helium as Standards. *J. Res. Natl. Inst. Stand. Technol.*, 105(5):667–688, 2000.

[77] John A Nelder and Roger Mead. A simplex method for function minimization. *The computer journal*, 7(4):308–313, 1965.

[78] Jeffrey C. Lagarias, James A. Reeds, Margaret H. Wright, and Paul E. Wright. Convergence Properties of the Nelder–Mead Simplex Method in Low Dimensions. *SIAM J. Optim.*, 9(1):112–147, 1998.

[79] Eric F. May, Robert F. Berg, and Michael R. Moldover. Reference Viscosities of H2, CH4, Ar, and Xe at Low Densities. *Int. J. Thermophys.*, 28(4):1085–1110, 2007.

[80] James B. Mehl, Marcia L. Huber, and Allan H. Harvey. Ab initio transport coefficients of gaseous hydrogen. *Int. J. Thermophys.*, 31:740–755, 2010.

[81] J. Kestin, S.T. Ro, and W.A. Wakeham. Viscosity of the noble gases in the temperature range 25-700°C. *J. Chem. Phys.*, 56(8):4119–4124, 1972.

[82] J. Kestin and W. A. Wakeham. The viscosity and diffusion coefficient of binary mixtures of nitrous oxide with he, ne and co. *Ber. Bunsenges. Phys. Chem.*, 87:309–311, 1983.

[83] E. Vogel. Präzisionsmessungen des viskositätskoeffizienten von stickstoff und den edelgases zwischen raumtemperatur und 650 k. *Ber. Bunsenges. Phys. Chem.*, 88:997–1002, 1984.

[84] J Kestin and W Leidenfrost. An absolute determination of the viscosity of eleven gases over a range of pressures. *Physica*, 25(7):1033–1062, 1959.

[85] J Kestin and A Nagashima. Viscosity of neonhelium and neonargon mixtures at 20 and 30 c. *J. Chem. Phys.*, 40(12):3648–3654, 1964.

[86] R DiPippo, J Kestin, and K Oguchi. Viscosity of three binary gaseous mixtures. *J. Chem. Phys.*, 46(12):4758–4764, 1967.

[87] GP Flynn, RV Hanks, NA Lemaire, and J Ross. Viscosity of nitrogen, helium, neon, and argon from78.5 to 100 c below 200 atmospheres. *J. Chem. Phys.*, 38(1):154–162, 1963.

[88] C. Evers, H.W. Lösch, and W. Wagner. An Absolute Viscometer-Densimeter and Measurements of the Viscosity of Nitrogen , Methane , Helium , Neon , Argon , and Krypton over a Wide Range of Density and Temperature. *Int. J. Thermophys.*, 23(6):1411–1439, 2002.

[89] Daniel Seibt, Eckhard Vogel, Eckard Bich, Daniel Buttig, and Egon Hassel. Viscosity Measurements on Nitrogen. *J. Chem. Eng. Data*, 51(2):526–533, 2006.

[90] Robert Hellmann. Ab initio potential energy surface for the nitrogen molecule pair and thermophysical properties of nitrogen gas. *Mol. Phys.*, 111(3):387–401, 2013.

[91] Eric F. May, Michael R. Moldover, Robert F. Berg, and John J. Hurly. Transport properties of argon at zero density from viscosity-ratio measurements. *Metrologia*, 43(3):247–258, 2006.

[92] E. Vogel. Reference Viscosity of Argon at Low Density in the Temperature Range from 290 K to 680 K. *Int. J. Thermophys.*, 31(3):447–461, 2010.

[93] J. T. Zhang, H. Lin, and J. Che. Effects of connecting tubing on a two-capillary viscometer. *Metrologia*, 50(4):377–384, 2013.

[94] Herrick L. Johnston and Edward R. Grilly. The Thermal Conductivites of Eight Common Gases between 80 and 380K. *J. Chem. Phys.*, 14(4):233–238, 1946.

[95] P.C. Jain and S.C. Saxena. Thermal conductivity and effective diffusion coefficient for vibrational energy: oxygen (4001600 K). *Mol. Phys.*, 33(1):133–138, 1977.

[96] William A. Wakeham, Akira Nagashima, and J. V. Sengers. *Measurement of the transport properties of fluids*, volume 3. Blackwell Science Inc, 1991.

[97] J. Kestin, R. Paul, A.A. Clifford, and W.A. Wakeham. Absolute determination of the thermal conductivity of the noble gases at room temperature up to 35 MPa. *Physica A.*, 100(2):349–369, 1980.

[98] J. Millat, M. Ross, W. A. Wakeham, and M. Zalaf. The thermal conductivity of neon, methane and tetrafluoromethane. *Physica A: Statistical Mechanics and its Applications*, 148(1):124–152, 1988.

[99] JW Haarman. Thermal conductivity measurements of he, ne, ar, kr, n2 and co2 with a transient hot wire method. In *TRANSPORT PHENOMENA1973: Second Annual International Centennial Boltzmann Seminar*, volume 11, pages 193–202. AIP Publishing, 1973.

[100] K. Stephan, R. Krauss, and A. Laesecke. Viscosity and Thermal Conductivity of Nitrogen for a Wide Range of Fluid States. *J. Phys. Chem. Ref. Data*, 16(4):993–1023, 1987.

[101] Y. Y. Duan, L. Q.. Sun, L. Shi, M. S. Zhu, and L. Z Han. Thermal Conductivity of Gaseous Trifluoroiodomethane (CF_3I). *J. Chem. Eng. Data*, 42(5):890–893, 1997.

[102] George Ś Springer and Elwood W Wingeier. Thermal conductivity of neon, argon, and xenon at high temperatures. *The Journal of Chemical Physics*, 59(5):2747–2750, 1973.

[103] Marc J Assael, Malcolm Dix, Albert Lucas, and William A Wakeham. Absolute determination of the thermal conductivity of the noble gases and two of their binary mixtures as a function of density. *Journal of the Chemical Society, Faraday Transactions 1: Physical Chemistry in Condensed Phases*, 77(2):439–464, 1981.

[104] J. C. Liner and Stanley Weissman. Determination of the Temperature Dependence of Gaseous Diffusion Coefficients Using Gas Chromatographic Apparatus. *J. Chem. Phys.*, 56(5):2288–2290, 1972.

[105] G. A. DuBro and Stanley Weissman. Measurements of Gaseous Diffusion Coefficients. *Phys. Fluids*, 13(11):2682–2688, 1970.

[106] Frank M. Mourits and Frans H. A. Rummens. A critical evaluation of Lennard-Jones and Stockmayer potential parameters and of some correlation methods. *Can. J. Phys.*, 55:3007–3020, 1977.

[107] S.C. Saxena, M. P. Saksena, and R. S. Gambhir. The thermal conductivity of non-polar polyatomic gases. *Br. J. Appl. Phys.*, 15(7):843–849, 1964.

[108] K. S. Yun and E. A. Mason. Collision Integrals for the Transport Properties of Dissociating Air at High Temperatures. *Phys. Fluids*, 5(4):380, 1962.

[109] M. Capitelli and E. Ficocelli V. Collision integrals of oxygen atoms in different electronic states. *J. Phys. B At. Mol. Phys.*, 5(11):2066, 1972.

[110] Paul M. Holland and Louis Biolsi. Transport properties of ground state oxygen atoms. *J. Chem. Phys.*, 89(5):3203, 1988.

[111] M. Capitelli, R. Celiberto, and C. Gorse. Transport Properties of High Temperature Air Components: A Review. *Plasma Chem. Plasma Process.*, 16(1):267–302, 1996.

[112] Michael J. Wright, Deepak Bose, Grant E. Palmer, and Eugene Levin. Recommended Collision Integrals for Transport Property Computations Part 1: Air Species. *AIAA J.*, 43(12):2558–2564, 2005.

[113] Mario Capitelli. *Molecular physics and hypersonic flows*. Springer, 1996.

[114] James MacDonald. Accurate collision integrals for the attractive static screened coulomb potential with application to electrical conductivity. *The Astrophysical Journal Supplement Series*, 76:369–381, 1991.

[115] Anne Thoul, J Montalbán, A Thoul, and J Montalbán. Microscopic diffusion in stellar plasmas. *EAS Publications Series*, 26:25–36, 2007.

[116] Vanina Recoules, Flavien Lambert, Alain Decoster, Benoit Canaud, and Jean Clérouin. AbInitio Determination of Thermal Conductivity of Dense Hydrogen Plasmas. *Phys. Rev. Lett.*, 102(7):075002, 2009.

[117] Andrew B. Weaver and Alina A. Alexeenko. Revised variable soft sphere and lennard-jones model parameters for 8 common gases up to 2200 k. *J. Phys. Chem. Ref. Data*, 2015. (submitted).

[118] P.M. Banks and G. Kockarts. *Aeronomy*, volume 1. Academic Press, New York, 1973.

[119] Michael J. Wright, Helen H. Hwang, and David W. Schwenke. Recommended Collision Integrals for Transport Property Computations Part II: Mars and Venus Entries. *AIAA J.*, 45(1):281–288, 2007.

[120] Domenico Bruno, Aldo Frezzotti, and Gian Pietro Ghiroldi. Oxygen transport properties estimation by DSMC-CT simulations. In *Proc. 29th Int. Symp. Rarefied Gas Dyn.*, volume 108, pages 108–114, Xi'an, 2014. AIP.

[121] Daniel D. Konowalow and Joseph O. Hirschfelder. Morse Potential Parameters for O-O, N-N, and N-O Interactions. *Phys. Fluids*, 4(5):637, 1961.

[122] Francis J. Smith and R. J. Munn. Automatic Calculation of the Transport Collision Integrals with Tables for the Morse Potential. *J. Chem. Phys.*, 41(11):3560, 1964.

[123] R. J. Munn, Francis J. Smith, Edward A. Mason, and L. Monchick. Transport Collision Integrals for Quantum Gases Obeying a 126 Potential. *J. Chem. Phys.*, 42(2):537–539, 1965.

[124] P.M. Banks and G. Kockarts. *Aeronomy*, volume 2. Academic Press, New York, 1973.

[125] M.J. Wright, D.K. Prabhu, and E.R. Martinez. Analysis of apollo command module afterbody heating. part i: As-202. *JTHT*, 20(1):16–30, 2006.

[126] W.F. Louisos, A.A. Alexeenko, D.L. Hitt, and A. Zilic. Design considerations for supersonic micronozzles. *Int. J. Manuf. Res.*, 3(1):80–113, 2008.

[127] C. Zener. Interchange of translational, rotational, and vibrational energy in molecular collisions. *Phys. Rev.*, 12(1):57–65, 1998.

[128] R.N. Schwartz, Z.I. Slawsky, and K.F. Herzfeld. Calculation of vibrational relaxation times in gases. *J. Chem. Phys.*, 20(10):1591–1599, 1952.

[129] J.M. Jackson and N.F. Mott. Energy exchange between inert gas atoms and a solid surface. *P. Roy. Soc. A-Math. Phys.*, 137(833):703–717, 1932.

[130] L Landau and E Teller. Zur theorie der schalldispersion. *Phys. Z. Sowjetunion*, 10(1):34, 1936.

[131] A. Zelechow and D. Rapp. Vibrational-vibrational-translational energy transfer between two diatomic molecules. *J. Chem. Phys.*, 49(1):286–299, 1968.

[132] I.V. Adamovich. Three-dimensional analytic model of vibrational energy transfer in molecule-molecule collisions. *AIAAJ*, 39(10):1916–1925, 2001.

[133] Y.E. Gorbachev and F. Mallinger. A quasi-classical model for vt and vv rate constants. *JTHT*, 13(4):411–423, 1998.

[134] G.D. Billing and E.R. Fisher. Vv and vt rate coefficients in n_2 by a quantum-classical model. *Chem. Phys.*, 43(3):395–401, 1979.

[135] G.D. Billing. Rate constants and cross sections for vibrational transitions in atom-diatom and diatom-diatom collisions. *Comput. Phys. Commun.*, 32(1):45–62, 1984.

[136] G.D. Billing. *The Quantum Classical Theory.* Oxford University Press, USA, 2003.

[137] M. Cacciatore, A. Kurnosov, and A. Napartovich. Vibrational energy transfer in n_2–n_2 collisions: A new semiclassical study. *J. Chem. Phys.*, 123(17):174315–1–174315–10, 2005.

[138] M. Karplus, R.N. Porter, and R.D. Sharma. Exchange reactions with activation energy. i. simple barrier potential for (h–h_2). *J. Chem. Phys.*, 43(9):3259–3287, 1965.

[139] Andrew B. Weaver, Venkattraman Ayyaswamy, and Alina A. Alexeenko. Implementation Challenges and Performance of Forced Harmonic Oscillator Model in DSMC. In *44th AIAA Thermophys. Conf.*, pages 1–14, San Diego, 2013. AIAA.

[140] F. Reif. *Fundamentals of Statistical and Thermal Physics*. McGraw-Hill New York, 1965.

[141] Zheng Li, T Zhu, and Deborah A Levin. DSMC Simulation of Vibrational Excitation and Reaction for Molecular Nitrogen in Shock Tube Flows. In *51st AIAA Aerosp. Sci. Meet.*, pages 1–20, Grapevine, 2013. AIAA.

[142] Igor V. Adamovich. Three-Dimensional Analytic Model of Coupled Vibrational-Rotational-Translational Energy Transfer in Diatomic Molecule Collisions. In *AIAA SciTech 52 Aerosp. Sci. Meet.*, number January, pages 1–23, National Harbor, 2014. AIAA.

[143] Edward H. Kerner. Note on the Forced and Damped Oscillator in Quantum Mechanics. *Can. J. Phys.*, 36:371–377, 1958.

APPENDICES

A. Reduced Collision Integrals for the LJPA model

Table A.1.: Reduced Collision Integrals for the LJPA model based on (12-6) L-J potential and neglecting scattering angles less than 0.1 radians

T^*	$\Omega^{*(1,1)}$	$\Omega^{*(1,2)}$	$\Omega^{*(2,2)}$	$\Omega^{*(2,3)}$	$\Omega^{*(2,4)}$	$\Omega^{*(2,5)}$	$\Omega^{*(2,6)}$	$\Omega^{*(4,4)}$
0.10	3.945957	3.500814	4.080144	3.741300	3.497027	3.312427	3.168215	3.752721
0.15	3.431486	3.026402	3.575068	3.290126	3.085649	2.925075	2.787177	3.299986
0.20	3.087775	2.694126	3.262964	3.001659	2.800466	2.627065	2.467891	2.993720
0.25	2.825225	2.434116	3.031267	2.770913	2.557225	2.367848	2.197137	2.746523
0.30	2.611942	2.223666	2.838839	2.570691	2.345630	2.149612	1.980000	2.538056
0.35	2.433581	2.051193	2.670990	2.394864	2.164625	1.970405	1.808775	2.360267
0.40	2.282065	1.908647	2.522068	2.241070	2.011454	1.824046	1.672938	2.207620
0.45	2.152011	1.789830	2.389262	2.107042	1.882109	1.703878	1.563664	2.075741
0.50	2.039464	1.689889	2.270622	1.990315	1.772523	1.604277	1.474462	1.961148
0.55	1.941365	1.605032	2.164497	1.888473	1.679132	1.520878	1.400703	1.861069
0.60	1.855290	1.532308	2.069408	1.799322	1.599009	1.450377	1.339052	1.773276
0.65	1.779293	1.469423	1.984021	1.720963	1.529806	1.390273	1.287041	1.695957
0.70	1.711801	1.414587	1.907156	1.651789	1.469655	1.338643	1.242799	1.627618
0.75	1.651531	1.366400	1.837775	1.590459	1.417065	1.293987	1.204872	1.567011
0.80	1.597432	1.323755	1.774974	1.535853	1.370833	1.255116	1.172116	1.513084
0.85	1.548640	1.285773	1.717972	1.487038	1.329984	1.221077	1.143623	1.464945
0.90	1.504438	1.251748	1.666090	1.443231	1.293717	1.191099	1.118666	1.421836
0.95	1.464229	1.221106	1.618742	1.403774	1.261372	1.164552	1.096662	1.383107
1.00	1.427510	1.193380	1.575420	1.368112	1.232401	1.140920	1.077143	1.348204
1.05	1.393860	1.168183	1.535682	1.335773	1.206344	1.119780	1.059729	1.316650
1.10	1.362921	1.145194	1.499144	1.306355	1.182818	1.100780	1.044116	1.288038
1.15	1.334386	1.124142	1.465472	1.279514	1.161497	1.083632	1.030054	1.262017
1.20	1.307994	1.104799	1.434372	1.254952	1.142109	1.068095	1.017343	1.238285

Continued on next page

Table A.1 – *Continued from previous page*

T^*	$\Omega^{*(1,1)}$	$\Omega^{*(1,2)}$	$\Omega^{*(2,2)}$	$\Omega^{*(2,3)}$	$\Omega^{*(2,4)}$	$\Omega^{*(2,5)}$	$\Omega^{*(2,6)}$	$\Omega^{*(4,4)}$
1.25	1.283517	1.086970	1.405586	1.232416	1.124419	1.053966	1.005815	1.216583
1.30	1.260762	1.070490	1.378887	1.211685	1.108230	1.041078	0.995332	1.196686
1.35	1.239556	1.055215	1.354076	1.192567	1.093374	1.029290	0.985778	1.178402
1.40	1.219750	1.041020	1.330977	1.174895	1.079704	1.018480	0.977055	1.161561
1.45	1.201215	1.027799	1.309432	1.158525	1.067096	1.008546	0.969078	1.146018
1.50	1.183835	1.015456	1.289304	1.143328	1.055443	0.999399	0.961772	1.131647
1.55	1.167508	1.003909	1.270467	1.129195	1.044650	0.990962	0.955072	1.118335
1.60	1.152142	0.993086	1.252811	1.116025	1.034635	0.983169	0.948919	1.105985
1.65	1.137659	0.982922	1.236239	1.103733	1.025327	0.975959	0.943259	1.094510
1.70	1.123986	0.973360	1.220661	1.092242	1.016663	0.969280	0.938044	1.083833
1.75	1.111058	0.964349	1.205998	1.081483	1.008586	0.963083	0.933230	1.073886
1.80	1.098817	0.955845	1.192178	1.071395	1.001046	0.957325	0.928774	1.064608
1.85	1.087213	0.947808	1.179137	1.061924	0.993998	0.951967	0.924640	1.055943
1.90	1.076196	0.940200	1.166816	1.053021	0.987402	0.946973	0.920792	1.047841
1.95	1.065726	0.932990	1.155163	1.044642	0.981220	0.942311	0.917199	1.040257
2.00	1.055763	0.926148	1.144130	1.036746	0.975419	0.937949	0.913832	1.033149
2.05	1.046273	0.919648	1.133672	1.029298	0.969969	0.933861	0.910665	1.026481
2.10	1.037223	0.913465	1.123751	1.022265	0.964842	0.930020	0.907672	1.020217
2.15	1.028584	0.907578	1.114330	1.015617	0.960012	0.926404	0.904833	1.014325
2.20	1.020330	0.901967	1.105375	1.009325	0.955455	0.922991	0.902128	1.008777
2.25	1.012436	0.896613	1.096857	1.003365	0.951151	0.919760	0.899538	1.003545
2.30	1.004879	0.891500	1.088746	0.997714	0.947078	0.916694	0.897049	0.998604
2.35	0.997640	0.886613	1.081017	0.992351	0.943218	0.913776	0.894646	0.993932
2.40	0.990699	0.881937	1.073646	0.987255	0.939555	0.910991	0.892317	0.989508
2.45	0.984039	0.877459	1.066611	0.982407	0.936072	0.908325	0.890052	0.985311
2.50	0.977644	0.873168	1.059892	0.977793	0.932755	0.905766	0.887840	0.981323
2.55	0.971498	0.869053	1.053469	0.973395	0.929590	0.903302	0.885674	0.977529
2.60	0.965587	0.865102	1.047326	0.969199	0.926566	0.900923	0.883547	0.973912
2.65	0.959899	0.861307	1.041445	0.965192	0.923669	0.898621	0.881452	0.970458
2.70	0.954422	0.857659	1.035811	0.961361	0.920891	0.896386	0.879384	0.967155
2.75	0.949144	0.854148	1.030410	0.957694	0.918221	0.894211	0.877340	0.963989

Continued on next page

Table A.1 – *Continued from previous page*

T^*	$\Omega^{*(1,1)}$	$\Omega^{*(1,2)}$	$\Omega^{*(2,2)}$	$\Omega^{*(2,3)}$	$\Omega^{*(2,4)}$	$\Omega^{*(2,5)}$	$\Omega^{*(2,6)}$	$\Omega^{*(4,4)}$
2.80	0.944055	0.850769	1.025230	0.954180	0.915650	0.892089	0.875315	0.960950
2.85	0.939146	0.847513	1.020256	0.950810	0.913169	0.890015	0.873307	0.958028
2.90	0.934407	0.844373	1.015479	0.947574	0.910773	0.887984	0.871313	0.955213
2.95	0.929829	0.841344	1.010887	0.944462	0.908452	0.885990	0.869331	0.952496
3.00	0.925406	0.838419	1.006469	0.941468	0.906202	0.884030	0.867360	0.949870
3.05	0.921128	0.835593	1.002217	0.938582	0.904016	0.882099	0.865399	0.947327
3.10	0.916990	0.832861	0.998121	0.935799	0.901889	0.880196	0.863446	0.944861
3.15	0.912984	0.830217	0.994172	0.933111	0.899816	0.878316	0.861502	0.942465
3.20	0.909105	0.827657	0.990364	0.930512	0.897792	0.876459	0.859565	0.940133
3.25	0.905347	0.825177	0.986688	0.927996	0.895814	0.874620	0.857636	0.937862
3.30	0.901703	0.822773	0.983138	0.925559	0.893878	0.872800	0.855715	0.935645
3.35	0.898170	0.820441	0.979707	0.923195	0.891981	0.870996	0.853801	0.933480
3.40	0.894741	0.818176	0.976388	0.920899	0.890119	0.869206	0.851895	0.931361
3.45	0.891413	0.815977	0.973177	0.918667	0.888290	0.867431	0.849997	0.929285
3.50	0.888180	0.813839	0.970067	0.916495	0.886490	0.865669	0.848108	0.927249
3.55	0.885039	0.811760	0.967053	0.914379	0.884719	0.863919	0.846228	0.925251
3.60	0.881986	0.809736	0.964130	0.912316	0.882974	0.862180	0.844357	0.923287
3.65	0.879017	0.807765	0.961294	0.910303	0.881253	0.860453	0.842496	0.921356
3.70	0.876128	0.805845	0.958541	0.908336	0.879555	0.858737	0.840645	0.919454
3.75	0.873317	0.803973	0.955865	0.906413	0.877877	0.857030	0.838805	0.917580
3.80	0.870580	0.802146	0.953264	0.904530	0.876219	0.855334	0.836976	0.915733
3.85	0.867914	0.800363	0.950734	0.902687	0.874579	0.853648	0.835158	0.913910
3.90	0.865315	0.798622	0.948271	0.900879	0.872956	0.851972	0.833352	0.912110
3.95	0.862782	0.796920	0.945873	0.899106	0.871350	0.850306	0.831559	0.910332
4.00	0.860312	0.795256	0.943535	0.897365	0.869760	0.848650	0.829778	0.908575
4.05	0.857902	0.793628	0.941255	0.895655	0.868184	0.847004	0.828011	0.906838
4.10	0.855550	0.792034	0.939030	0.893973	0.866622	0.845367	0.826257	0.905119
4.15	0.853254	0.790473	0.936858	0.892319	0.865073	0.843741	0.824516	0.903417
4.20	0.851011	0.788944	0.934736	0.890690	0.863537	0.842125	0.822790	0.901733
4.25	0.848820	0.787445	0.932662	0.889086	0.862014	0.840519	0.821078	0.900065
4.30	0.846678	0.785974	0.930634	0.887505	0.860502	0.838923	0.819380	0.898413

Continued on next page

Table A.1 – *Continued from previous page*

T^*	$\Omega^{*(1,1)}$	$\Omega^{*(1,2)}$	$\Omega^{*(2,2)}$	$\Omega^{*(2,3)}$	$\Omega^{*(2,4)}$	$\Omega^{*(2,5)}$	$\Omega^{*(2,6)}$	$\Omega^{*(4,4)}$
4.35	0.844584	0.784531	0.928650	0.885946	0.859003	0.837337	0.817697	0.896776
4.40	0.842536	0.783115	0.926707	0.884408	0.857514	0.835762	0.816029	0.895153
4.45	0.840532	0.781723	0.924804	0.882889	0.856036	0.834198	0.814376	0.893545
4.50	0.838571	0.780356	0.922939	0.881390	0.854569	0.832644	0.812738	0.891950
4.55	0.836651	0.779012	0.921110	0.879909	0.853113	0.831102	0.811116	0.890369
4.60	0.834770	0.777690	0.919316	0.878445	0.851667	0.829570	0.809509	0.888801
4.65	0.832928	0.776389	0.917555	0.876998	0.850231	0.828049	0.807918	0.887245
4.70	0.831122	0.775110	0.915827	0.875567	0.848805	0.826539	0.806342	0.885703
4.75	0.829352	0.773849	0.914129	0.874151	0.847388	0.825041	0.804782	0.884172
4.80	0.827616	0.772608	0.912460	0.872749	0.845982	0.823554	0.803237	0.882654
4.85	0.825914	0.771385	0.910819	0.871362	0.844585	0.822078	0.801709	0.881147
4.90	0.824243	0.770179	0.909205	0.869989	0.843197	0.820614	0.800196	0.879652
4.95	0.822603	0.768990	0.907617	0.868628	0.841819	0.819161	0.798698	0.878169
5.00	0.820993	0.767818	0.906054	0.867281	0.840451	0.817720	0.797217	0.876698
6.00	0.793795	0.747059	0.878829	0.842532	0.815006	0.791366	0.770775	0.849540
7.00	0.773053	0.729830	0.856704	0.821106	0.793108	0.769542	0.749822	0.826418
8.00	0.756160	0.714908	0.837760	0.802409	0.774497	0.751715	0.733380	0.806914
9.00	0.741805	0.701739	0.821168	0.786121	0.758801	0.737242	0.720519	0.790562
10.00	0.729273	0.690015	0.806496	0.771966	0.745614	0.725503	0.710411	0.776887
11.00	0.718141	0.679532	0.793466	0.759684	0.734539	0.715937	0.702349	0.765441
12.00	0.708140	0.670130	0.781865	0.749026	0.725206	0.708060	0.695762	0.755820
13.00	0.699084	0.661677	0.771519	0.739760	0.717292	0.701469	0.690212	0.747673
14.00	0.690836	0.654055	0.762273	0.731676	0.710515	0.695842	0.685375	0.740702
15.00	0.683289	0.647161	0.753992	0.724587	0.704644	0.690929	0.681020	0.734660
16.00	0.676359	0.640903	0.746552	0.718330	0.699486	0.686539	0.676987	0.729345
17.00	0.669971	0.635197	0.739847	0.712767	0.694888	0.682531	0.673169	0.724600
18.00	0.664066	0.629972	0.733779	0.707778	0.690727	0.678800	0.669494	0.720296
19.00	0.658590	0.625163	0.728264	0.703264	0.686908	0.675272	0.665920	0.716337
20.00	0.653496	0.620716	0.723229	0.699144	0.683356	0.671894	0.662418	0.712646
21.00	0.648743	0.616581	0.718610	0.695350	0.680014	0.668628	0.658973	0.709167
22.00	0.644296	0.612719	0.714351	0.691825	0.676838	0.665450	0.655580	0.705853

Continued on next page

Table A.1 – *Continued from previous page*

T^*	$\Omega^{*(1,1)}$	$\Omega^{*(1,2)}$	$\Omega^{*(2,2)}$	$\Omega^{*(2,3)}$	$\Omega^{*(2,4)}$	$\Omega^{*(2,5)}$	$\Omega^{*(2,6)}$	$\Omega^{*(4,4)}$
23.00	0.640121	0.609092	0.710404	0.688524	0.673793	0.662343	0.652235	0.702674
24.00	0.636192	0.605670	0.706728	0.685409	0.670856	0.659295	0.648937	0.699603
25.00	0.632483	0.602428	0.703287	0.682451	0.668007	0.656299	0.645691	0.696623
26.00	0.628972	0.599343	0.700051	0.679624	0.665232	0.653353	0.642497	0.693721
27.00	0.625640	0.596397	0.696994	0.676910	0.662521	0.650454	0.639359	0.690886
28.00	0.622468	0.593572	0.694093	0.674291	0.659867	0.647600	0.636280	0.688111
29.00	0.619443	0.590856	0.691330	0.671754	0.657263	0.644793	0.633260	0.685391
30.00	0.616549	0.588237	0.688688	0.669290	0.654706	0.642033	0.630303	0.682723
31.00	0.613776	0.585705	0.686153	0.666890	0.652193	0.639320	0.627409	0.680104
32.00	0.611113	0.583252	0.683713	0.664547	0.649722	0.636654	0.624578	0.677532
33.00	0.608550	0.580870	0.681358	0.662256	0.647292	0.634036	0.621811	0.675006
34.00	0.606078	0.578554	0.679080	0.660011	0.644902	0.631467	0.619107	0.672525
35.00	0.603690	0.576299	0.676869	0.657811	0.642550	0.628947	0.616465	0.670088
36.00	0.601380	0.574099	0.674721	0.655651	0.640237	0.626475	0.613886	0.667695
37.00	0.599141	0.571951	0.672630	0.653528	0.637962	0.624051	0.611367	0.665345
38.00	0.596969	0.569852	0.670590	0.651443	0.635725	0.621675	0.608908	0.663037
39.00	0.594858	0.567799	0.668597	0.649392	0.633526	0.619347	0.606505	0.660771
40.00	0.592805	0.565789	0.666649	0.647374	0.631363	0.617065	0.604159	0.658545
41.00	0.590805	0.563821	0.664741	0.645389	0.629236	0.614830	0.601867	0.656361
42.00	0.588855	0.561893	0.662872	0.643434	0.627146	0.612639	0.599628	0.654216
43.00	0.586952	0.560002	0.661038	0.641510	0.625091	0.610493	0.597440	0.652111
44.00	0.585093	0.558147	0.659238	0.639616	0.623072	0.608389	0.595300	0.650043
45.00	0.583277	0.556327	0.657470	0.637750	0.621087	0.606328	0.593208	0.648013
46.00	0.581499	0.554541	0.655732	0.635913	0.619136	0.604308	0.591162	0.646020
47.00	0.579760	0.552787	0.654023	0.634103	0.617219	0.602327	0.589159	0.644063
48.00	0.578056	0.551065	0.652341	0.632320	0.615334	0.600386	0.587198	0.642141
49.00	0.576385	0.549374	0.650686	0.630564	0.613482	0.598482	0.585278	0.640253
50.00	0.574748	0.547713	0.649056	0.628834	0.611661	0.596614	0.583397	0.638398
60.00	0.559888	0.532578	0.633978	0.612861	0.595038	0.579717	0.566417	0.621484
70.00	0.547212	0.519719	0.620755	0.598998	0.580848	0.565408	0.551973	0.607010
80.00	0.536188	0.508659	0.609027	0.586855	0.568540	0.552996	0.539345	0.594371

Continued on next page

Table A.1 – *Continued from previous page*

T^*	$\Omega^{*(1,1)}$	$\Omega^{*(1,2)}$	$\Omega^{*(2,2)}$	$\Omega^{*(2,3)}$	$\Omega^{*(2,4)}$	$\Omega^{*(2,5)}$	$\Omega^{*(2,6)}$	$\Omega^{*(4,4)}$
90.00	0.526474	0.499013	0.598541	0.576118	0.557714	0.542066	0.528232	0.583163
100.00	0.517821	0.490478	0.589105	0.566543	0.548100	0.532394	0.518539	0.573130
200.00	0.462122	0.435076	0.529247	0.508112	0.492013	0.479749	0.470400	0.513402
300.00	0.430446	0.404088	0.498489	0.479593	0.465699	0.454905	0.445864	0.485378
400.00	0.408995	0.384168	0.478201	0.460461	0.447101	0.436185	0.426719	0.465824
500.00	0.393262	0.369944	0.462849	0.445607	0.432292	0.421212	0.411634	0.450341

B. Formulation of Forced Harmonic Oscillator Model

Kerner [143] had published in 1958 a solution to the time-dependent Schrödinger wave (TDSW) equation for a single oscillator subjected to an external force, $F(t)$. Thus, this solution is applicable to a atom-diatom interaction. This was obtained through a coordinate transformation such that the wave function moved with the collision, and then using separation of variables. This solution proceeds as follows.

First, the TDSW equation is written for a harmonic oscillator as

$$-\frac{\hbar^2}{2m}\frac{\partial^2\Psi}{\partial x^2} + \overbrace{\left[\frac{1}{2}kx^2 - xF(t)\right]}^{V(x,t)}\Psi = \imath\hbar\frac{\partial\Psi}{\partial t} \tag{B.1}$$

where $kx^2/2$ is the potential energy for the harmonic oscillator and the potential from the external force is given by $xF(t)$. Use the transformations,

$$\Psi = \chi\,\exp\left(xg(t)\right), \qquad \chi = \phi\left(x - u(t), t\right) = \phi\left(\xi, t\right), \tag{B.2}$$

and define the derivatives as follows.

$$\begin{aligned}\frac{\partial\Psi}{\partial x} &= \frac{\partial\Psi}{\partial\xi}\\ &= \frac{\partial\chi}{\partial\phi}\frac{\partial\phi}{\partial\xi}\,\exp\left[\left(\xi + u(t)\right)g(t)\right] + \frac{\partial\left(\xi + u(t)\right)g(t)}{\partial\xi}\,\exp\left[\left(\xi + u(t)\right)g(t)\right]\\ &= \frac{\partial\phi}{\partial\xi}\,\exp\left[\left(\xi + u(t)\right)g(t)\right] + g(t)\phi(\xi,t)\,\exp\left[\left(\xi + u(t)\right)g(t)\right]\end{aligned} \tag{B.3}$$

The second order spatial derivative which appears in the TDSW equation is then

$$\begin{aligned}\frac{\partial^2\Psi}{\partial x^2} &= \frac{\partial\Psi}{\partial\xi^2}\\ &= \frac{\partial}{\partial\xi}\left(\frac{\partial\Psi}{\partial\xi}\right)\\ &= \exp\left[\left(\xi + u(t)\right)g(t)\right]\left\{\frac{\partial^2\Phi}{\partial\xi^2} + g(t)\frac{\partial\phi}{\partial\xi} + \frac{\partial\phi}{\partial\xi}g(t) + g^2(t)\phi(\xi,t)\right\}\end{aligned} \tag{B.4}$$

The time derivative is similarly obtained.

$$\begin{aligned}\frac{\partial \Psi}{\partial t} &= \frac{\partial \chi}{\partial \phi}\left(\frac{\partial \phi}{\partial t}+\frac{\partial \phi}{\partial \xi}\frac{\partial \xi}{\partial t}\right)\exp\left[\left(\xi+u(t)\right)g(t)\right]+\left(\xi+u(t)\right)\frac{\partial g}{\partial t}\phi(\xi,t)\,\exp\left[\left(\xi+u(t)\right)g(t)\right]\\ &= \exp\left[\left(\xi+u(t)\right)g(t)\right]\left\{\frac{\partial \phi}{\partial t}-\frac{\partial \phi}{\partial \xi}\frac{\partial u(t)}{\partial t}+\phi(\xi,t)\left(\xi+u(t)\right)\frac{\partial g}{\partial t}\right\}\end{aligned} \tag{B.5}$$

Substitute these definitions for the derivatives into the TDSW equation, Eq. (B.1), and cancel out the exponential term.

$$-\frac{\hbar^2}{2m}\left[\frac{\partial^2\phi}{\partial\xi^2}+2g\frac{\partial\phi}{\partial\xi}+g^2\phi\right]+\left[\frac{1}{2}k\left(\xi+u\right)^2-\left(\xi+u\right)F(t)\right]\phi=\imath\hbar\left[\frac{\partial\phi}{\partial t}-\frac{\partial\phi}{\partial\xi}\dot{u}+\dot{g}\phi\right] \tag{B.6}$$

Rearrange the common terms.

$$\begin{aligned}&-\frac{\hbar^2}{2m}\frac{\partial^2\phi}{\partial\xi^2}+\left[\imath\hbar\dot{u}-\frac{\hbar^2 g}{m}\right]\frac{\partial\phi}{\partial\xi}\\ &\qquad+\left[\frac{1}{2}k\xi^2+\xi\left(ku-F(t)-\imath\hbar\dot{g}\right)+\underbrace{\left(\frac{1}{2}ku^2-uF(t)-\imath\hbar u\dot{g}-\frac{\hbar^2}{2m}\right)}_{\delta(t)}\right]\phi=\imath\hbar\frac{\partial\phi}{\partial t}\end{aligned} \tag{B.7}$$

For an undamped system we need to eliminate the $\partial\phi/\partial\xi$ and $\xi\phi$ terms. The variables g and u are arbitrary and may be used to reduce the coefficients of these terms to zero.

$$\imath\hbar\dot{u}-\frac{\hbar^2 g}{m}=0,\qquad ku-F(t)-\imath\hbar\dot{g}=0 \tag{B.8}$$

Taking the derivative of the $\partial\phi/\partial\xi$ coefficient with respect to time enables the substitution into the second equation containing $F(t)$.

$$\frac{\hbar}{m}\dot{g}=\imath\ddot{u}\rightarrow m\ddot{u}=-\imath\hbar\dot{g} \tag{B.9}$$

$$\begin{aligned}F &= ku-\imath\hbar\dot{g}\\ &= ku+m\ddot{u}\end{aligned} \tag{B.10}$$

This reduces the partial differential equation (PDE) to

$$-\frac{\hbar^2}{2m}\frac{\partial^2\phi}{\partial\xi^2}+\left[\frac{1}{2}k\xi^2+\delta(t)\right]\phi=\imath\hbar\frac{\partial\phi}{\partial t} \tag{B.11}$$

Now use separation of variables to solve the PDE. Start by writing the wavefunction, $\phi(\xi,t)$, as

$$\phi(\xi,t)=F(\xi)G(t), \tag{B.12}$$

and then substituting this into the PDE as expressed in Eq. (B.11).

$$-\frac{\hbar^2}{2m}F''G+\left(\frac{1}{2}k\xi^2+\delta(t)\right)FG=\imath\hbar F\dot{G} \tag{B.13}$$

Divide both sides by the product, FG, and separate ξ and t terms into two groups.

$$-\frac{\hbar^2}{2m}\frac{F''}{F}+\frac{1}{2}k\xi^2=\imath\hbar\frac{\dot{G}}{G}-\delta(t) \tag{B.14}$$

Since the variables have been separated then each side of the equation must be equal to a constant, C. We may also relate the spring constant, k, for a harmonic oscillator to the oscillation angular frequency, ω.

$$\omega=\sqrt{\frac{k}{m}}\rightarrow k=m\omega^2,\qquad \alpha^2=\frac{mk}{\hbar^2}=\frac{m^2\omega^2}{\hbar^2} \tag{B.15}$$

$$F''-\alpha^2\xi^2F+\frac{2m}{\hbar^2}CF=0 \tag{B.16}$$

At this point, the ODE for the variable ξ looks very much like that of the unperturbed, stationary, harmonic oscillator. The solution from here may be carried out in a manner consistent with the harmonic oscillator solution as provided by Levine [22]. Start by introducing a new function, $h(\xi)$, which depends on $F(\xi)$.

$$h(\xi)=\mathrm{e}^{-\alpha\xi^2/2}\,F(\xi)\rightarrow F(\xi)=h(\xi)\,\mathrm{e}^{-\alpha\xi^2/2} \tag{B.17}$$

In order to substitute this representation for $F(\xi)$, expand the second-order derivative.

$$\begin{aligned}\frac{\partial^2F}{\partial\xi^2}&=\frac{\partial}{\partial\xi}\left[-\alpha\xi\,\mathrm{e}^{-\alpha\xi^2/2}h(\xi)+h'\,\mathrm{e}^{-\alpha\xi^2/2}\right]\\&=-\alpha\,\mathrm{e}^{-\alpha\xi^2/2}h(\xi)+\alpha^2\xi^2\,\mathrm{e}^{-\alpha\xi^2/2}h(\xi)-\alpha\xi\,\mathrm{e}^{-\alpha\xi^2/2}h'(\xi)+h''(\xi)\,\mathrm{e}^{-\alpha\xi^2/2}-\alpha\xi h'(\xi)\,\mathrm{e}^{-\alpha\xi^2/2}\end{aligned} \tag{B.18}$$

Now, the ODE becomes

$$h''(\xi) + h'(\xi)\left(-2\alpha\xi\right) + h(\xi)\left(-\alpha^2\xi^2 + \alpha^2\xi^2 - \alpha + \frac{2m}{\hbar^2}C\right) = 0 \tag{B.19}$$

The $\alpha^2\xi^2$ terms thus cancel out and we are left with

$$h''(\xi) + h'(\xi)\left(-2\alpha\xi\right) + h(\xi)\left(\frac{2m}{\hbar^2}C - \alpha\right) = 0 \tag{B.20}$$

Proceed by representing the function, $h(\xi)$, as a polynomial expansion (power series method).

$$h(\xi) = \sum_n a_n \xi^n \tag{B.21}$$

Substituting this polynomial expansion into the ODE of Eq. (B.20) results in a series.

$$\sum_{n=2}^{\infty} n\left(n-1\right) a_n \xi^{n-2} - 2\alpha\xi \sum_{n=1}^{\infty} n a_n \xi^{n-1} + \left(\frac{2mC}{\hbar^2} - \alpha\right) \sum_{n=0}^{\infty} a_n \xi^n \tag{B.22}$$

The ξ multiplying the summation in the second term may be moved inside the summation. A substitution, $k = n - 2$ may be made for the first term in order to both start the summation at zero and have the proportionality of ξ^n rather than ξ^{n-1}. The second term may be set to start at $n = 0$ since this term is already zero at $n = 0$ due to the factor, n.

$$\begin{aligned}
&\sum_{k=0}^{\infty} \left(k+2\right)\left(k+1\right) a_{k+2} \xi^k - 2\alpha \sum_{n=0}^{\infty} n a_n \xi^n + \left(\frac{2mC}{\hbar^2} - \alpha\right) \sum_{n=0}^{\infty} a_n \xi^n = 0 \\
&= \sum_{n=0}^{\infty} \left[\left(n+2\right)\left(n+1\right) a_{n+2} - 2\alpha n a_n + \left(\frac{2mC}{\hbar^2} - \alpha\right) a_n\right] \xi^n
\end{aligned} \tag{B.23}$$

In order for this equation to be zero everywhere, the coefficients of ξ^n must be zero. Equating this to zero results in the following recursive formula.

$$a_{n+2} = \frac{\alpha + 2\alpha n - 2mC\hbar^{-2}}{\left(n+1\right)\left(n+2\right)} a_n \tag{B.24}$$

There is another stipulation that the wavefunction should be quadratically integrable. As it is now, the wavefunction would be

$$F(\xi) = A\,\mathrm{e}^{-\alpha\xi^2/2} \sum_{n=0}^{\infty} a_{2n} \xi^{2n} + B\,\mathrm{e}^{-\alpha\xi^2/2} \sum_{n=0}^{\infty} a_{2n+1} \xi^{2n+1} \tag{B.25}$$

and therefore we must make the coefficients of a_n zero in order to make the series go to zero as $\xi \to \infty$. Thus,

$$\alpha + 2\alpha n - \frac{2mC}{\hbar^2} = 0 \tag{B.26}$$

We can substitute back the relation for α, $\alpha = m\omega/\hbar$, in order to obtain the expected harmonic oscillator energy.

$$\frac{2\pi\nu m}{\hbar}(1+2n) = \frac{2mC}{\hbar^2} \to C = h\nu\left(\frac{1}{2}+n\right) \tag{B.27}$$

Note that we should set $n = v$ since C is a constant for this given v. When we substitute this back into the recursive formula for a_{n+2} we thus have a dependence on v and n.

$$a_{n+2} = \frac{2\alpha(n-v)}{(n+1)(n+2)}a_n \tag{B.28}$$

$$\begin{aligned} F(\xi) &= h(\xi)\,\mathrm{e}^{-\alpha\xi^2/2} \\ &= \begin{cases} \mathrm{e}^{-\alpha\xi^2/2}\left(a_0 + a_2\xi^2 + \ldots + a_v\xi^v\right) & \text{for v even} \\ \mathrm{e}^{-\alpha\xi^2/2}\left(a_1\xi + a_3\xi^3 + \ldots + a_v\xi^v\right) & \text{for v odd} \end{cases} \end{aligned} \tag{B.29}$$

Normalize the wavefunction such that:

$$\int_{-\infty}^{\infty} \phi_v^* \phi_v \,\mathrm{d}\xi = 1 \tag{B.30}$$

For $v = 0$:

$$1 = \int_{-\infty}^{\infty} |a_0|^2 \,\mathrm{e}^{-\alpha\xi^2/2}\,\mathrm{d}\xi \tag{B.31}$$

Now begin with the other ODE for time, t.

$$\dot{G} + \imath\delta(t)\frac{G}{\hbar} + \frac{\imath GC}{\hbar} = 0 \tag{B.32}$$

$$\dot{G} + \left(\frac{\imath\delta(t)}{\hbar} + \frac{\imath C}{\hbar}\right)G = 0 \tag{B.33}$$

The characteristic equation is then

$$r + \int_0^t \left(\frac{\imath\delta(t)}{\hbar} + \frac{\imath C}{\hbar}\right)\mathrm{d}t = 0 \tag{B.34}$$

$$r = -\frac{\imath}{\hbar}\int_0^t (\delta(t) + C)\ \mathrm{d}t \tag{B.35}$$

The function, $G(t)$, is for a single root

$$G(t) = A\ \exp\left[-\frac{\imath}{\hbar}\int_0^t (\delta(t) + E_v)\ \mathrm{d}t\right] \tag{B.36}$$

where the substitution for the constant, C, has been made. E_v refers to the harmonic oscillator energy as discussed earlier.

C. Formulation of Exponential Repulsive Interaction with a Harmonic Oscillator

If the masses of the colliding diatoms are similar then the assumption that the vibrational amplitude is small in comparison to the interaction range is reasonable. This allows for the simplification from an exponential potential depending on center-of-mass distance, X, and diatomic distance from vibrational equilibrium, Y,

$$\begin{aligned} V(X,Y) &= E_0 \exp\left(-X/L\right) \exp\left\{\left[m_C/\left(m_B+m_C\right)\right] Y/L\right\} \\ &\approx E_0 \exp\left(-X/L\right) \left\{1 - \left(\frac{m_C}{m_B+m_C}\right)\frac{Y}{L}\right\}, \quad \text{for small } Y/L \end{aligned} \tag{C.1}$$

to a potential which only depends on X,

$$V(X) \approx E_0 \exp\left(-X/L\right) \tag{C.2}$$

This potential is used to construct the classical trajectory and compute the amount of energy transferred from the translational mode into the vibration of the two diatoms. For any potential which only depends on X we may write

$$v = \frac{dX}{dt} = \sqrt{\frac{2}{\tilde{m}}\left(E_0 - V(X)\right)} \tag{C.3}$$

The goal here is to replace the potential's dependence on X with a dependence on time, t. Start by collecting variables depending on X on the left and variables depending on t on the right. Then integrate.

$$\int_{X_0}^{X} \frac{dX}{\sqrt{\frac{2}{\tilde{m}}\left(E_0 - V(X)\right)}} = t - t_0, \quad X = 0 \text{ at } t = 0, E_0 = \frac{1}{2}\tilde{m}v_0^2 \tag{C.4}$$

Thus, after subsitution for the potential $V(X)$

$$t = \int_0^X \frac{dX}{\sqrt{v_0^2\left(1 - \exp\left(-X/L\right)\right)}} = \frac{1}{v_0}\int_0^X \frac{dX}{\sqrt{1 - \exp\left(-X/L\right)}} \tag{C.5}$$

This integral is equal to

$$\begin{aligned} v_0 t &= 2\exp\left(X/2L\right)\exp\left(-X/2L\right) L \ln\left(\exp\left(X/2L\right) + \sqrt{\exp\left(X/L\right) - 1}\right) \\ &= 2L \ln\left(\exp\left(X/2L\right) + \sqrt{\exp\left(X/L\right) - 1}\right) \end{aligned} \tag{C.6}$$

Taking the exponential of both sides to eliminate the natural logarithm simplifies the expression to

$$\exp\left(v_0 t/2L\right) - \exp\left(X/2L\right) = \sqrt{\exp\left(X/L\right) - 1} \tag{C.7}$$

Now square both sides and eliminate the like terms, $\exp\left(X/L\right)$.

$$\exp\left(v_0 t/L\right) - 2\exp\left[\left(v_0 t + X\right)/2L\right] = -1 \tag{C.8}$$

Multiply both sides by $\exp\left(-X/2L\right)$ and divide both sides by $1 + \exp\left(v_0 t/L\right)$.

$$\exp\left(-X/2L\right) = \frac{2\exp\left(v_0 t/2L\right)}{1 + \exp\left(v_0 t/L\right)} \tag{C.9}$$

After squaring both sides we have obtained an expression for the potential in terms of time, t.

$$\begin{aligned} \exp\left(-X/L\right) &= \left(\frac{2\exp\left(v_0 t/2L\right)}{1 + \exp\left(v_0 t/L\right)}\right)^2 \\ &= \operatorname{sech}^2\left(v_0 t/2L\right) \end{aligned} \tag{C.10}$$

Therefore, we may substitute this expression replacing the dependence on X with t into the potential $V(X, Y)$ shown in Eq. (C.1). For two diatoms, this is equal to

$$V(t, Y_1, Y_2) = E_0 \operatorname{sech}^2\left(\frac{v_0 t}{2L}\right) \exp\left[\frac{\gamma}{L}\left(Y_1 + Y_2\right)\right] \tag{C.11}$$

The forcing function, $F(t)$, is computed as it normally is from a potential. That is,

$$\begin{aligned} F(t) &= -\nabla V(t, Y_1, Y_2) = -\frac{\partial V}{\partial Y_i} \\ &= \left(\frac{\gamma}{L} E_0 \operatorname{sech}^2 \left(\frac{v_0 t}{2L} \right) \exp \left[\frac{\gamma}{L} (Y_1 + Y_2) \right], \frac{\gamma}{L} E_0 \operatorname{sech}^2 \left(\frac{v_0 t}{2L} \right) \exp \left[\frac{\gamma}{L} (Y_1 + Y_2) \right] \right) \end{aligned} \tag{C.12}$$

One of the parameters in the VVT model from Zelechow *et al.* [131] is ϵ. This is defined mathematically as

$$\epsilon = \frac{\Delta E_{vib}}{\hbar \omega} \tag{C.13}$$

The change in vibrational energy, E_{vib}, may be written as [cite Rapp 1960]

$$\Delta E_{vib} = \frac{1}{2} \mu \omega^2 \left(|Y(\infty)|^2 - |Y(-\infty)|^2 \right) \tag{C.14}$$

where, using Green's method,

$$Y(t') - Y(-\infty) = \int_{-\infty}^{t'} \frac{F(t)}{\mu \omega} \, \mathrm{e}^{i \omega t} \, \mathrm{d}t \tag{C.15}$$

VITA

VITA

Andrew B. Weaver

4136 Stergen Dr.
Lafayette, IN 47909

abweaver@purdue.edu
Cell: 440.829.1918

Education

Ph.D.	Purdue University, Aeronautics & Astronautics G.P.A. 3.6/4.0 Advisor: Alina Alexeenko, Dissertation: "Assessment of High-Fidelity Collision Models in the Direct Simulation Monte Carlo Method"	May 2015
M.S.E	Purdue University, Aeronautics & Astronautics G.P.A. 3.7/4.0 Advisor: Alina Alexeenko, Thesis: "Analysis of Flowfield and Surface Heat Flux Uncertainties Under Typical Blunt-Body Re-Entry Conditions"	May 2010
B.S.M.E.	Ohio Northern University, Mechanical Engineering G.P.A. 3.1/4.0	May 2008

Research Interests

Hypersonic aerothermodynamics, computational modeling of high-enthalpy flows in continuum and rarefied regimes, molecular collision modeling, uncertainty quantification methods (UQ), direct simulation Monte Carlo (DSMC), numerical heat transfer

Journal Publications

A. Weaver and A. Alexeenko, "Comparison of Binary Scattering of Ground-State Atomic Oxygen based on Ab Initio and Empirical Potentials," *Journal of Chemical Physics* (submitted).

A. Weaver and A. Alexeenko, "Revised Variable Soft Sphere and Lennard-Jones Model Parameters for 8 Common Gases up to 2200 K," *Journal of Physical & Chemical Reference Data* (submitted).

A. Weaver, A. Venkattraman, and A. Alexeenko, "Effect of Intermolecular Potential on Compressible Couette Flow in Slip and Transitional Regimes," *Physics of Fluids* Vol. 26, No. 10, 2014, pp. 107102.

S. Chigullapalli, **A. Weaver**, and A. Alexeenko, "Nonlinear Effects in Squeeze-Film Gas Damping on Microbeams," *Journal of Micromechanics and Microengineering*, Vol. 22, No. 6, 2012, pp. 1–7.

A. Weaver, A. Alexeenko, R. Greendyke, and J. Camberos, "Uncertainty Analysis for Hypersonic CFD Simulations," *Journal of Thermophysics and Heat Transfer*, Vol. 25, No. 1, 2011, pp. 10–20.

Reports and Conference Papers

A. Weaver and A. Alexeenko, "Effect of Molecular Models on Viscosity and Thermal Conductivity Calculations," *Proceedings of the 29th Rarefied Gas Dynamics (RGD) Symposium*, Xi'an, China, July 2014. (to be published by AIP)

A. Weaver and A. Alexeenko, "Investigation of Multi-Element gPC Methods for Weaponeering Applications," *Final Report for Air Force Institute of Technology*, 2013, pp. 1–6.

A. Weaver, V. Ayyaswamy, and A. Alexeenko, "Implementation Challenges and Performance of Forced Harmonic Oscillator Model in DSMC," *44th AIAA Thermophysics Conference*, San Diego, CA., 2013, pp. 1–14.

A. Weaver, A. Alexeenko, K. Chi, and T. Shih, "CFD Simulation of Heat Transfer in Wet Friction Clutches and Brakes," *Final Report for Raybestos Powertrain*,

2012, pp. 1–20.

A. Weaver, A. Alexeenko, R. Greendyke, and J. Camberos, "Flowfield Uncertainty Analysis for Hypersonic CFD Simulations," *48th AIAA Aerospace Sciences Meeting*, Orlando, FL., 2010, pp. 1–11.

Professional Experience

Summer Intern, Sandia National Laboratory, NM May 2013 – July 2013

- Performed intermolecular model comparison over a wide temperature range within DSMC framework

Research Assistant, Purdue University, School of Aero. & Astro.

Sponsor: NASA February 2014 – July 2014

- Computationally model film-evaporation MEMS tunable array to aid in design of picosat propulsion

Sponsor: PRISM May 2011 – June 2013

- Analyzed non-linear gas damping effects in transitional regime for MEMS devices using ES-BGK model
- Improved life-cycle predictions of MEMS devices through use of accurate, open-to-close simulations

Sponsor: AFIT / U.S. STRATCOM October 2012 – June 2013

- Demonstrated fast sampling algorithms for multi-dimensional UQ analyses in weaponeering applications (i.e. polynomial chaos and Smolyak sparse grid)
- Developed and implemented a multi-element gPC code with a graphical user interface

Sponsor: Raybestos Powertrain December 2011 – July 2012

- Used CFD to predict thermal distributions in an automobile wet-clutch/brake pack subject to high thermal loading during engagement phase

Summer Researcher, Wright-Patterson Air Force Research Laboratory May 2009 – July 2009

- Performed uncertainty quantification (UQ) analysis for computational, hypersonic flows using NASA Langley's CFD software, LAURA
- Provided organization with efficient methods to determine flow properties of largest uncertainty

Teaching Experience, Purdue University, School of Aero. & Astro.

Course: Undergraduate Fluid Mechanics August 2014 – December 2014

- Full instructor for a class of 64 students
- Lectured and designed homework assignments and exams

Course: Molecular Gas Dynamics August 2013 – December 2013

- Lectured when instructor was absent
- Prepared solutions to exams and homework assignments
- Graded exams and homeworks and provided regular office hours

Course: Undergraduate Fluid Mechanics January 2012 – May 2012

- Lectured when instructor was absent
- Prepared solutions to homework assignments and provided regular office hours

Course: Graduate CFD January 2011 – May 2011

- Graded homework assignments and provided regular office hours

Course: Graduate Fluid Mechanics August 2010 – Dec. 2010

- Graded homework assignments and provided regular office hours

Co-op Student, Copeland Corporation, Sound and Vibration Laboratory September 2006 – February 2007

- Headed the development of two data acquisition programs using LabView

- Collaborated with customers for desired features in acquisition software
- Collected frequency response data for modal analysis
- Organized annual performance data and analyzed for quality control

Technical Skills

Scientific and Engineering Analysis Tools

CAD: Catia; *Meshing*: Cubit, Gambit, Gridgen; *Gas/Fluid Solvers*: ANSYS Fluent, NASA Langley LAURA, Bird DS2V; *Visualization*: Tecplot, Paraview

Programming/Scripting Languages

C/C++, Fortran (77/90/95), Matlab, Bash, Python, LabView

Operating System & Presentation Software

Windows, Unix/Linux, Mac OS, Microsoft Office Suite, LaTeX, Beamer

Affiliations

AIAA 2005 – Present

- Vice Chairman (2005 – 2006): Suggested and implemented plans for annual entrances to RC aircraft competitions. Organized recruiting events